Design and Development of a Morphing Wing Utilising Flexible Materials

by

Erasmus Johannes van Zyl

Thesis presented in partial fulfilment of the requirements for the degree of Master of Engineering (Mechanical) in the Faculty of Engineering at Stellenbosch University

Supervisor: Dr. MP. Venter

March 2020

Stellenbosch University https://scholar.sun.ac.za

Declaration

By submitting this thesis electronically, I declare that the entirety of the work contained therein is my own, original work, that I am the sole author thereof (save to the extent explicitly otherwise stated), that reproduction and publication thereof by Stellenbosch University will not infringe any third party rights and that I have not previously in its entirety or in part submitted it for obtaining any qualification.

Date: March 2020

Copyright © 2020 Stellenbosch University
All rights reserved.

Stellenbosch University https://scholar.sun.ac.za

Abstract

Design and Development of a Morphing Wing Utilising Flexible Materials

EJ. Van Zyl

Department of Mechanical and Mechatronic Engineering,
University of Stellenbosch,
Private Bag X1, Matieland 7602, South Africa.

Thesis: MEng (Mech)

March 2020

Aircraft wings are required to operate in a multitude of different aerodynamic conditions. To compensate for these varying conditions, modern aircraft are equipped with devices that can alter the aerodynamic characteristics of the wings by altering their shape. Most of these devices use a joint or hinge mechanism and are relatively effective at controlling the airflow over the wings but also introduce losses in aerodynamic efficiency due to discontinuities that they create in the wing surface. These devices also create large point loads at the joints or hinges, resulting in an increased likelihood of failure occurring at these locations. An iterative design method is followed in the development of a low-cost and robust small to medium-sized Unmanned Aerial Vehicle (UAV) wing capable of changing its camber during operation.

The overall design process was split into two sub-processes, namely designing a suitable wing base-structure and the design of a morphing mechanism to be used in combination with the base-structure. Multiple prototypes were developed and evaluated, which led to the selection of the best performing base-structure and morphing mechanism based on the overall stiffness of the prototype and the magnitude of possible camber-change.

Further exploration was carried out on the selected morphing mechanism through the use of central-composite design (CCD) studies in conjunction with a Response Surface Methodology approach and One-Factor-At-a-Time (OFAT) analysis. Through this process, a mathematical relationship between the build-parameters of the morphing mechanism and its resulting bending output was

Stellenbosch University https://scholar.sun.ac.za

established. The optimal build-parameter combination in the specified design range was obtained.

Through the knowledge gathered, a topologically simple and low-cost morphing wing was developed and constructed. The designed wing was fully inflatable, offered bi-directional camber morphing capabilities and also had the shape-changing mechanism directly embedded into the base-structure, resulting in a wing that utilized no rigid components or complex joints between parts, making the design more resilient to small to medium impacts in comparison to traditional wing designs.

Stellenbosch University https://scholar.sun.ac.za

Uittreksel

Ontwerp en Ontwikkeling van 'n Vervormbare Vlerk met behulp van Buigsame Materiale

("Design and Development of a Morphing Wing Utilizing Flexible Materials")

EJ. Van Zyl

Departement Meganiese en Megatroniese Ingenieurswese,
Universiteit van Stellenbosch,
Privaatsak X1, Matieland 7602, Suid Afrika.

Tesis: MIng (Meg)

Maart 2020

Vliegtuigvlerke word vereis om in 'n reeks van verskillende aerodinamiese toestande te funktioneer. Om te kompenseer vir hierdie verskillende toestande, is moderne vliegtuie toegerus met toestelle wat die aerodinamiese eienskappe van die vlerke kan verander deur om hul vorm te verander. Hierdie toestelle is relatief doeltreffend om die lugvloei oor die vlerke te beheer, maar meestal gebruik egter 'n las- of skarniermeganisme en tot die verlies aan aerodinamiese doeltreffendheid as gevolg van diskontinuïteite wat dit in die vlerkoppervlak veroorsaak. Hierdie toestelle skep ook groot puntlading by die laste of skarniere, wat lei tot 'n groter waarskynlikheid dat versuim op hierdie plekke sal voorkom. Die navorsing wat hier voorgelê word, het gefokus op die iteratiewe ontwerpmetode wat gevolg is in die ontwikkeling van 'n laekoste en robuuste klein tot mediumgrootte Onbemande Lugvoertuig (OLV) vlerk wat in staat is om die vlerkkromming tydens werking te verander.

Om die ontwerpproses te vereenvoudig is die algehele ontwerpsproses in twee sub-prosesse verdeel, naamlik die ontwerp van 'n geskikte vlerk-basisstruktuur en die ontwerp van 'n vlerk-vervormingsmeganisme wat in kombinasie met die basisstruktuur gebruik moet word. Deur hierdie proses is verskeie prototipes ontwikkel en geëvalueer, wat uiteindelik gelei het tot die keuse van die beste presterende vlerk-basisstruktuur en vervormingsmeganisme. Hierdie keuse is gebasseer op die algehele styfheid van die ontwerp as ook die omvang van die vlerkkrommingsverandering moontlik.

Stellenbosch University https://scholar.sun.ac.za

Verdere ondersoek is uitgevoer op die geselekteerde vlerk-vervormingsmeganisme deur gebruik te maak van sentraal-saamgestelde ontwerp (SSO) studies saam met 'n Responsoppervlakmetodologie benadering as ook 'n Een-Faktor-Op-'n-Slag (EFOS) studie. Deur middel van hierdie verskillende studies is 'n wiskundige verwantskap tussen die bou-parameters van die vlerk-vervormingsmeganisme en die gevolglike buiguitset daarvan en het ook die skatting van die optimale bou-parameter kombinasie in die gespesifiseerde ontwerpreeks moontlik gemaak.

Deur die kennis wat ingesamel is, is 'n topologies eenvoudige en laekoste vervormbare-vlerk ontwikkel en gebou. Die ontwerpte vlerk was volledig opblaasbaar, het tweerigting-vervormingsvermoë in terme van die vlerkkromming getoon en is so ontwerp dat die vlerk-vervormingsmeganisme direk in die basisstruktuur ingebou is, wat gelei het tot 'n vlerk wat geen regiede komponente of ingewikkelde verbindings tussen dele gebruik het nie en het dus die ontwerp meer bestand gemaak teen klein tot medium impak in vergelyking met tradisionele vlerkontwerpe.

Stellenbosch University https://scholar.sun.ac.za

Contents

Stellenbosch University https://scholar.sun.ac.za

Stellenbosch University https://scholar.sun.ac.za

List of Figures

Stellenbosch University https://scholar.sun.ac.za

Stellenbosch University https://scholar.sun.ac.za

List of Tables

Stellenbosch University https://scholar.sun.ac.za

Stellenbosch University https://scholar.sun.ac.za

Chapter 1

Introduction

The research presented here focuses on the design and development of a wing, using an iterative design approach, capable of changing its shape during operation. The following sections provide a detailed description of the scope, aims, and objectives of the project as well as descriptions of tasks and activities that were done to complete the project. An in-depth literature review as well as the project methodology, followed by the results and conclusions made are also included in this document.

1.1 Problem Statement and Motivation

Aircraft wings are required to operate in a multitude of different aerodynamic conditions. Aircraft spend most of their flight time in cruise, thus aircraft wings need to exhibit enough lift force to allow the aircraft to maintain altitude, while simultaneously offering a low drag coefficient in this specific velocity range. Other operating conditions include take-off, where a high lift force is required; and landing, where a high drag force is desirable.

Modern aircraft are equipped with devices, such as slats and flaps, that change the wing shape to allow the wing to deliver improved aerodynamic characteristics under varying conditions. Most of these devices use a joint or hinge mechanism and are relatively effective at controlling the airflow over the wings but also introduce losses in aerodynamic efficiency due to discontinuities that they create in the wing surface. These devices also create large point loads at the joints or hinges, resulting in an increased likelihood of failure occurring at these locations.

The problem at hand is to change the shape of a wing without introducing unnecessary wing-surface discontinuities as well as reducing the stress experienced by the joint or hinge of the wing morphing mechanism. The solution to this problem is to design and develop an aircraft wing utilizing smart and/or

Stellenbosch University https://scholar.sun.ac.za

flexible materials to allow the construction of a flexible wing with morphing mechanisms embedded directly into the structure. By doing so, the traditional mechanically controlled and complex wing morphing devices can be replaced by a single and topologically simpler structure. For the project, a focus will be placed on the structural design of the wing and the embedded morphing mechanism.

By replacing traditional aircraft wings along with the current shape altering devices with a topologically simpler morphing wing built from flexible and/or smart materials, the overall aerodynamic characteristics of an aircraft can be improved. This improvement is possible since a morphing wing will not cause any discontinuities in the wing surface associated with current wing morphing devices and will thus negate the losses encountered as a result of these discontinuities. Another benefit of using a wing constructed from flexible materials is the increase in robustness, making the morphing wing more likely to survive low- to medium-sized impacts without sustaining critical damage.

1.2 Aim and Objectives of Project

The project aims to design and develop a topologically simple, self-supporting wing capable of changing its camber while it is in operation.

Three objectives were identified that were necessary to successfully achieve the aim of the project.

1. Generation of multiple preliminary morphing wing designs utilizing different types of base-structures, deformation mechanism or a combination thereof.

2. Perform a parametric analysis on the best performing deformation mechanism to characterize the relationship between the performance of the mechanism and its design parameters.

3. Develop a prototype wing design using the proposed design method.

1.3 Scope of Project

Focus is placed on the structural design of the wing and shape-changing mechanism. Even though the project is somewhat related to aeronautics, the aerodynamic performance of the prototypes as well as the final design will not be considered as part of the project. Considerations regarding in-depth study the structural integrity or strength of the wing will not be investigated and time-dependent effects such as creep or fatigue of the design will also not form part of the scope. Lastly, the means as to how the developed wing will attach

Stellenbosch University https://scholar.sun.ac.za

to the fuselage of an aircraft will also be excluded from the scope.

The chosen scope can be further divided into two additional decision-making areas namely morphing type and actuation method to be implemented. To simplify the design phase, the morphing type for this project was limited to designs varying only the camber of the wing in an attempt to mimic current deformation mechanisms as found on modern aircraft.

1.4 Project Methodology

For this project, a design approach using the classical V-model was used. Using the V-model as a guideline, the general process needed to design a functional morphing wing was split into seven sub-processes namely design conception, identification of engineering requirements, broad system design, sub-system design, construction and implementation, system testing and refinement and lastly system verification. These sub-processes as well as the general V-model design methodology are described in Chapter 3 under Section 3.1.

For the initial conception phase, multiple conceptual designs were created, drawing inspiration from literature regarding morphing wings and aerofoils as well as from literature focusing on technology capable of inducing a shape change in a general structure. Using these conceptual designs, the requirements needed to develop a functional morphing wing were identified and refined.

Next, the broad system design was done, resulting in two system categories being identified, namely the base-structure of the wing and the deformation or shape-changing mechanism. The base-structure of the wing refers to the structure responsible for the integrity of the wing as well as the general shape of the wing, while the deformation mechanism refers to the mechanism that produces the desired shape change in the wing.

Multiple designs of morphing wings were generated in terms of base-structures as well as the incorporated deformation mechanism. For each design generated, a prototype was constructed and assessed, with possible improvements made thereafter, making the overall design process iterative in nature.

After all the designs had been constructed and evaluated, a single design was chosen based on four factors namely, how self-supporting the design is, how noticeable as well as how useful the shape change of the design is, the materials needed for the design and finally the overall complexity of the structure.

After the prototyping phase was completed and the most promising design identified, the chosen design was explored and analyzed further. The addi-

Stellenbosch University https://scholar.sun.ac.za

tional exploration was done primarily on the morphing mechanism through a parametric study to determine and quantify the effect changing values of the design parameters had on the resulting induced shape change. The parametric study was carried out through the utilization of a Design of Experiment (DoE) process in combination with a Response Surface Methodology (RSM) approach to determine a mathematical relationship between the construction parameters of the morphing mechanism and the resulting output. Both the DoE and the RSM methodologies are described in further detail in Chapter 3.

After the parametric study was completed, a One-Factor-at-a-Time (OFAT) study was done to further increase the understanding of the morphing mechanism. An OFAT study involves the changing of only a single design variable, while the other variables remained fixed.

From the data gathered from the various studies, a new wing design was developed applying all knowledge gained throughout the project and was used to verify if the final design satisfied the initial determined engineering requirements as well as if the possible camber change of the design correlates to the mathematical model derived during the RSM phase.

Stellenbosch University https://scholar.sun.ac.za

Chapter 2

Literature Review

2.1 Modern Mechanisms which Change Aircraft Wing Shape

The following Section provides a brief overview of the high-lift devices currently in use on modern aircraft. Although other high-lift devices are also available, this section will focus on slats and flaps, since these two devices are among the most popular and also mechanically simple to recreate with flexible technologies. The general location of where slats and flaps can be found on a wing is shown in Figure 2.1.

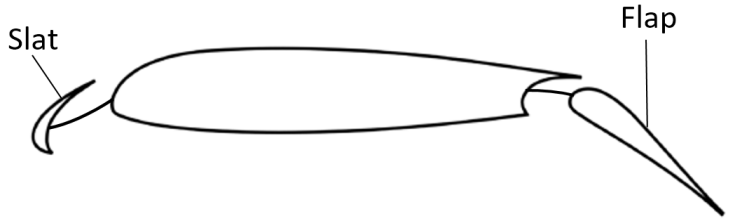

Figure 2.1: *General Location of Slats and Flaps on a Wing*

2.1.1 Slats

Slats form part of a group of devices referred to as High Lift Devices. Slats are commonly found on the leading edge of an aircraft wing. The purpose of these devices is to increase lift during low-speed operations such as take-off, initial climb, approach and also during landing (SKYbrary, 2016). This is accomplished by extending and slightly angling the slats downward, as illustrated in Figure 2.2.

Stellenbosch University https://scholar.sun.ac.za

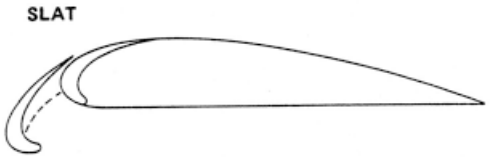

Figure 2.2: *Slats Extended from Leading Edge (SKYbrary, 2016)*

2.1.2 Flaps

Flaps are another type of High Lift Devices, but unlike slats, flaps are found on the trailing edge of the wing. Flaps consist of a single or in some cases multiple hinged panels that extend to effectively increase the camber profile, the chord length and the surface area of the wing. Flaps increase the lift and drag force through the same principles as described for the slats. There are many different flap configurations used today. Large aircraft often utilize more than one flap configuration on different sections of the wing.

The most common designs of flaps are Plain Flaps, Split Flaps, Slotted Flaps, Fowler Flaps and the Double Slotted Fowler Flaps (SKYbrary, 2016). A simple diagram illustrating the workings of each type of flap is shown in Figure 2.3. Plain Flaps (Figure 2.3a) consist of a single panel located at the leading edge of the wing and rotate downwards through a simple hinge mechanism fixed at the front of the flap.

Split Flaps (Figure 2.3b) form part of the lower surface of the wing when not in use. When activated, a section of the bottom part of the wing hinges downwards in the same fashion as for Plain Flaps. Slotted Flaps (Figure 2.3c) are similar to Plain Flaps, but incorporate a gap between the flap and the wing. High-pressure fluid from the bottom surface of the wing is forced through the gap and over the top surface of the flap. This aids in the reduction of boundary layer separation as well as prolonging the laminar flow region over the flap (SKYbrary, 2016).

A Fowler Flap (Figure 2.3d) is a split type flap that slides backward for a distance before it hinges downward. Fowler flaps thus increase firstly the cord length and surface area of the wing and secondly the camber profile. A Double Slotted Fowler Flap (Figure 2.3e) is an improved variation of the general Fowler Flap configuration and incorporates the benefit of the gap as found in Slotted Flaps. Fowler Flaps or variations of these are the most common flaps found on modern-day aircraft.

Stellenbosch University https://scholar.sun.ac.za

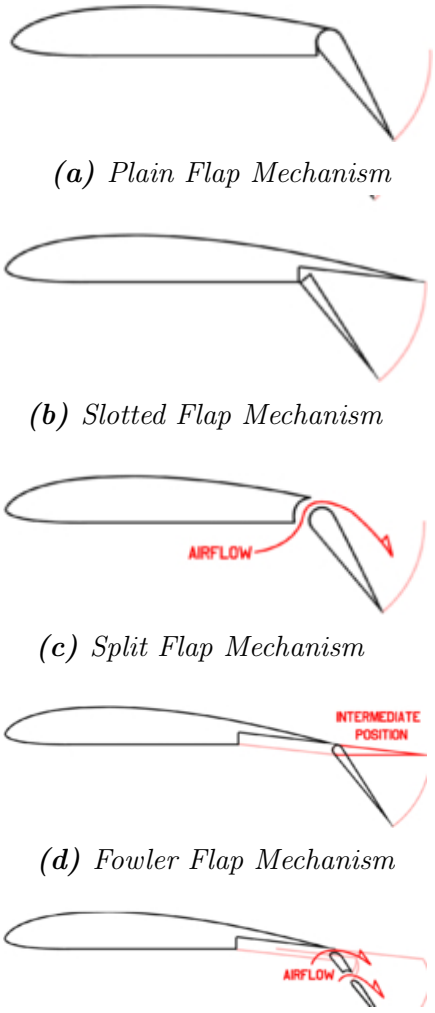

(a) Plain Flap Mechanism

(b) Slotted Flap Mechanism

(c) Split Flap Mechanism

(d) Fowler Flap Mechanism

(e) Double Slotted Fowler Flap Mechanism

Figure 2.3: *Different Types of Flap Mechanisms (SKYbrary, 2016)*

2.2 Types of Structures Employed

Much research has been done in the last several decades regarding morphing aerofoils and wings. There are several review papers available in literature summarising the many different innovations and concepts explored through research, most notably the writings of Chopra (2000) and Barbarino *et al.* (2011). In most studies involving morphing wings or aerofoils, the focus is placed on sections of the problem, for example developing a compliant skin or novel actuation mechanism for example, rather than the entire scope of the problem. In this section, some of the previously done research will be highlighted, split into relevant categories and discussed briefly. A description is given of previous research done in the fields of asymmetric laminates, corrugated composite skins, shape memory structures, inflatable structures as well

Stellenbosch University https://scholar.sun.ac.za

as kagome truss structures.

2.2.1 Asymmetric Laminates

Asymmetric laminates are often characterized by bi-stable deformation states present in the material due to residual stresses formed during cooling of the laminate (Dano and Hyer, 2001). The concept of using such laminates for shape-changing wings has clear benefits. Shape changing mechanisms brought on by piezo-ceramic or shape-memory alloy actuators require a constant supply of power to change the original shape to a nearby configuration, while shape changes brought on by using bi-stable laminates only require a force to change the laminate from one equilibrium state to another. Shown in Figure 2.4 is a $[90_4, 0_4]^T$ laminate in its two equilibrium states.

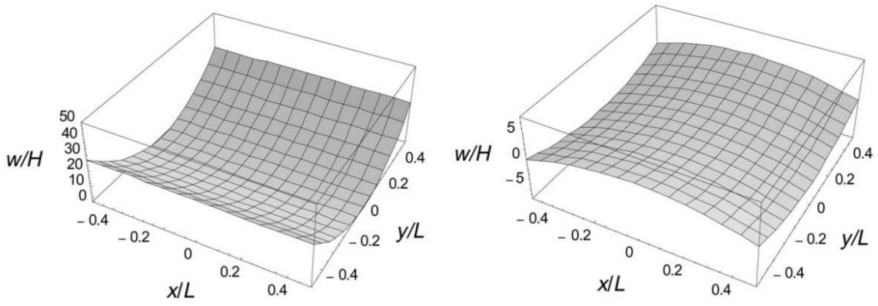

Figure 2.4: *Equilibrium State of* $[90_4, 0_4]^T$ *Laminate (Gude and Hufenbach, 2006)*

Piezo-ceramic actuators are still the preferred method of actuation, but requires only an impulse rather than a constant supply of power to change the shape of the wing due to the multiple equilibrium states of bi-stable laminates (Gude and Hufenbach, 2006).

Semi-analytical calculations can be done on systems as described above using the theory of Total Potential Energy along with the Rayleigh-Ritz method, which is used to obtain an approximate solution to the displacement field of the composite. This method can be used to calculate the equilibrium states of the composite as well as the applied force required to be delivered by the piezo-ceramic actuator and consequently, the necessary actuation voltage required (Dano and Hyer, 2001). Numerical simulation of bi-stable composites using piezo-ceramic actuators can be a difficult task but allows for the design and testing of more complex morphing laminate-actuators structures.

A method to model these systems in a Finite-Element environment is to use a package available from ANSYS, modeling the piezo-ceramic element as a

Stellenbosch University https://scholar.sun.ac.za

SOLID5-element and the bi-stable composite as a single SOLID64-element (Gude and Hufenbach, 2006). The ANSYS Finite-Element software package provides coupled-field brick elements that allow the electro-mechanical analysis of piezoelectric elements in conjunction with structural analyses performed on the bi-stable composite. To estimate the snap-through voltage of the composite, an electrical field is gradually applied to the piezo-ceramic element modeled in the Finite-Element environment until the composite shifts from its current equilibrium state to the next. According to the paper by Gude *et al.* (2011), the simulation strategy suggested above agreed well with results obtained experimentally. Using the methods described here, the snap-through voltage could easily be estimated for a wing utilising Piezo-ceramic actuators along with Asymmetric laminates as its deformation mechanism.

2.2.2 Corrugated Composite Skins

In the field of morphing aerodynamic structures, many designs utilise some form of anisotropic skin covering the base-structure of the wing. This skin is required to be stiff enough to withstand the aerodynamic forces experienced by the wing, while simultaneously remaining flexible enough to allow a sufficient shape change. This trade-off between flexibility and stiffness is a large concern in the field of morphing wings. One method proposed to solve this issue is by using Corrugated Composite Skins.

The highly anisotropic nature and good in-plane strain characteristics of composites make them ideal for morphing wing applications (Dayyani *et al.*, 2015). Gong *et al.* (2017) explored using shape memory polymers along with corrugated composites as reinforcement to produce a wing skin with different stiffness values along the length and width of the wing, while still offering a smooth and continuous aerodynamic surface. This specific structure uses a shape memory polymer with a stiffness that changes with temperature. Below the glass transition temperature, the polymer is stiff and does not allow large deformations, but with an increase in temperature, the polymer becomes flexible and more capable of large strains. The polymer also has the ability to harden after deformation, allowing the structure to lock into a current configuration without the need for a constantly applied force (Gong *et al.*, 2017). A concept of a corrugated composite skin using a shape memory polymer as actuator can be seen in Figure 2.5.

Another use of corrugated composite cores is the combination of corrugated composite cores with an an elastic polymer coating as done by Dayyani *et al.* (2015), where they applied this strategy to a FishBAC morphing wing design, as can be seen in Figure 2.6.

Stellenbosch University https://scholar.sun.ac.za

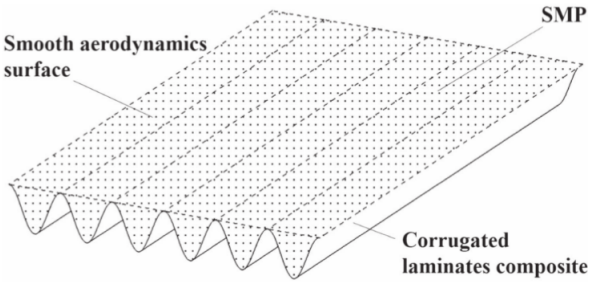

Figure 2.5: *Corrugated Composite Skin using Shape Memory Polymer as Actuator (Gong* et al.*, 2017)*

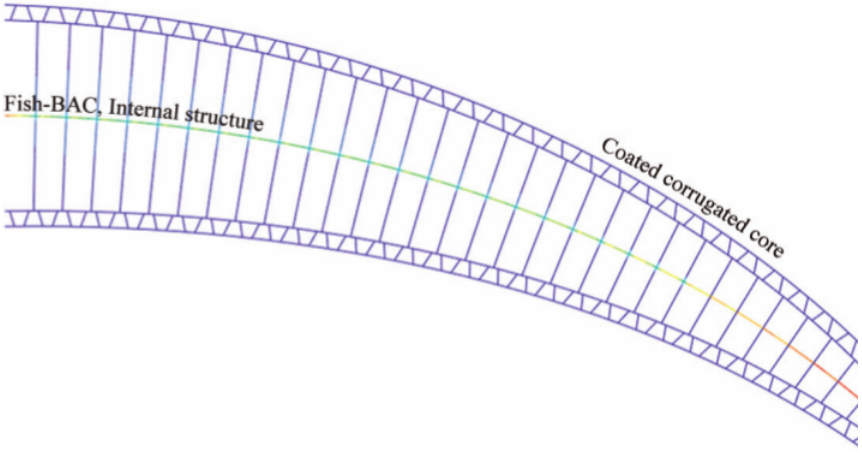

Figure 2.6: *Corrugated Composite Core with Elastic Polymer Coating (Dayyani* et al.*, 2015)*

The coating did ensure a smooth aerodynamic surface which aided in the reduction of drag produced, but increased both the in- and out-of-plane stiffness, resulting in a wing that showed a smaller useful shape change than its uncoated counterpart. (Dayyani *et al.*, 2015).

Strategies for modeling these corrugated composite structures analytically or in a Finite-Element environment and experimentally validating these results have been the focus of many studies. Derivations, experimental methods, experimental results, Finite-Element modeling and structural optimization techniques can be widely found in literature and will not be discussed in detail.

2.2.3 Shape Memory Structures

Shape Memory Structures is a branch of Smart Materials, consisting mainly of two categories namely Shape Memory Polymers (SMP) and Shape Memory Alloys (SMA). SMPs, like the polymer used by Gong *et al.* (2017) described in the previous section, are polymers that undergo substantial stiffness variations

Stellenbosch University https://scholar.sun.ac.za

when externally stimulated, usually by being heated. SMPs are usually stiff below their glass transition temperature, but become flexible and capable of large deformations when heated above this temperature.

SMAs are currently more favorable than SMPs since the maximum possible actuation force of SMAs is much higher. SMAs also undergo a shape change when a suitable stimulus, such as heating, is applied and is most often used with a pre-strain applied in the form of stretching. Much like SMPs, the SMAs have a critical temperature and when heated above this temperature the alloy reverts to its pre-stretched configuration. Upon cooling, the alloy does not revert to its stretched configuration and thus is used in conjunction with other deformation-creating devices such as springs or other elastic members (Sofla *et al.*, 2008).

Often SMAs are used in an antagonistic configuration consisting of two or more SMA structures, eliminating the need for additional deformation-creating members and thus reducing the weight and overall complexity of the structure (Lu *et al.*, 2001). An example of such a structure is a cantilever beam constructed by sandwiching a triangular corrugated core with two SMA plates as seen in Figure 2.7. These antagonistic actuating structures also have the benefit of not requiring continuous power to retain the new shape after deformation.

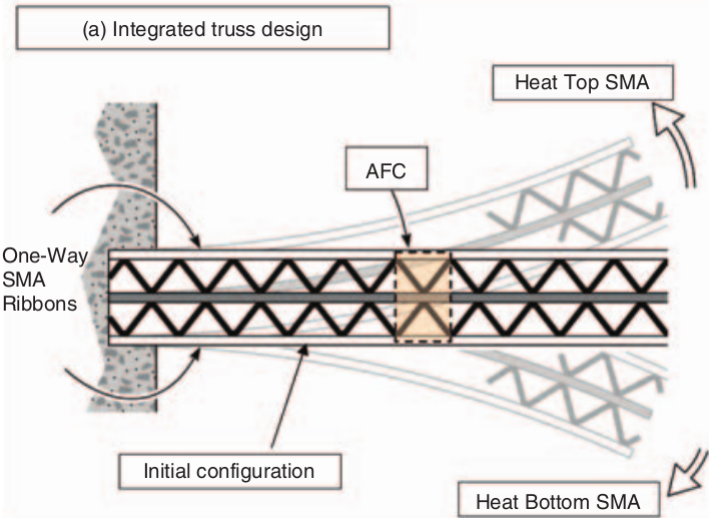

Figure 2.7: *Cantilever Beam formed of Antagonistic Flexural Cells (AFC) (Sofla* et al.*, 2008)*

SMAs do have a few drawbacks though. One major flaw is the difficulty to characterize their behavior, since it is highly non-linear and extremely depen-

Stellenbosch University https://scholar.sun.ac.za

dant on the history of the loading that was previously applied to the structure (Barbarino *et al.*, 2009). There have been many studies done to analytically determine the characteristics for these types of alloys, but for engineering applications, the focus was placed more on phenomenological models than analytical models. This avoided the use of difficult to measure constants such as free energy and made use of only clearly defined and measurable material constants.

In particular, the material models developed by Tanaka (1986) and Liang and Rogers (1990) can be easily implemented in a Finite-Element environment to analyze SMAs. Another major drawback in the context of morphing aerofoils is the slow response time SMAs display. There are strategies to accelerate the actuation time by using complementary heat sources to speed up the warm-up process (Barbarino *et al.*, 2009). A possible source of extra heat can be the exhaust gasses created by the aircraft during flight.

2.2.4 Inflatable Structures

Inflatable structures usually consist of a cellular internal structure covered by a skin with elastic or flexible properties. This internal structure allows morphing of the structure by varying the internal pressure of these cells. Morphing aerofoils mostly utilize pressurized cellular structures to achieve some form of camber manipulations, since camber manipulation is the simplest method to increase the lift generated by a wing (Vos *et al.*, 2011).

Finding the optimal shape for these cellular structures can be achieved by Topology Optimisation techniques, where the aim is to optimize the distribution of material within a topology that maximizes or minimize an objective function. Vasista and Tong (2012) had success in implementing the widely researched and documented Solid Isotropic Material with Penalisation (SIMP) method as well as the newer Moving Isosurface Threshold (MIST) technique to produce viable cellular shapes that can be incorporated to allow morphing.

Luo and Tong (2013) suggested a design for these cells with a hexagonal or rectangular shape, each having two curved walls as can be seen in Figure 2.8. These cell designs incorporate curved walls since the deformation of the curved walls allows for a larger actuation force in comparison to a configuration only using straight walls. When the pressure inside a cell is increased, the cell walls deform in bending due to the pressure difference between the pressurized and void cells, which leads to the overall deformation of the structure (Luo and Tong, 2013).

Vos *et al.* (2011) also suggested a design for internal cellular structures, namely the Pressure Adaptive Honeycomb (PAH). It has been claimed by the design-

Stellenbosch University https://scholar.sun.ac.za

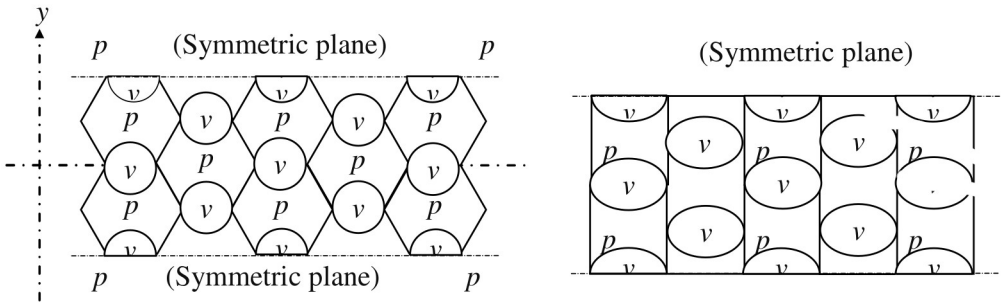

Figure 2.8: *Proposed Cellular Structure Designs, with 'P' referring to Cells that can be pressurised and 'V' Empty Void Cells [Hexagonal, Left; Rectangular, Right] (Luo and Tong, 2013)*

ers that their design can easily be FAA/EASA certified, since it uses well-characterized materials that are arranged in such a way that high levels of structural adaptability are possible, whereas designs from other sources do not necessarily comply to FAA/EASA standards (Vos *et al.*, 2011). The PAH design by Vos *et al.* (2011) can be seen in Figure 2.9.

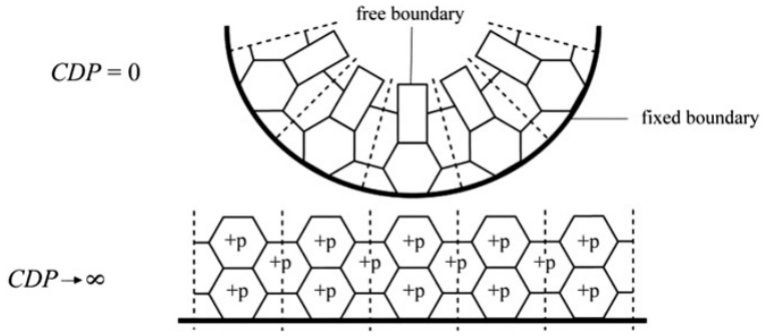

Figure 2.9: *Pressure Adaptive Honeycomb Design [Top, Unpressurized; Bottom, Pressurised] (Vos* et al.*, 2011)*

Feng *et al.* (2015) followed a completely different approach. Instead of relying on an inflatable internal structure to alter the shape of the structure, a morphing skin was proposed. The proposed skin, which can be seen in Figure 2.10, consists of a flexible skin embedded with bio-inspired pneumatic muscle fibers.

The morphing skin forms the bottom surface of the wing and operates in conjunction with a carbon fiber skin, which forms the top surface of the wing. In this configuration, the upper surface of the wing is much stiffer than the lower surface and by varying the pressure in the pneumatic muscle fibers the camber profile of the wing changes (Feng *et al.*, 2015). A diagram of the wing

Stellenbosch University https://scholar.sun.ac.za

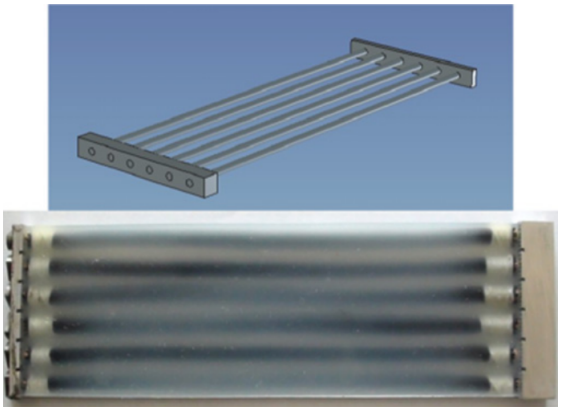

Figure 2.10: *Morphing Skin with Embedded Pneumatic Muscle Fibres Coated with an Opaque Film [Top, CAD; Bottom, As Implemented in a Wing Model] (Feng* et al.*, 2015)*

assembly can be seen in Figure 2.11.

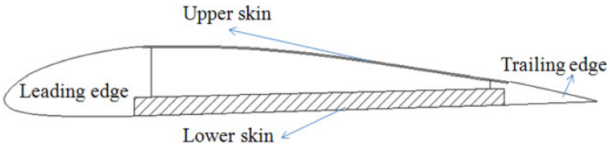

Figure 2.11: *Proposed Wing Assembly (Feng* et al.*, 2015)*

In the configuration displayed in Figure 2.11, the pneumatic muscle fibers are fully active and the wing shape has the least amount of camber from all its other possible forms. When this form of least camber is required, constant actuation of the pneumatic muscle fibers, achieved through a continuously applied pressure force, is necessary. This need for constant actuation results in an increase in energy consumption and will lower the overall energy efficiency of the wing if it is intended to operate in this shape for extended periods.

Another recent development in the field of inflatables is Tensairity. Tensairity is the combination of inflatable structures with cables and struts, increasing the stiffness and load-bearing capabilities of the inflatable structure tremendously. The most basic Tensairity structure consists of a compression element, a low-pressure air-beam that is tightly connected to the compression element and two tension elements that run from end to end of the compression element in a spiral fashion around the air-beam. This basic structure can be seen below in Figure 2.12.

Inflatable aerofoils are already in widespread use for low-speed applications such as kite-surfing. These aerofoils are usually very flexible and have very

Stellenbosch University https://scholar.sun.ac.za

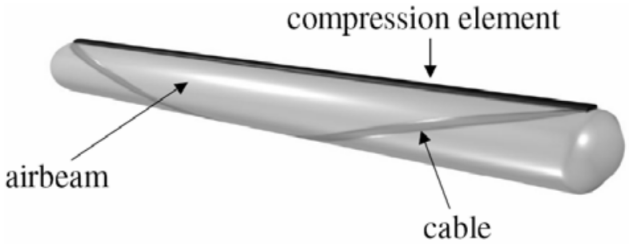

Figure 2.12: *Basic Tensairity Structure (Breuer* et al.*, 2007)*

little load-bearing capacity (Breuer and Luchsinger, 2010). The concept of Tensairity overcomes this deficiency. The Tensairity concept can even be further stiffened by introducing fabric webs into the air-beam. The concept of Tensairity has already been implemented in the field of morphing aerofoils by Breuer *et al.* (2007). The concept developed consisted of a multi-spar wing with two discrete Tensairity elements included. A schematic of the design can be seen in Figure 2.13, with the black dots representing the location of the Tensairity compression and tension members. The surface of the wing was also covered with a polymer skin to ensure a smooth outer surface is present.

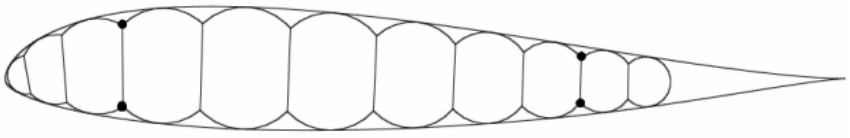

Figure 2.13: *Tensairity Wing Design(Breuer* et al.*, 2007)*

Another recent implementation of Tensairity in the field of flexible aerofoils was the development of a Tensairity Kite by Breuer and Luchsinger (2010). The goal of the research was to use the concept of Tensairity to develop a stable kite that flies using only a single tether. The eventual product of this research was an 11 m^2 kite that consists of one main Tensairity spar with a web in the span-wise direction to resist the bending load and several Tensairity struts in the chord direction to tension the entire lifting surface. The final design weighed only 2.5 kg and used a single tether fixed to two points on the center strut. In Figure 2.14 the final design of the Tensairity Kite can be seen.

A recent research paper published by Ou *et al.* (2016) from the Massachusetts Institute of Technology also discussed the possible use cases of using inflatable structures as actuators. The paper titled *Aeromorph*, focuses on developing shape-changing inflatable actuators from various materials utilizing selective reinforcement. This selective reinforcement is done by bonding the material at strategic locations to create a desired deformation once the structure is inflated.In Figure 2.15 a few possible inflatable structures created through the

Stellenbosch University https://scholar.sun.ac.za

Figure 2.14: *Developed Tensairity Kite Prototype with a Total Surface area of 11 m^2 and 7.8 m Span (Breuer and Luchsinger, 2010)*

Aeromorph research can be seen.

For these designs, heat-sealing was used as the method of reinforcement through the placements of seals at certain regions of the inflatable. The structure will hinge or curve along the seal since an inflatable structure strives to become spherical when inflated and assuming the material cannot stretch the sides of the airbag tends to curve inward, implying a compressive deformation on the lateral seams (Ou *et al.*, 2016). The newly added seal can be seen as a common or shared seal between two air-pockets and thus for the internal forces of the structure to be in static equilibrium, the two adjacent air-pockets must bend around the shared seal until the volume of the structures is maximized. This principle is illustrated in Figure 2.16, with the solid and dashed lines representing the uninflated and inflated shape, respectively. Also visible in Figure 2.16 is the resultant compressive force acting on the lateral seams responsible for the inward curving of the sides of the airbag.

In cases such as these where heat is used as the bonding or sealing method, the bending action will always tend toward the surface where heat was applied to, since the application of heat weakens the material marginally and forms a type of folding-crease on the surface, making the resistance to bending slightly less in that region compared to the material of the seal located on the opposite surface (Ou *et al.*, 2016). In Figure 2.15 the solid lines in the top images represent seals applied on the top surface, where dashed lines represent seals applied from the bottom surface.

The actuators developed during the *Aeromorph* research focus mostly on the different types of deformations possible and how the various design parameters of the actuator can affect its inflated shape. In Figure 2.17, designs for an actuator are shown that induces a bending angle when inflated. Three seal geometries were investigated to induce this deformation, namely a straight line seal, a curved arc seal and lastly a diamond seal. The parameters of the shapes

Stellenbosch University https://scholar.sun.ac.za

Figure 2.15: *Examples of Possible Actuators Developed through the Aeromorph Research [Top, Bonding Pattern for Inflatable; Bottom, Resulting Inflatable (Ou* et al.*, 2016)*

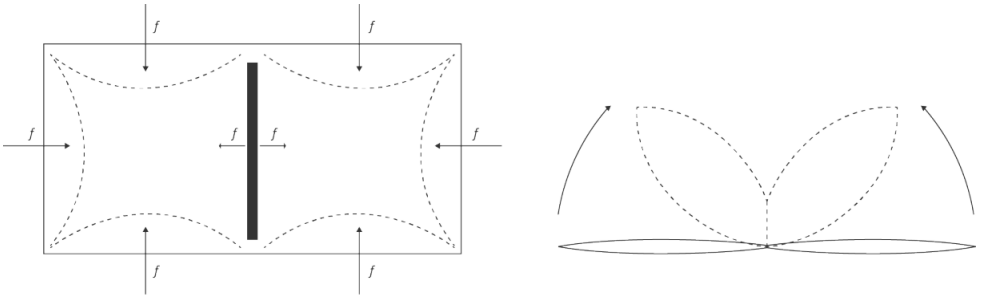

Figure 2.16: *Bending Deformation of Two Adjacent Air-pockets Sharing a Common Seal (Ou* et al.*, 2016)*

can be varied to alter the bending angle achieved once the structure is fully inflated. It was discovered that the diamond shape allowed a greater range as well as better control over the bending angles compared to the curved arc or straight seal and also proved to be much a much stiffer hinge than the other two alternatives (Ou *et al.*, 2016).

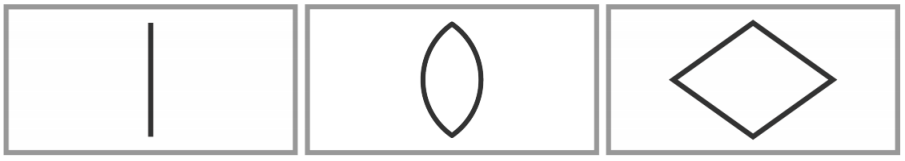

Figure 2.17: *Seal Geometries Investigated to Induce a Bending Angle Once Inflated [Left, Straight Line Seal; Middle, Curved Arc Seal, Right, Diamond Seal] (Ou* et al.*, 2016)*

In Figure 2.15 a range of actuators using a diamond seal geometry is shown, each with a different aspect ratio to demonstrate the relationship between the seal geometry and the resulting fully-inflated bending angle. The potential of

Stellenbosch University https://scholar.sun.ac.za

using this type of actuator as a rudimentary wing flap mechanism with a fixed bending-angle is evident.

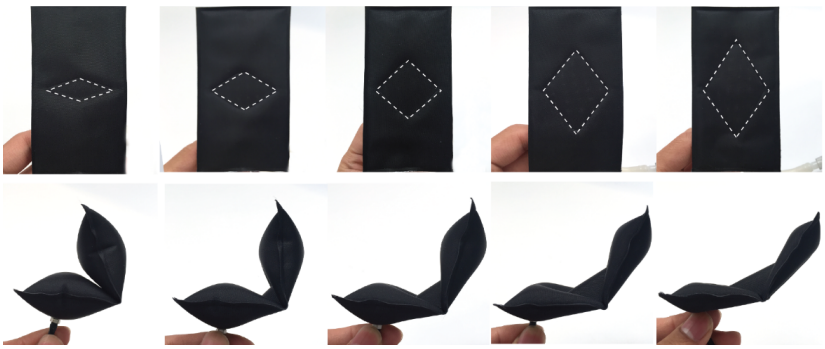

Figure 2.18: *Example of a Possible Actuator that can be used in the Design of a Morphing Wing with Different Seal Aspect Ratios(Ou* et al.*, 2016)*

2.2.5 Kagome Truss Structures

Kagome Truss structures are a class of planar pin-jointed structure based on the ancient Kagome basket weave pattern, which consists of a combination of hexagons and triangles as can be seen in Figure 2.19. These types of structures have been identified to have excellent actuation characteristics, in-plane isotropic stiffness as well as having optimal weight compared to other trusses for a specified stiffness or strength (Hutchinson *et al.*, 2003).

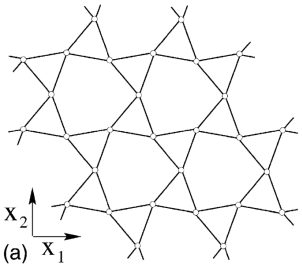

Figure 2.19: *Kagome Weave Pattern (Hutchinson* et al.*, 2003)*

Many Kagome Truss-based structures exist, two popular configurations being a tetrahedral truss core sandwiched between two Kagome truss faces or one Kagome truss fixed to a solid face. These two configurations are displayed in Figure 2.20.

dos Santos e Lucato *et al.* (2004) used this concept of Kagome trusses to generate a concept for a morphing structure capable of complex shape changes.

Stellenbosch University https://scholar.sun.ac.za

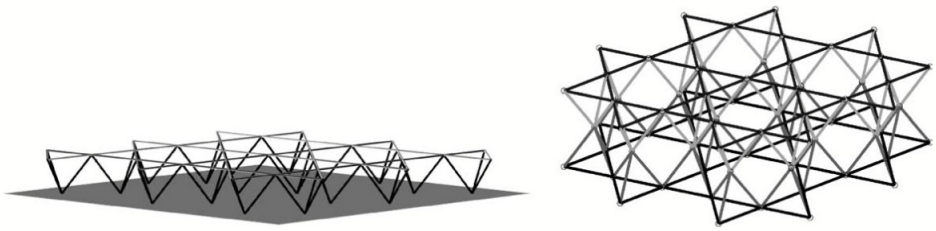

Figure 2.20: *Popular Kagome Truss Configurations [Left:Kagome truss and Solid Face-sheet, Right: Two Kagome Truss Faces] (Hutchinson* et al.*, 2003)*

This structure consisted of a solid face-sheet with a Kagome backplane (see Figure 2.20) and is rigidly supported at one end. To allow actuation of the structure, certain truss members of the tetrahedral truss core were replaced with linear actuators. In Figure 2.21, the mentioned design can be seen.

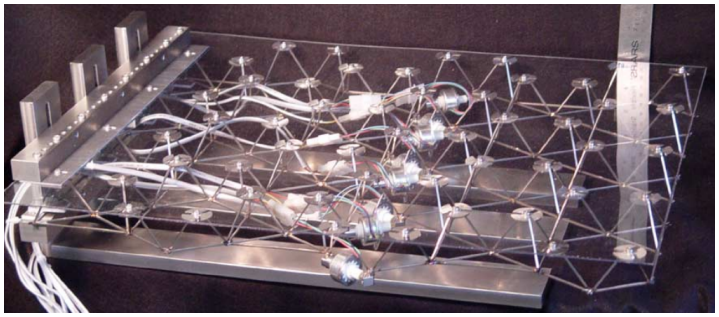

Figure 2.21: *High Authority Morphing Structure Using A Kagome Structure and Linear Actuators(dos Santos e Lucato* et al.*, 2004)*

The structure developed can be incorporated into a morphing wing design with some minor adjustments, however, the overall structure is very complex and failure of any linkage could be detrimental and can even render the wing inoperable, since each linkage is vital to the function of the structure.

Stellenbosch University https://scholar.sun.ac.za

Chapter 3

Methods

The following chapter provides a description of the various methods and/or tools used throughout this research. Some comparisons between similar methods and tools are also discussed to justify why certain methods were chosen above other available options. Included in this chapter are descriptions of the fabrication methods, the utilised design approach, numerical form-finding and simulation techniques, the 3D-scanning method used, as well as the Design of Experiment procedure. A brief description is also given on coding-scripts that were developed for this project as well as any software that was implemented.

3.1 V-model Design Approach

The V-model is a methodology typically used in system design and consists of various processes ordered in a cascading manner. The V-model is constructed in such a manner that the flow of time is indicated by movement from the left towards the right of the diagram (Mathur and Malik, 2010). In Figure 3.1, the layout of the V-model used during this project can be seen.

At the top of the V-model is the conception of the design. In this stage, the abstract problem is framed and research is done into previous similar designs as well as technology available to realize the design concept. The next step is the formulation of engineering requirements, detailing what specific functions the design has to fulfil. During the broad system design, a general layout of the design is formed, consisting of the different systems each with a specific task that makes up the design as well as how these systems will interact.

After the broad system design has been completed, sub-system design can commence. In this phase, the broad systems are further split into sub-systems and the components forming the sub-systems are fully defined. The next phase consists of combining all the different sub-systems to form the general system as defined during the broad system design. Next testing and refinement of the

Stellenbosch University https://scholar.sun.ac.za

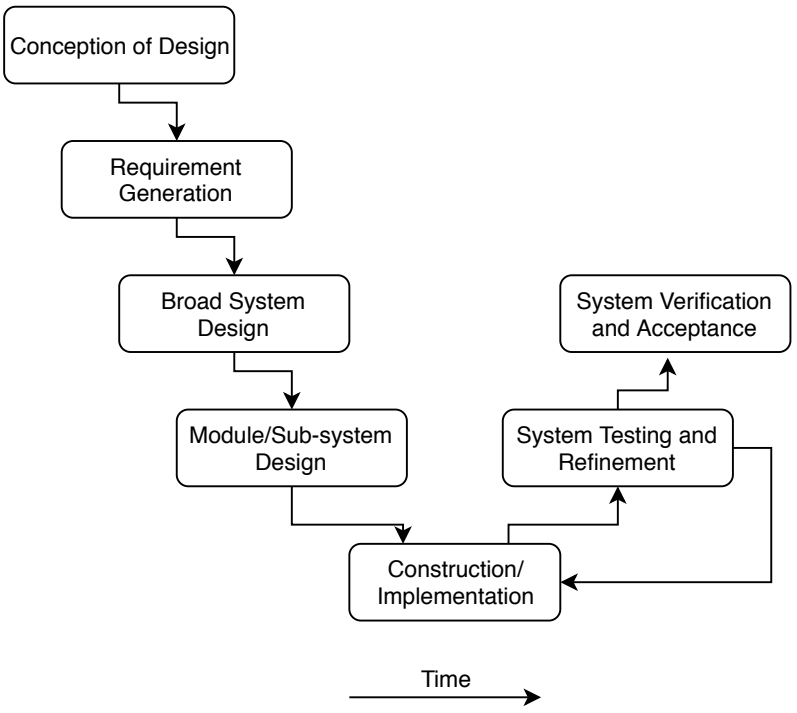

Figure 3.1: *V-model Design Approach Used for this Project Showing the Various Processes in a Cascading Manner. The Flow of Time is Indicated by Movement from the Left of the Diagram Towards the Right.*

constructed system starts, with the construction/implementation process repeating until the system performance during testing, is at a satisfactory level. The final step in the design process is the verification of the overall system and if the system satisfies the requirements as defined in the second phase of the process.

3.2 Fabrication Methods

As a large quantity of commercial-grade low-density polyethylene was available, it was decided to use this as the bulk material for the wing structure where possible. Due to this decision a suitable fabrication method had to be determined that sufficiently bonded the material to allow the construction of tubes-like structures as well as other components. The fabrication methods considered can be split into two broad categories namely heat-binding and ultrasonic welding.

Ultrasonic welding is the process of binding two components through the use of a tool vibrating at a high-frequency. The tool is then pressed against the joint

Stellenbosch University https://scholar.sun.ac.za

location of the two components resulting in a weld formed through friction-heating. Although ultrasonic welding works well to bind low-density polyethylene it did require expensive equipment to be purchased. The cost of the needed equipment made this choice unfeasible, since an objective of the project was to create a low-cost wing.

Heat-binding is the process of binding two similar thermoplastics together by the application of both direct heat and pressure. Three methods of heat-binding were considered for the fabrication method. The first method used consisted of a self-made sealing press constructed from a wooden bar covered with a thin silicone coating. A nickle-chromium wire was placed on top of this silicone layer and was used as the heating element for the sealing process. To prevent the wire from sticking onto the polyethylene during the sealing process, a layer of Teflon tape was applied over the wire. ordinary bench-top power-supply capable of delivering a maximum output of 216 W, the wire was heated through a joule-heating process.

This method however proved ineffective since the current drawn from the power-supply was limited by the low resistance of the nickle-chromium wire, resulting in insufficient heat produced throughout the wire to create a strong bond between two layers of polyethylene sheeting. In Figure 3.2, the sealing press used can be seen.

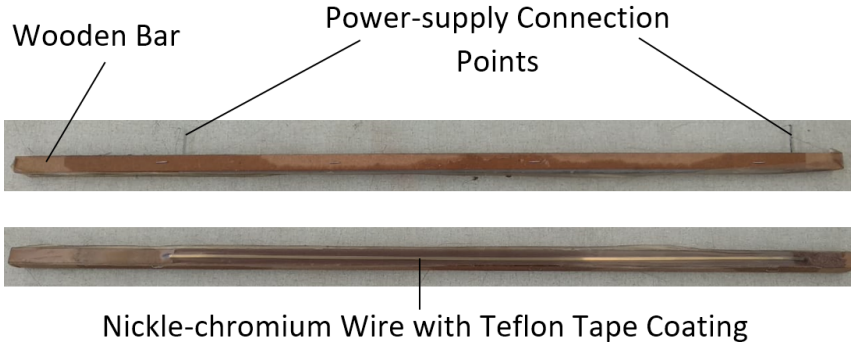

Figure 3.2: *Sealing Press Constructed from a Wooden Bar, Thin Layer of Silicone and a Nickle-chromium Wire Coated with Teflon Tape used as the Heating Element*

Alternatively, a commercial 5000 W foot-operated heat-sealer was used, which proved sufficient in binding multiple layers of polyethylene sheeting, but the bond locations were severely limited by the jaws of the device allowing the material to only move a finite distance past the clamping location. In Figure 3.3, a foot-operated heat sealer similar to the one used can be seen.

Stellenbosch University https://scholar.sun.ac.za

Figure 3.3: *Conventional Foot-operated Heat-sealer with the Jaw-configuration Allowing Plastic Sheeting to only Move a Finite Distance Passed the Seal Location*

To allow for more versatility in the bond locations, a soldering-iron set to 300°C equipped with a 3.2 mm soldering-tip was used to bond the material. Using this method intricate and complex joints were possible, but creating seals without any defects proved challenging due to the nature of the sealing technique.

Effectively sealing multiple layers with the soldering-iron sealing method also proved somewhat challenging. To remedy this issue, it was decided to use both the soldering-iron sealing method in conjunction with the foot-operated heat-sealer, with the soldering-iron responsible for all intricate single-layer seals, while the foot-operated heat-sealer would be used for multi-layer sealing purposes.

3.3 3D-scanning

3D-scanning is the process of capturing digital information regarding the shape of an objects that can then be used to create a 3D computer model of the scanned item. Due to equipment available, structured-light 3D-scanning was selected as the 3D-scanning method of choice. 3D-scanning was used during this project to create digital models of constructed prototypes for further analysis and manipulation.

The most basic structured-light 3D-scanner consists of a light source and one camera. An additional camera is often added to the configuration to increase the scanning accuracy and the field-of-view of the scanner. The light source

Stellenbosch University https://scholar.sun.ac.za

is used to project a pattern onto the surface of the object, while the cameras are used to detect and capture the distortions in the projected pattern caused by the shape of the object. The data as captured by the cameras is then used by the 3D-scanning software to calculate the depth as well as other surface information of the object. This process is done by using the known distance between the cameras and the light-source as well as the angle between the two through a process called triangulation, which is displayed graphically in Figure 3.4 (Chougule *et al.*, 2018).

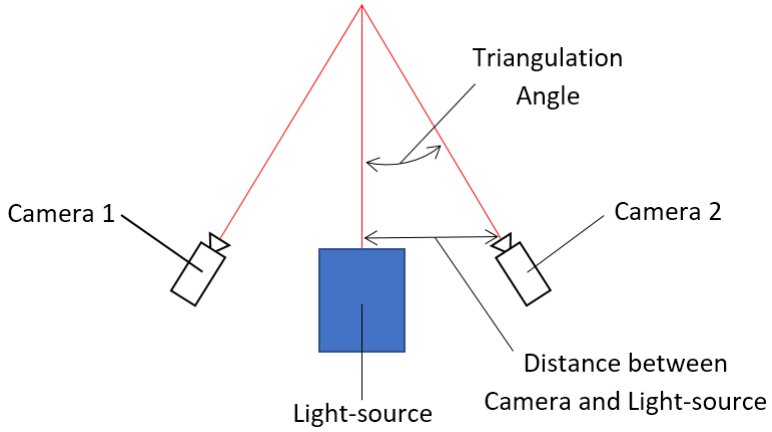

Figure 3.4: *Angle and Distance used for the Triangulation Process to Calculate the Depth of a Point on the Surface of the Scanned Object. The Target Object is Located at the Convergence Point of the Light-source and the Line-of-sight of the Two Cameras.*

Through this process a mesh of points is created which can then be used to create a digital model of the surface of the object. This process however only creates a digital 3d-model of the object surface currently in the view of the cameras. To create a model of the entire object this process is then repeated for a chosen number of object orientations, which are merged during post processing to form a complete 3d-model of the scanned object.

A major challenge with this type of 3D-scanning is the difficulties caused by transparent, reflective or dark surfaces (Mitas *et al.*, 2014). Objects with reflective surfaces prove difficult to scan due to the reflection of the projected pattern exceeding the dynamic range of the cameras. Objects with dark surfaces, especially black, result in the cameras being unable to differentiate between the various components of the pattern and the surface of the object, resulting in a lack of pattern visibility and consequently a failed scan. With transparent objects, most of the light responsible for the pattern generation passes through the object, again resulting in a lack of pattern visibility and a unsuccessful scan. To overcome these issues, it has become common practice

Stellenbosch University https://scholar.sun.ac.za

to coat the object to be scanned with a thin opaque layer to allow the cameras to successfully identify the generated pattern and capture the surface data of the object (Mitas *et al.*, 2014).

3.4 Image Tracking

Image tracking was predominantly used to measure the bending deformation of the various prototypes constructed during this project. Image tracking was chosen, since it allowed the measurement of bending deformations while allowing unrestricted motion of the prototype. For this process *Tracker* was mused. *Tracker* is an open-source video and image analysis tool built on the Open Source Physics (OSP) Java framework. It is predominantly used for physics problems and offers a wide range of features such as manual and automated object tracking as well as data extraction and basic model or curve fitting. *Tracker* also features some rudimentary video and image manipulation tools such as the ability to add filters or overlays, frame cropping as well as basic colour corrections. (Brown, 2006)

For the research presented here, *Tracker* was predominantly used for its image tracking capabilities. In Figure 3.5, a typical example of the tracking capabilities of *Tracker* can be seen. The red dot seen on the prototype in Figure 3.5 is the chosen point that the software tracks relative to the user-defined axis or reference frame shown in pink. To find the angle change of the prototype the dot angle relative to the user-defined axis is measured in both the symmetric and cambered shape. The angle change is then calculated by subtracting the smaller value of the two from the larger value.

Tracking of points can either be done via manual tracking or automatic tracking. With manual tracking the user is asked to click on the point of interest in each frame of the video. This tracking style is best suited for determining physical properties, such as angles between objects, from a still image rather than a video. For videos auto-tracking is more suitable, since it reduces the user-input by automating the process of manual-tracking. To use auto-tracking, a clearly identifiable marker is to be placed on the point of interest of the tracked object. This is done to allow the software to easily distinguish the point of interest from the background to allow successful tracking over multiple frames.

Another feature of *Tracker* used during this project was the built-in circle fitting algorithm. The algorithm works by having the user specify a minimum of three points on the perimeter of the circle and then by using a least-squares algorithm the center-point and radius of the circle is determined (Brown, 2006). In Figure 3.6, an example of such a circle fit done on a prototype actuator can be seen.

Stellenbosch University https://scholar.sun.ac.za

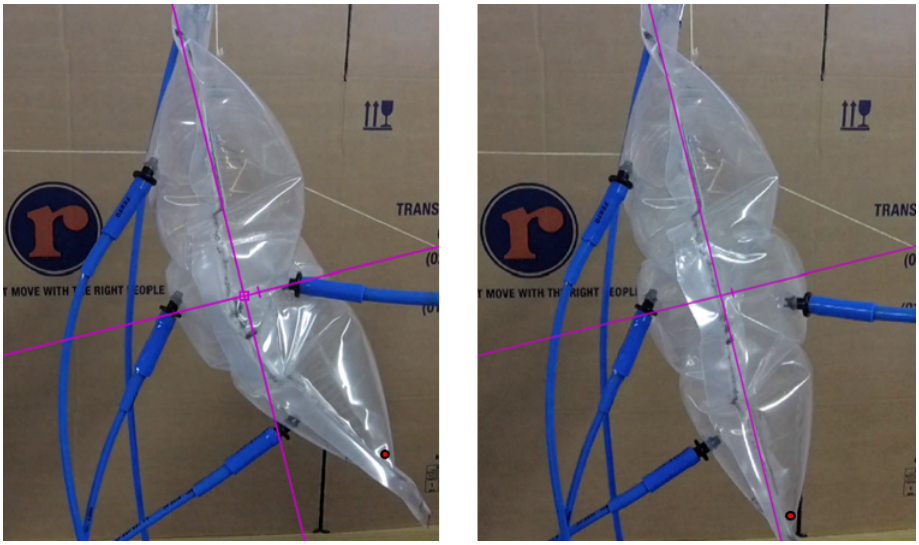

Figure 3.5: *Example of Tracker Deformation Measurement. Measured Deflection Angle Between Left and Right Image = 24°*

Figure 3.6: *Example of Circle Fit done through the Use of the Built-in Circle Fitting Algorithm Available in Tracker. 11 Points were Specified to be on the Perimeter of the Circle for this Example Fit*

3.5 Generation of Prototype Construction Parameters

To simplify the wing design process a Python-script was developed to extract certain construction parameters from an industry standard aerofoil. For this purpose the NACA 4-digit series aerofoils were selected. In the NACA 4-digit

Stellenbosch University https://scholar.sun.ac.za

system, the first digit specifies the maximum camber as a percentage of the chord length, the second digit the location of the maximum camber as measured from the leading edge of the aerofoil and the last two digits the maximum thickness as a percentage of the chord length.

It was decided to limited the script to only generate symmetric NACA aerofoils. This choice simplified the overall geometry of the aerofoil while simultaneously limited the number of user inputs necessary to fully define the 4-digit NACA aerofoil since with a symmetrical aerofoil the first two digits of the NACA aerofoil is reduced to zero, meaning only the chord length and the the maximum thickness needs to be specified by the user to fully determine the NACA aerofoil.

The choice of using a symmetric NACA aerofoil also simplified the coding procedure since a parametric equation is available that describes half of a symmetric 4-digit NACA aerofoil, which when mirrored over the x-axis produces a complete aerofoil. The general 4-digit NACA Equation can be seen in Equation 3.5.1. As this script is intended to be utilised with a completely inflatable wing consisting of multiple chambers created by placing vertical spars at certain locations, the user is also prompted for the number of desired chambers in addition to the chord length and maximum percentage thickness.

$$y = 5Lt\left[0.2969\sqrt{x} - 0.1260x - 0.3516x^2 + 0.2843x^3 - 0.1015x^4\right] \quad (3.5.1)$$

$L =$ Chord Length; $\quad t =$ Percentage Maximum Thickness; $\quad x = 0$ to 1

The script utilises the input variables and calculates certain construction parameters such as the spar locations, the edge length between consecutive spars forming a chamber and also generates a visual representation of the coinciding 4-digit NACA aerofoil with the vertical spars added. An example output of the script can be seen in Figure 3.7

Stellenbosch University https://scholar.sun.ac.za

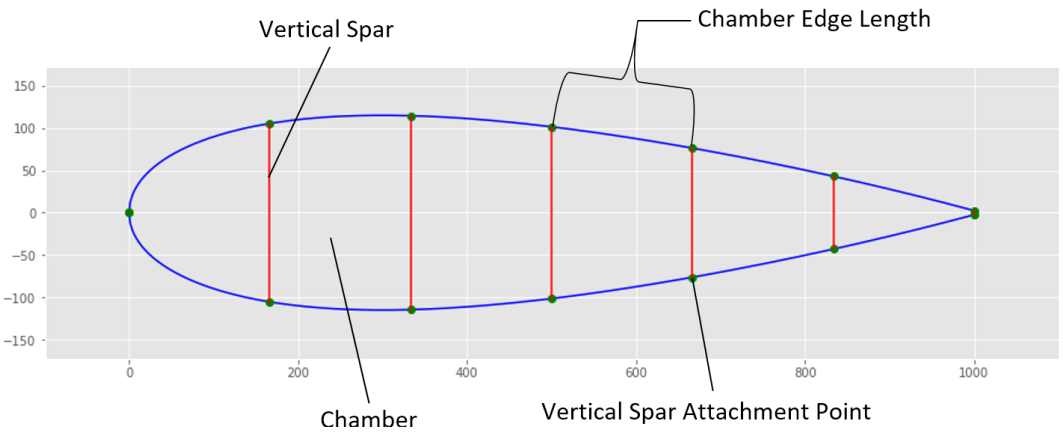

Figure 3.7: *Example of a Script Generated 4-digit NACA Aerofoil with a Chord Length of 1000 mm, a Maximum Percentage Thickness of 0.23 and Six Inflatable Chambers.*

3.6 Numerical Form-finding Methods

As this project relied on an iterative design approach, a method was desired to estimate the final shape of a design before a prototype was constructed. To do this, it was chosen to incorporate a simulation method into the Python-script described in Section 3.5. To simplify the overall simulation process it was decided to only simulate the centre-line cross-section of the wing design, effectively reducing the simulation to a two-dimensional problem. For this process two form-finding methods were investigated namely Dynamic Relaxation and the Force Density Method.

3.6.1 Background of Methods

Dynamic Relaxation (DR) is based on the fact that a system undergoing damped vibration ultimately comes to rest in the displaced static equilibrium position. DR discretises the mass of the entire system and distributes the mass to the nodes, which oscillate about the equilibrium position (Mohammed Elmardi Osama, 2016). By introducing artificial inertia and damping values (denoted ρ and k), the system is forced to converge to some static displaced position, resulting in DR only calculating the final shape of the structure and not the form of the structure at various time-steps. This makes DR particularly suited to form-finding approaches where only the final shape is of interest.

DR aims to solve the differential equation of motion displayed in Equation 3.6.1 for each node of the structure. The displacement of each node is iteratively calculated until the velocity of the node is equal to zero or below a predefined threshold. Once the velocity is deemed negligible, the displacements of the

Stellenbosch University https://scholar.sun.ac.za

node at static equilibrium is known and thus the shape of the structure at equilibrium is also known.

$$f = \rho \frac{\partial^2 u}{\partial t^2} + k \frac{\partial u}{\partial t} \tag{3.6.1}$$

$$\text{With: } u = \text{Displacement; } \frac{\partial u}{\partial t} = \text{Velocity; } \frac{\partial^2 u}{\partial t^2} = \text{Acceleration}$$

Using the velocities before and after a period δt denoted by the subscript n and n-1 respectively and using finite differences in time as well as specifying the function value at the half-step $n - \frac{1}{2}$, Equation 3.6.1 can be rewritten in the form displayed in Equation 3.6.2.

$$f_{n-\frac{1}{2}} = \left(\frac{\rho}{\Delta t}\right)\left[\left(\frac{\partial u}{\partial t}\right)_n - \left(\frac{\partial u}{\partial t}\right)_{n-1}\right] + \left(\frac{k}{2}\right)\left[\left(\frac{\partial u}{\partial t}\right)_n - \left(\frac{\partial u}{\partial t}\right)_{n-1}\right] \tag{3.6.2}$$

Equation 3.6.2 can then be rewritten to calculate the velocity after the time step Δt and can then be used to calculate the displacements at the middle of the next time-step $n + \frac{1}{2}$ by integrating the velocity, leading to Equation 3.6.3.

$$u_{n+\frac{1}{2}} = u_{n-\frac{1}{2}} + \left(\frac{\partial u}{\partial t}\right)_n \Delta t \tag{3.6.3}$$

The iterative process starts at t=0 with all initial values of the velocity and displacements set to suitable values. In the first iteration the velocities and displacements are obtained through the respective use of Equation 3.6.2 and Equation 3.6.3. The boundary conditions are then applied, with the subsequent iterations following the same process as the first until the desired level of accuracy is reached.

The Force Density Method (FDM) uses a geometric stiffness approach rather than a time-dependent approach to solve for the equilibrium position of a structure (Schek, 1974). FDM works by descretizing a structure into a finite number of one-dimensional elements called nodes, with the connection between nodes called branches. For the system to be in static equilibrium, each node of the structure must also be in static equilibrium. The FDM takes all external forces applied to the system and distributes it to the nodes, with force transferred between nodes through the connecting branches. The equilibrium equation for all the nodes of the system is displayed in Equation 3.6.4. The matrix $\boldsymbol{D}$ represents the Force Density matrix, which is a function of the internal forces experienced at each node and the length of each branch, the vector $\boldsymbol{X}$ represents the nodal coordinates and $\boldsymbol{P}$ represents the load vector which is a function of all unbalanced forces experienced at the nodes.

$$\boldsymbol{DX} = \boldsymbol{P} \tag{3.6.4}$$

Stellenbosch University https://scholar.sun.ac.za

To construct these vectors and matrices, consider the 2D discretized structure shown in Figure 3.8, consisting of three nodes and two branches. In a general sense the index j is used to indicate the element number. The first and second node of an element are respectively represented by i and k. In Figure 3.8 $j = a; b; c$, $i = 1$ and $k = 2, 3$. External loads experienced by the structure are lumped together and distributed across the nodes and denoted by P_1,P_2 and P_3 in Figure 3.8.

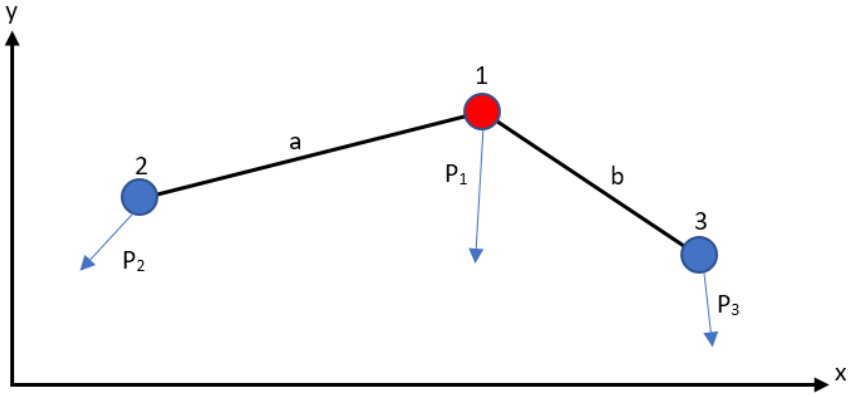

Figure 3.8: *Example of a discretized Structure Consisting of Three Nodes and Two Branches*

By applying Newton's Second Law to each node a relationship can be found between the internal forces, the node locations, the branch lengths, and the externally applied forces. For the case shown in the figure, the resulting equation for the x- and y-direction after applying Newton's Second Law is shown respectively in Equation 3.6.5 and Equation 3.6.6.

$$S_{\mathrm{a}}\left[\frac{x_1 - x_2}{L_{\mathrm{a}}}\right] + S_{\mathrm{b}}\left[\frac{x_1 - x_3}{L_{\mathrm{b}}}\right] = P_{1,x} \tag{3.6.5}$$

$$S_{\mathrm{a}}\left[\frac{y_1 - y_2}{L_{\mathrm{a}}}\right] + S_{\mathrm{b}}\left[\frac{y_1 - y_3}{L_{\mathrm{b}}}\right] = P_{1,y} \tag{3.6.6}$$

Transforming the equations shown in Equation 3.6.5 and Equation 3.6.6 to a more general sense, the following equations are found for the respective x- and y-direction.

$$\sum_{j=1}^{n} S_j\left[\frac{x_{j,i} - x_{j,k}}{L_j}\right] = P_{j,x} \tag{3.6.7}$$

$$\sum_{j=1}^{n} S_j\left[\frac{y_{j,i} - y_{j,k}}{L_j}\right] = P_{j,y} \tag{3.6.8}$$

Stellenbosch University https://scholar.sun.ac.za

Introducing the idea of force density (q), which is the internal force of each element divided by the element length and introducing u and v as the coordinate differences, Equation 3.6.7 and Equation 3.6.8 can be rewritten in the form shown in Equation 3.6.9 and Equation 3.6.10.

$$\sum_{j=1}^{n} q_j u_j = P_{j,x} \tag{3.6.9}$$

$$\sum_{j=1}^{n} q_j v_j = P_{j,y} \tag{3.6.10}$$

$$\text{With:} \quad u_j = (x_{j,i} - x_{j,k}); \quad v_j = (y_{j,i} - y_{j,k}); \quad q_j = \frac{S_j}{L_j}$$

A new matrix named the Connectivity matrix (C_s) is now introduced and is used to relate the branches to the nodes connected to it. In the Connectivity matrix the first node (i) of an elements is assigned a 1 and the second node (k) is assigned a -1. For all nodes not connected to element a zero is assigned. By constructing the Connectivity matrix in such a way that the free nodes are listed first and the fixed nodes second, the Connectivity matrix can be split into a free and fixed Connectivity matrix, denoted respectively by C and C_f. Using this principle of separating the free and fixed nodes, the system coordinates, denoted by x_s, can also be split into its free and fixed components denoted respectively by x and x_f. Using these new matrices, the coordinate differences can now be converted to a matrix form as shown in Equation 3.6.11 and Equation 3.6.12.

$$\boldsymbol{u} = \boldsymbol{C_s x_s} = \boldsymbol{C x} + \boldsymbol{C_f x_f} \tag{3.6.11}$$

$$\boldsymbol{v} = \boldsymbol{C_s y_s} = \boldsymbol{C y} + \boldsymbol{C_f y_f} \tag{3.6.12}$$

Grouping all the element force densities in a row vector (Q) and using all newly the newly defined coordinate difference matrix and Connectivity matrix, the equilibrium equation shown in Equation 3.6.4 can now be rewritten in terms of these components, in its complete or separated form. In Equation 3.6.13 and Equation 3.6.14 the new equilibrium equations for the x- and y-direction can be seen.

$$\boldsymbol{C}^T \boldsymbol{Q} u = \boldsymbol{C}^T \boldsymbol{Q} \left(\boldsymbol{C_s x_s} = \boldsymbol{C x} + \boldsymbol{C_f x_f}\right) = \boldsymbol{P_x} \tag{3.6.13}$$

$$\boldsymbol{C}^T \boldsymbol{Q} v = \boldsymbol{C}^T \boldsymbol{Q} \left(\boldsymbol{C_s y_s} = \boldsymbol{C y} + \boldsymbol{C_f y_f}\right) = \boldsymbol{P_y} \tag{3.6.14}$$

Simplifying Equation 3.6.13 and Equation 3.6.14 and rewriting, two equations are formed for calculating the static x- and y-equilibrium position of the nodes. These equations can be seen in Equation 3.6.15 and Equation 3.6.16. Using these equations along with an initial guess for the force-density matrix ($\boldsymbol{Q}$)

Stellenbosch University https://scholar.sun.ac.za

and updating it upon every iteration through a chosen scheme, the static equilibrium coordinates of the nodes can be calculated. The structure is seen to have reached equilibrium once the force-density matrix has reached a steady-state value and does not change upon further iteration.

$$\boldsymbol{x} = \boldsymbol{D}^{-1}\left(\boldsymbol{P_x} - \boldsymbol{D_f x_f}\right) \tag{3.6.15}$$

$$\boldsymbol{y} = \boldsymbol{D}^{-1}\left(\boldsymbol{P_y} - \boldsymbol{D_f y_f}\right) \tag{3.6.16}$$

$$\text{With:} \quad \boldsymbol{D} = \boldsymbol{C}^T\boldsymbol{Q}\boldsymbol{C}; \quad \boldsymbol{D_f} = \boldsymbol{C}^T\boldsymbol{Q}\boldsymbol{C_f}$$

3.6.2 Coding of Chosen Algorithm

Although DR is a popular form-finding method, research done by Veenendaal and Block (2012) concluded that the FDM converged faster and also required less iterations compared to DR for multiple geomtries tested. The FDM also proved advantageous in its ease of implementation, since it does not convert a static problem to a dynamic problem as with the approach taken with DR. For these reasons, FDM was chosen as the simulation method of choice. The FDM was used as an extension of the Python-script described in Section 3.5 and thus used the same design geometry as described. The general structure of the FDM code was split into three categories namely matrix generation, node pressure-force calculation and lastly FDM method implementation, residual checking and matrix updating. For each of these a dedicated function was created.

The algorithm starts with the input of a general 2D membrane structure as a collection of x- and y-coordinates. From this the function named *Matrix* discretizes the structure into a user-defined number of nodes and straight lines between the attachment locations of the vertical spars. Here-after the function calculates whether each node is free or fixed based on geometric constraints. For the algorithm developed here, the origin of the leading edge and the tip of the trailing edge, with coordinates (0,0) and (L,0), were fixed as well as all spar attachment locations. In Figure 3.9 an example of the fixed node locations can be seen for a six chamber wing design.

Using this information the free and fixed Connectivity matrices ($\boldsymbol{C}$ and $\boldsymbol{C_f}$) are generated as well as the separate free and fixed nodal coordinate matrices ($\boldsymbol{x}$, $\boldsymbol{y}$, $\boldsymbol{x_f}$ and $\boldsymbol{y_f}$). From these newly calculated matrices the nodal difference matrices ($\boldsymbol{u}$ and $\boldsymbol{v}$) are calculated. The transpose of the Connectivity matrix is also calculated and stored for later use by this function.

The function named *pressure-force* is responsible for the calculation of the pressure-forces acting on each node. All designs developed utilised some form

Stellenbosch University https://scholar.sun.ac.za

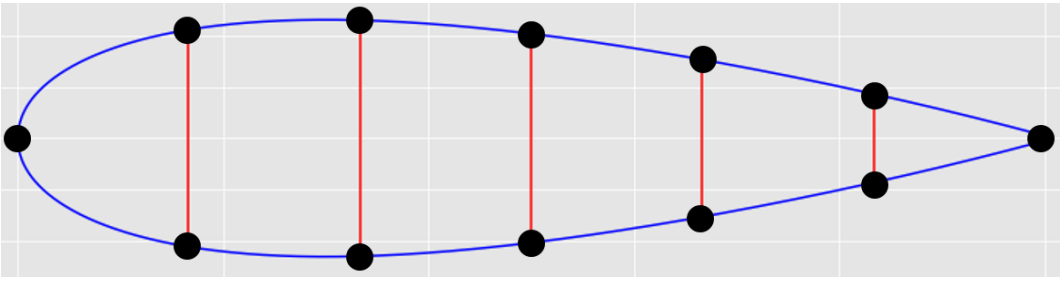

Figure 3.9: *Example of the Fixed Nodes of a Wing Structure Consisting of Six Chambers as Shown by the Black Dots*

of internal pressure resulting from inflation and as a result the pressure-force acting on each node as well as the x- and y-component of this force had to be determined. As the structure iss discretized into nodes and branches, each branch consisted of straight line with a distinct angle and length, which is dependent on the geometry of the given structure.

For calculating the force acting on each node, it was decided to split the total pressure-force acting on each branch into two equal force vectors acting only on the connected nodes. These force vectors are calculated by determining the magnitude of the pressure-force acting on each branch, dividing it by two and splitting it into its Cartesian components using the distinct angle of each branch. This angle could be easily be calculated by using the nodal coordinates of the connected nodes and basic trigonometry due to the the branches being straight lines. The sum of pressure-force vectors of the previous and consecutive branch is then used to calculate the resulting pressure-force vector at each node. The pressure-force vector of each node is then stored in two separate arrays for the respective x- and y-components.

The function named *FDM* is responsible for the actual implementation of the FDM. This function requires all matrices and vectors generated by the previous two functions described as well as a vector of initial guesses for the force-density of each branch in the discretized structure. An additional constraint added to the general FDM is the constraint of fixed length and is mathematically shown in Equation 3.6.17. This was added as the material used to construct the prototypes was seen as in-extensible and thus the initial length of each branch was seen as constant.

$$\boldsymbol{l} = \boldsymbol{L} - \boldsymbol{L}_{\text{initial}} \tag{3.6.17}$$

Using the quantities generated by the previously defined functions, the new nodal locations are iteratively calculated where-after the new length of the branch is calculated. The force-density vector ($\boldsymbol{Q}$) is then updated after every iteration by adding ΔQ, which is a function of the change of length in the

Stellenbosch University https://scholar.sun.ac.za

respective x- and y-direction, to the original force-density vector. The calculation of ΔQ is briefly expanded on in Equation 3.6.18, however the exact calculation is mathematically complex and is not of importance for the general explanation of the algorithm.

$$\Delta \boldsymbol{Q} = f\left(\frac{\boldsymbol{\delta l}}{\boldsymbol{\delta x}}, \frac{\boldsymbol{\delta l}}{\boldsymbol{\delta y}}\right) \tag{3.6.18}$$

$$\text{With:} \quad \frac{\boldsymbol{\delta l}}{\boldsymbol{\delta x}} = \boldsymbol{C}^T \boldsymbol{u} \boldsymbol{L}^{-1}; \quad \frac{\boldsymbol{\delta l}}{\boldsymbol{\delta y}} = \boldsymbol{C}^T \boldsymbol{v} \boldsymbol{L}^{-1}$$

The iteration process is repeated until the force-densities in each branch has either changed by less than a specified tolerance during consecutive iterations or a user-defined maximum iteration count is reached. After the iteration process has ceased, the new nodal coordinate locations are stored and the resulting shape is displayed.

3.7 Design of Experiment, Response Surface Methodology and Implementation

3.7.1 Design of Experiment (DoE)

DoE is a powerful data collection tool that has its roots in the field of applied statistics. Through the use of a DoE, the effect of the various input parameters on the output of a process can be rapidly determined. This is done by using a statistical approach and varying the values of multiple input parameters at the same time, resulting in a drastic reduction in the number of experiments needed to explore the entire design space.

For this project a central-composite design (CCD) was chosen as the DoE method of choice, since it allows the rapid exploration of the entire design space by using an embedded full-factorial model along with additional points added to estimate the curvature and the inter-experimental variance of the data.

At the core of a CCD is an embedded two-level full-factorial model, which consists of a mathematical model where all the input factors are set at two distinct levels, namely high or low. Using these values, a range of designs or experiments are formed by combining all the input parameters in all possible high/low combinations. Figure 3.10 shows a typical setup for a two-factor full-factorial DoE with three input variables. Each dot in Figure 3.10 represents a possible combination of the input parameters to be used for a design or

Stellenbosch University https://scholar.sun.ac.za

experiment.

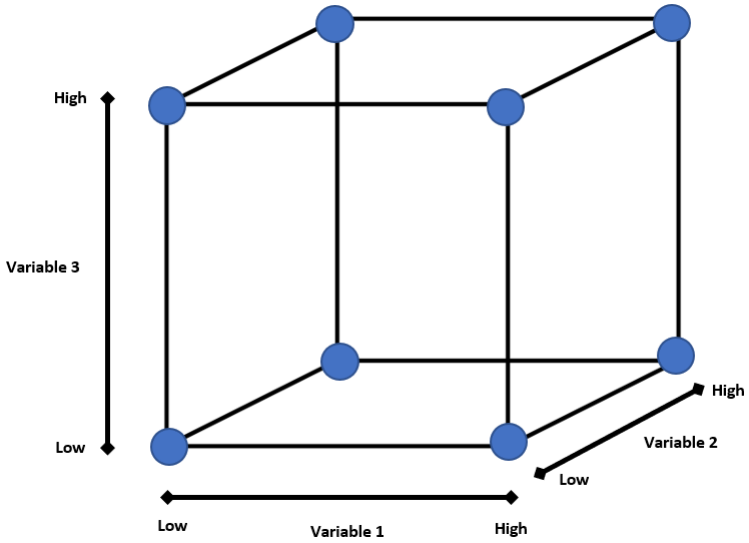

Figure 3.10: *Full-factorial Model with Three Input Parameters*

The most basic form of CCD is a full-factorial design with only one additional point included in the absolute center of the design space. For this project, this form of CCD was chosen, since it allowed rapid exploration of the entire design space without the need for an excessive number of prototypes to be generated, while still maintaining the benefits of being able to estimate the curvature found in the collected data. Two additional duplicate points were also inserted in the absolute center of the design space, which allowed for an estimation of variance found between prototype builds.

3.7.2 Response Surface Methodology (RSM)

Response Surface Methodology is the process of fitting a mathematical model to data collected through some process such as a DoE. The purpose of RSM is to optimise the underlying process by using the generated mathematical model to estimate the optimal parameter combination in the explored design space.

For this project, it was assumed that the relationship between the data collected through the CCD study and its input parameters was parabolic in nature, which made it possible to easily estimate the optimal parameter combination within the explored designs range by finding the location of the global minimum of the second-order surface.

As the RSM is a curve fitting process at its core, some performance metrics were selected and calculated for each RSM to evaluate the quality of the fitted

Stellenbosch University https://scholar.sun.ac.za

surface or mathematical model. The performance metrics chosen include the Root Mean Square Error (RMSE), the Mean Absolute Error (MAE), the R^2-value and the adjusted R^2-value. The Root Mean Square Error (RMSE) is a measurement of the standard deviation of the error between the predictions of a model and the actual measured data and measures how far the data points are away from the fitted function. Mean Absolute Error (MAE) is a measurement of the average absolute error between the target values and the model predictions. MAE is a linear score where all individual differences between the measured data and the model predictions are weighted equally, making it less sensitive to outliers as compared to the RMSE.

The coefficient of determination or R^2-value is a metric that shows the proportion of variance found in the measured data that is accounted for by the model and is a good indication of how well unseen inputs will be predicted by the model. The R^2-value is a ratio and can vary from 0 to 1. The adjusted R^2-value is a modified version of the R^2-value that has been adjusted for the number of input parameters in the model and is used as a selection criterion between models of varying complexity. The adjusted R^2-value increases only if a newly added parameter or term improves the prediction accuracy of the model more than would be expected by pure chance and is always lower than the R^2-value.

3.7.3 Implementation

For the implementation of the CCD study a Python-script was developed utilizing the *PyDoE*-package at its core. The *PyDoE*-package is capable of generating the necessary experimental parameter combinations for a multitude of different types of DoE's, including the full-factorial model used as the core model of the chosen CCD.

On the first run, the user is asked to input the number of variables to be investigated, the names of the variables as well as the minimum and maximum allowed values for the parameter. The script also prompts the user to input how many duplicate center-point designs should be added to convert the full-factorial model to the CCD chosen for this project.

The developed script also improved the readability of the *PyDoE*-package output by changing the default representation for the high/low parameter combination from 1/-1 to the maximum/minimum value of each parameter as specified by the user. The option to extract the input data as well as the generated DoE data to a comma-separated value (.csv) file was also added.

The functionality of the developed script was extended to include a second-order surface fitting function as well as a multi-variate minimisation algorithm

Stellenbosch University https://scholar.sun.ac.za

to be used for the RSM process after the CCD data had been collected. The function responsible for the generation of the mathematical model relied on a multi-variate linear regression algorithm utilising the *Sklearn*-package at its core. To fit a second-order surface to the data, the function required the construction parameters and the measured output of the prototypes as inputs

Using the generated second-order surface, the output of a prototype constructed with any parameter combination in the explored design space could be predicted. To obtain the optimal parameter combination in the explored design space, a multi-variate minimisation function from the *SciPy*-package was used to find the global-minimum location of the surface and return the values of each parameter at this location.

Stellenbosch University https://scholar.sun.ac.za

Chapter 4

Critical Evaluation of Available Technology

The goal of this research was to develop a wing that displays a useful change in camber while the wing is in operation. From the literature review, it is evident that all of the identified technologies can be used to induce a camber change by attaching the structures at intelligently picked locations within or on top of the wing-structure. To narrow down the list of technologies to be explored in detail, a list of general requirements for the morphing-mechanism to be incorporated into the final wing design had to be identified. For this project, three requirements were identified, namely:

- The design must be able to produce a useful camber-change
- The design must be robust
- The design must have a fast actuator response time

For the conceptual wing designs it was decided to mimic the flap-mechanism rather than the slat-mechanism described in Chapter 2. This decision was made due to flaps being mechanically simpler to implement in comparison to slats, since a basic flap only requires a hinge mechanism, while slats require a hinge and some form of sliding mechanism.

On modern aircraft, flap-settings are conventionally kept between 5-20^o for take-off and between 30-45^o during landing (Boldmethod, 2019). During take-off small flap-adjustments (5-20^o) noticeably increase the maximum coefficient of lift, while increments above 35^o induces more drag than lift (Kluga, 1991). For this reason a useful camber-change was quantified as any change in angle above 20^o. This threshold was calculated by averaging the overall range of flap angle settings used for take-off and landing.

The robustness requirement is measured in the amount of joints a technology requires to function as intended and was assigned a score between 1 and 3.

Stellenbosch University https://scholar.sun.ac.za

Technologies utilising less than five joints were assigned a 1, while technologies requiring between five and ten joints were assigned a 2. Technologies requiring more than ten joints were assigned a value of three. A lower score indicates that the technology is more likely to function after an impact compared to a technology with a higher score.

Response time of the implemented technologies was of high importance, since the response time would highly influence the controllability and manoeuvrability of the wing. The controllability and manoeuvrability of the wing design form part of the aerodynamic considerations which are not considered in this iteration of the project, but to produce a viable wing design, these must still be considered when choosing a camber-changing mechanism. This requirement also uses a scoring system between 1 and 3. Technologies capable of fully actuating in less than 30 s, between 30-60 s or more than 60 s are respectively assigned a score of 1, 2 and 3.

A method to compare and reduce the amount of viable technologies had to be developed. For this purpose, four elimination criteria were identified through slight modification of the design requirements as stated above. The elimination criteria identified can be reduced to four distinct questions, with the first three being crucial for the development of a functional wing, while the last elimination criteria only increased the overall functionality of the design. The questions used for the elimination criteria were:

- Can the technology be used to create a mechanisms that produces a fixed change in camber?
- Does the technology have a fast response time?
- Is the general structure of the technology crash resistant?
- Can the technology be used to create an adjustable camber-morphing mechanism?

After the elimination criteria were identified and sorted by descending importance, the elimination diagram displayed in Figure 4.1 was constructed. The order of importance for the identified criteria was chosen based on the minimum requirements to developed a morphing wing, with the more important criteria being vital for the base-function, while the less important criteria only add additional functionality to the design. In the diagram, the identified criteria can be seen as hurdles that each technology has to overcome, starting with the most crucial elimination criteria on the left and moving towards the right. If a technology does not satisfy certain criteria it is permanently eliminated from the remaining viable choices.

Stellenbosch University https://scholar.sun.ac.za

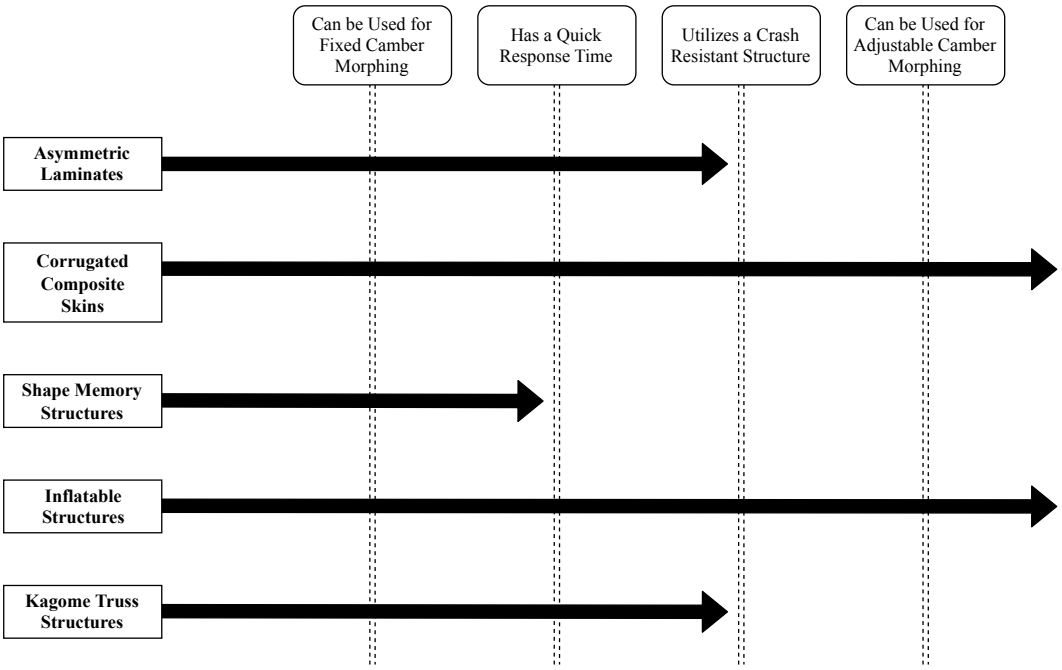

Figure 4.1: *Elimination Decision Process of Technologies Available*

Shape memory structures were the first technology to be eliminated. This was due to the fact that shape memory structures are known to have a slow response time, as confirmed in research done by Barbarino *et al.* (2009) regarding the response time of various shape memory structures.

Asymmetric laminates and kagome truss structures did not satsify the robustness requirement. Kagome truss structures utilise multiple hinges throughout the structure that would results in partial or complete failure of the mechanism if some of the joints were damaged during an impact. Asymmetric laminates do not use multiple joints or hinges, but require a separate actuator to create the snap-through effect and are mostly attached to the surface of the laminate (Gude and Hufenbach, 2006). Damage to this additional actuator during an impact would prevent any further wing morphing and thus render the device inoperable.

From the diagram it is seen that two of the five technologies, namely inflatable structures, and corrugated composite skins, satisfied all of the elimination criteria fully. These two technologies were then chosen for further incorporation and exploration during the design phase of the project.

Stellenbosch University https://scholar.sun.ac.za

Chapter 5

Prototype Designs

This chapter focuses on the iterative design process followed in developing the base-structure and morphing-mechanism. In Section 5.1, the base-structure designs developed during this research are discussed, while in Section 5.2 the designs considered for the morphing-mechanism are described.

5.1 Wing Base-structure

A criterion for a successful prototype is for the design to be self-supporting, meaning the overall wing structure must be stiff enough to support its own weight as well as not deforming extensively when a slight force is applied to the structure. For this reason, it was decided to first determine a structurally adequate base-structure before any morphing mechanisms were incorporated into the design. For the base-structure, three designs were developed and constructed to evaluate the viability of using it as the final base-structure of the morphing wing.

In Appendix A, stiffness tests are described that were used for the preliminary evaluation of the various base-structures. The results of these preliminary tests are also available in Appendix A. Design 1 drew inspiration from conventional wing design and utilises a system of rigid vertical spars. Design 2 was the first fully inflatable design and consisted of tube-like structures formed through simple flat seals. The last design, Design 3, was also a fully inflatable design and also consisted of tube-like structures. For Design 3 these tube-structures were created by vertical polyethylene spars instead of simple flat-seals.

5.1.1 Rigid Vertical Spars (Design 1)

The first base-structure design was inspired by the combination of current wing designs and previous research done, most notably by Vos *et al.*, Vasista

Stellenbosch University https://scholar.sun.ac.za

and Tong and Luo and Tong, as briefly discussed in Chapter 2. The design consisted of a structure formed from various rigid vertical spars connected to a single semi-flexible horizontal spar that spans the entire length and width of the wing. The horizontal spar is also fixed to two additional rigid components designed to mimic the general shape of a wing at the leading and trailing edge. To ensure a smooth and continuous wing surface, it was planned to cover the entire structure with a layer of polyethylene sheeting.

For structural and morphing purposes, the empty spaces between consecutive spars were filled with an inflatable bladder, also constructed from polyethylene sheeting. These bladders could then be individually inflated and by varying the pressure in each bladder, an overall shape change in the wing could be induced. The formulated design can be seen in Figure 5.1, with the dots representing the bladder locations.

From the stiffness test results found in Appendix A, it can be concluded that this design had the benefit of being completely self-supporting and load-bearing along the width as well as the chord length of the wing once the bladders were inflated. The large load-bearing capabilities of the structure did however limit the possible shape-change. The limited change of camber possible with this design as as well as the overall construction time required, made this design less attractive.

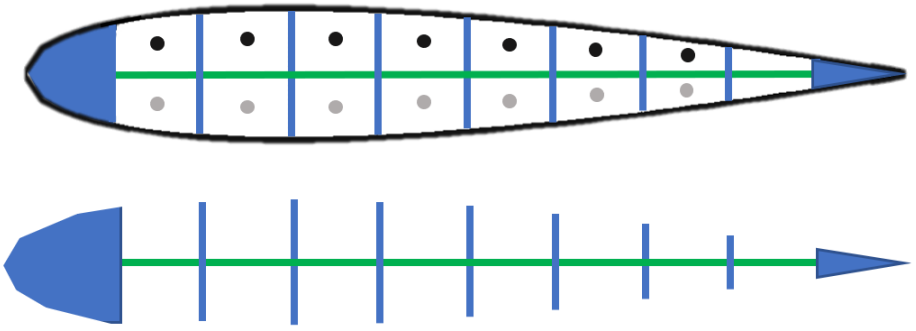

Figure 5.1: *Inflatable Bladder-type Base-structure Design. [Top, Internal Structure Covered with Polyethylene Film; Bottom, Internal Structure Only]*

5.1.2 Fully Inflatable Multi-cell Design with Flat-seals (Design 2)

After Design 1 was evaluated, a fully inflatable design was developed. Fully inflatable designs were considered, since it reduced the total weight of the design while simultaneously increasing the robustness of the wing and its likelihood

Stellenbosch University https://scholar.sun.ac.za

Table 5.1: *Results of Diameter Change Experiment (All Values in Millimetre, unless Clearly Stated Otherwise)*

Diameter	Test				%Δ in Original Diameter
	1	2	3	Average	
30	21	19	23	21	70
50	32	34	30	32	64
100	66	67	67	66.67	66.67
150	102	105	100	102.33	68.22

of surviving impacts without sustaining critical damage. An inflatable wing will also reduce the cost of construction as well as creating the possibility of a deployable wing, that requires a low storage volume, while simultaneously possessing a high operating volume. The inflatable concept consisted of two sheets of polyethylene bonded together across the width of the sheeting at various locations to form tube-like structures when inflated. A schematic of the design can be seen in Figure 5.2, showing both the pattern needed to form the structure as well as the fully inflated state.

During construction, it was noticed that there was a discrepancy between the length of polyethylene sheeting used and the final length of the wing once inflated. To determine the extent of this discrepancy, an experimental analysis was conducted by constructing tubes of various diameters and comparing the spacing between consecutive seals to the inflated tube. Through this experiment, it was found that the tube diameter of the inflated shape was, on average, 32.8 % smaller than the length between the consecutive seals on the uninflated shape that form the tube. This shrinking characteristic is seen in all inflatables and has to be kept in mind when specific tube diameters or other specific dimensions are required. The complete results found through this experiment can be seen in Table 5.1.

This design was much less labour and time-intensive to construct and also weighed much less than Design 1, which made it an attractive choice for use as the base-structure. It was however found through the preliminary stiffness evaluation of the concept that the simple flat-seals used to form the tubes reduced the overall stiffness along the cord of the wing dramatically. This can be seen from the test results in Appendix A, where the design was unable to support any additional weight in the chord direction and did not meet the specified 0.5 kg threshold along the width of the wing.

These results confirmed that the design was not self-supporting and did not have any additional load-bearing capabilities. As a result, this design was deemed unfeasible for use as the base-structure. To remedy this issue, the seals along the width of the structure were shortened to form two additional

Stellenbosch University https://scholar.sun.ac.za

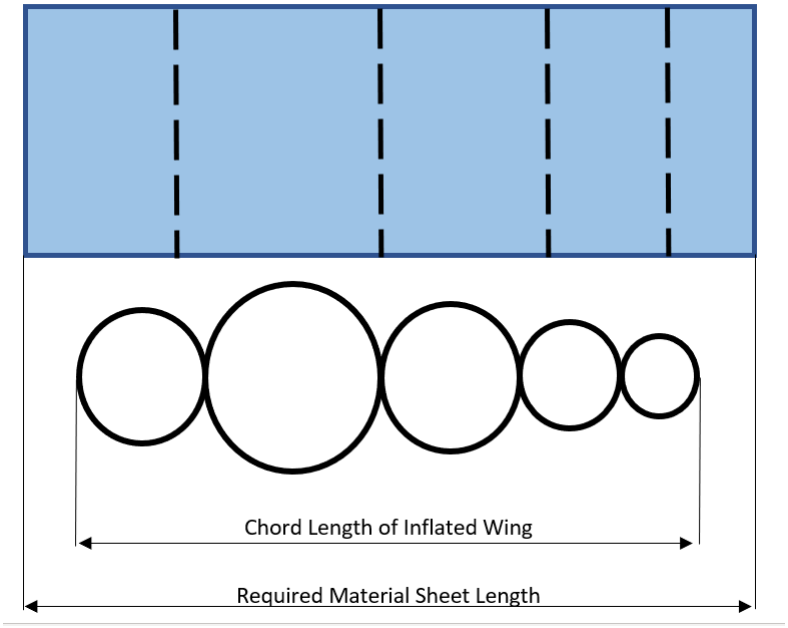

Figure 5.2: *Fully Inflatable Design with Full Width Flat-seals. [Top, Flat Sheet Pattern with Seal Locations Shown with Dashed Lines; Bottom, Design Once Fully Inflated]*

tubes running parallel to the chord line. These newly added tubes acted as stiffeners along the chord and width of the wing. From the preliminary stiffness tests available in Appendix A it can be seen that the modified prototype was self-supporting and load-bearing. The pattern used to create the modified design can be seen in Figure 5.3.

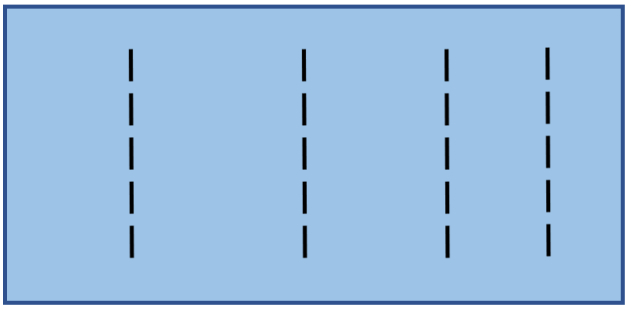

Figure 5.3: *Pattern of Modified Design 2 with Shortened Flat-seals*

Stellenbosch University https://scholar.sun.ac.za

5.1.3 Fully Inflatable Multi-cell Design with Flexible Spars (Design 3)

Taking into account the benefits offered by Design 2 in terms of weight, robustness and construction time, a second fully inflatable design was developed. During the planning of this design, much consideration and thought were given to improve the seal stiffness between consecutive tubes without the need for additional tubes parallel to the chord line. A recent paper by Breuer *et al.* (2007), mentioned previously in Section 2, exploring the use of Tensairity in inflatable wings partly inspired the new design. In this paper, Breuer *et al.* created an inflatable wing by using a single inflatable bladder with cables wrapped tightly around the structure, perpendicularly to the chord line, at various locations to force the bladder to approximate a wing shape. Using this principle, a design was developed using a series of internal spars fixed to both layers of the polyethylene sheeting used, to create a series of tube-like structures and consequently force the structure to take on a wing-like shape.

For this base-structure a Python-script was developed and used to determine the spar locations and lengths from a 4-digit NACA aerofoil. The script also incorporates a Force Density Method (FDM) algorithm to simulate what the fully inflated shape will look like for the given user inputs. This script was primarily developed to streamline the design process for this base-structre design. A detailed description of the developed script and the incorporated FDM algorithm are available in Chapter 3. In Figure 5.4 an example of the initial symmetric 4-digit NACA aerofoil with 6 inflatable chambers, a chord length of 1000 mm and a 23 % thickness ratio can be seen as well as the FDM generated inflated base-structure and its smooth wing approximation.

After construction, a computer model of the prototype was created through a 3D-scanning process to determine the accuracy of the predicted shape versus the actual shape once constructed. Information regarding the 3D-scanning method used is available in Chapter 3. To create a fair comparison between the actual and script generated wing profile, it was decided to section the generated model at its mid-plane to effectively cancel any edge effects created by the construction method. Information regarding the 3D-scanning process and a brief explanation of the working principles behind it can also be found in Chapter 3. In Figure 5.5, the sectioned view of the resulting 3d-model can be seen. When Comparing Figure 5.5 with the script generated aerofoil as seen in Figure 5.4, it is noted that the script generated aerofoil and the constructed wing cross-section are similar in shape with small deviations present, such as a slight decrease in the amount of chamber-curvature seen in the constructed design as compared to the script generated result.

Stellenbosch University https://scholar.sun.ac.za

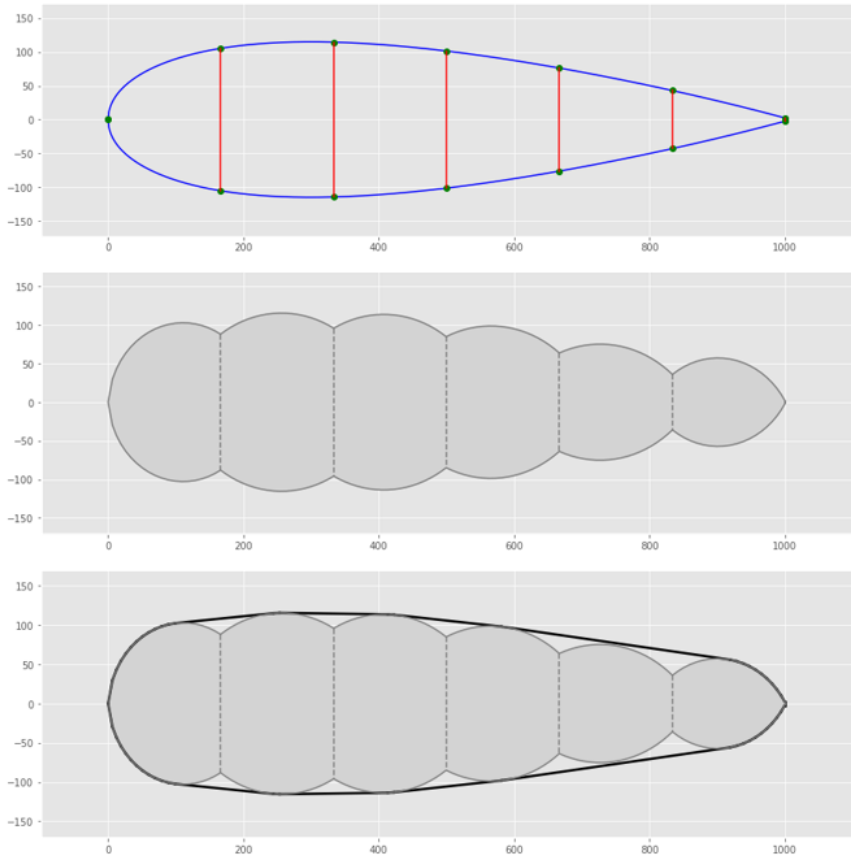

Figure 5.4: *Aerofoil Generated with the Developed Python-script. [Top, Original 0023 NACA Aerofoil; Middle, Inflatable approximation of 0023 NACA Aerofoil; Bottom, Inflatable 0023 NACA Smooth Wing Approximated Shape]*

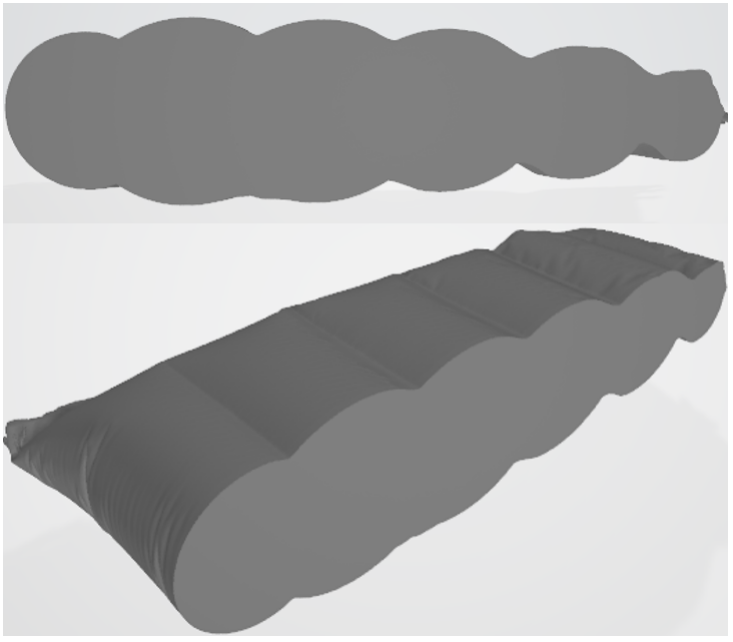

Figure 5.5: *3D-scan Model of Prototype 0023 NACA Aerofoil with Build Parameters as Generated by the Python-script Developed. [Top, Side-view of Model; Bottom, Isometric View of Model]*

Stellenbosch University https://scholar.sun.ac.za

From testing the constructed design, it was seen that this design showed superior stiffness and load-bearing capabilities throughout the entire wing structure, compared to the previous modified inflatable design as can be seen when comparing Table A.4 and Table A.3 in Appendix A. This design was also much lighter than Design 1 and also less labour-intensive to construct. This design was also simple and time-efficient to construct, with the added benefit of generating the design parameters through the created Python-script, ensuring that the constructed design approximated a wing shape. Design 3 was chosen for the base-structure of the wing. This choice also meant the final designed wing would be a completely inflatable structure.

5.2 Wing Morphing Mechanisms

In this section the morphing-mechanisms developed through the iterative design process is discussed. To simplify the mechanism design, a decision was made to initially only focus on camber morphing to mimic current wing-morphing devices found on modern aircraft. The deformation mechanism concepts explored can be split into two categories, namely designs utilizing a single geometry and designs utilizing multiple structures functioning on antagonistic principles. In Appendix A, joint stiffness and preliminary actuation-force measurement tests are described that were used for the preliminary evaluation of prototypes with the morphing mechanisms incorporated. The results of these preliminary tests can also be found in Appendix A.

5.2.1 Single Geometry Designs

As mentioned in Section 2, a recent research paper by Ou *et al.* (2016) explored the concept of embedding intelligence into inflatable structures. The research focused largely on using heat-sealing to create sealed areas within an inflatable in the form of various geometric shapes that when inflated, induced a useful shape-change in the structure. In Figure 5.6, two examples of such seal geometries can be seen along with the resulting deformation once the structure is inflated. The dashed line visible in the figures represents the shape before inflation. The diagonal line seals can be used in a morphing wing to induce twist when inflated, while the diamond seal can be used to increase the camber of the wing. Further exploration revealed that out of all the seal-shapes tested, only the diamond seal generated a hinge that could hold its shape when trying to manually force the inflated structure to its original form. It was for this reason that only the diamond-seal mechanism was further explored and developed.

The diamond-seal induces a bending action when inflated as shown in the top image of Figure 5.6. The amount of bending can easily be controlled by

Stellenbosch University https://scholar.sun.ac.za

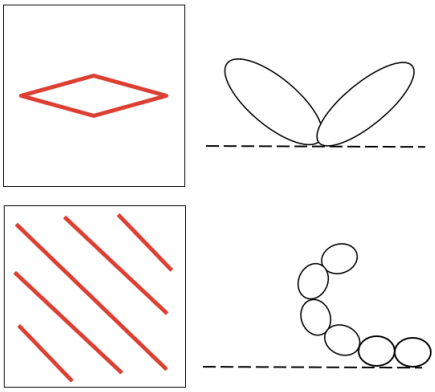

Figure 5.6: *Geometric Seals and the Resulting Deformation once Inflated. [Top, Diamond Seal; Bottom, Diagonal Lines]*

varying the aspect ratio of the diamond, with a larger aspect ratio reducing the bending angle and a smaller aspect ratio the opposite. In Figure 5.7, a few examples of how the aspect ratio influences the bending angle are shown. It was evident from the design that only a fixed camber would be present if this actuator would be incorporated into an inflatable wing since the actuator is only capable of carrying a load when fully inflated.

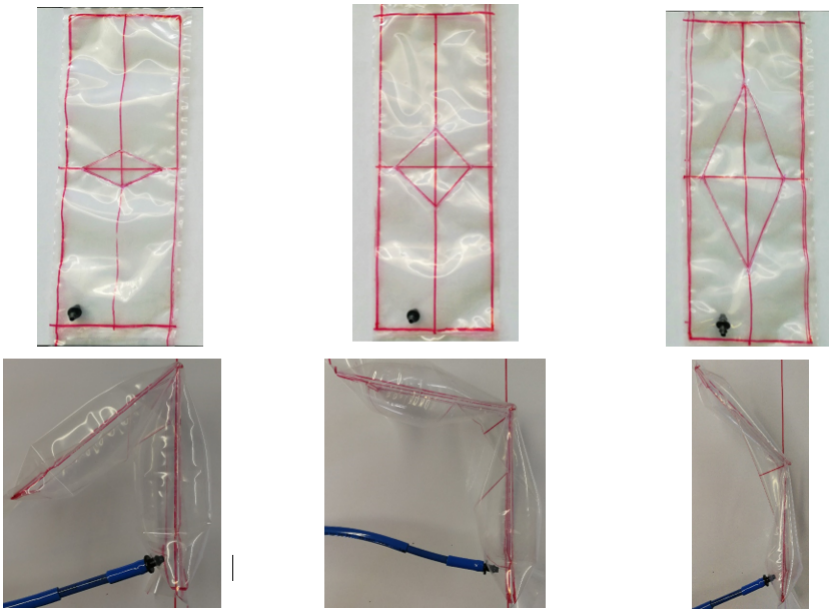

Figure 5.7: *Diamond Seals with Different Aspect Ratios and the Resulting Deformation once Inflated*

Stellenbosch University https://scholar.sun.ac.za

5.2.2 Antagonistic Actuator Designs

To rectify the issue of a fixed camber found with the diamond-seal actuator, two strategies were used. The first was to use a double layer design, where an actuator using the diamond-seal was bonded to the top and bottom surface of the base-structure. In cases such as these where heat is used as the bonding method, the bending action will always tend towards the surface where heat was applied to. The application of heat weakens the material marginally and forms a type of folding-crease on the surface, making the resistance to bending slightly less in that region (Ou *et al.*, 2016). This phenomenon meant that the direction of the top and bottom actuators could be predefined, resulting in an antagonistic mechanism that could vary the camber of the wing, depending on the pressures in the two actuators. This design was, however, difficult to construct and manufacturing defects were frequently encountered, due to the heat-sealing method used and the complexity of the actuator pattern.

It was noted that for the basic diamond-seal mechanism, the actuator effectively consisted of two isolated inflatable pockets, separated by the perimeter of the added seal. In the original configuration, the internal pocket is sealed and never inflates, resulting in a region of lower stiffness compared to the inflated outer pocket. This region causes a reduction in the total resistance to deformation and as a result, changes the equilibrium shape of the structure to the state seen in Figure 5.7. By individually inflating the outer as well as the internal pocket simultaneously, an antagonistic interaction is created between them, with the outer pocket inducing a downwards bending force and the internal pocket a counteracting or straightening force. This actuator made the inflatable wing topologically simpler since only one actuator was needed instead of two, while simultaneously simplifying the overall construction process of the wing. In Figure 5.8, an inflatable wing using this antagonistic diamond-seal actuator can be seen.

The diamond-seal antagonistic design discussed above proved to be effective in changing the camber of an inflatable wing but had the effect of creating a sudden change in the wing geometry where the actuator was positioned. This sudden change in surface geometry could lead to premature flow separation and vortex formation, which would lead to an increase in the overall pressure drag experienced by the inflatable wing, resulting in a less aerodynamic design. This change in geometry could also lead to possible stress concentrations forming in the material, resulting in weak points on the wing surface. For this reason, an entire new actuator was developed.

The new design was inspired by the inherent spaces found between consecutive tubes of the base-structure chosen in Section 5.1. The actuator consisted of two polyethylene rectangles, bonded respectively to the upper and lower

Stellenbosch University https://scholar.sun.ac.za

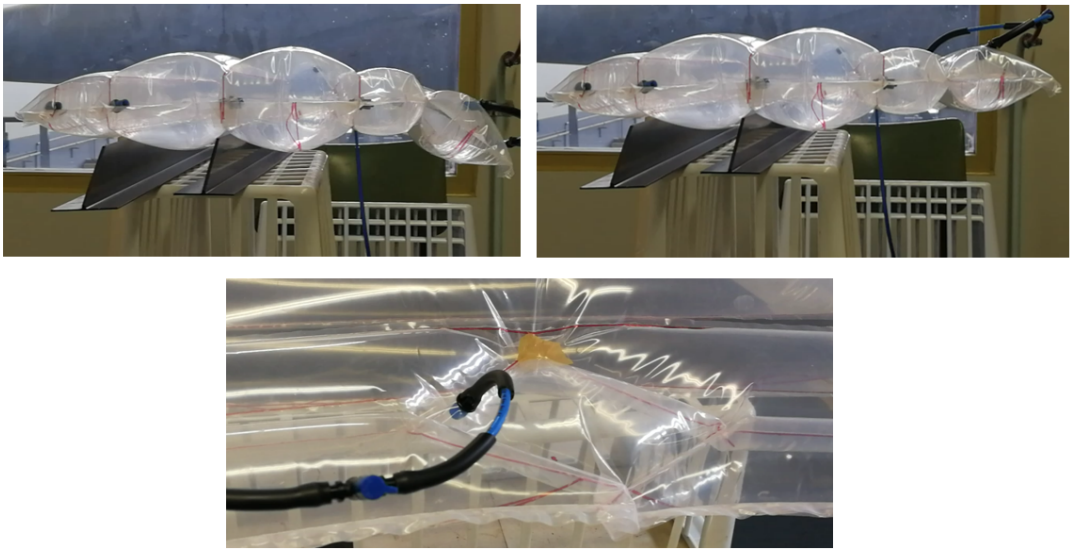

Figure 5.8: *Diamond-seal Incorporated into an Inflatable Wing. [Top Left, Only Outer Pocket Inflated; Top Right, Both Pockets Inflated; Bottom, Actuator Close-up with Both Pockets Inflated]*

surface of the consecutive tubes. Upon testing, it was noted that the base-structure was too stiff and prevented the actuator from imposing any useful deformation on the structure. To allow the structure to deform, the stiffness of the base-structure had to be reduced at the location where the actuator was placed. This was done by incorporating the simple flat-seal as used by Design 2 discussed in Section 5.1, since it was evident from Design 2 that a simple flat-seal between tubes lowered the stiffness at the joint significantly.

The base-structure design was altered slightly by inserting a flat-seal between consecutive tubes at each location where an actuator was to be placed, instead of using a spar as originally intended. A schematic representation of this new design can be seen in Figure 5.9, with Tube 1 and Tube 2 representing consecutive tubes of the base-structure.

Through observation of experiments it was noticed that the multi-tube actuator design combined with the newly modified base-structure outperformed all previously constructed prototypes in terms of possible shape-change as well how accurately the shape-change could be controlled. It was also noted that with the multi-tube actuator, the hinge location was much stiffer over the entire range of camber possible, compared to the diamond-seal designs previously implemented, which is confirmed by comparing Table A.6 with Table A.5 found in Appendix A. By the nature of the multi-tube design, both the top and bottom actuator-pockets are pressurized at all times, with the pressure only varying in each pocket depending on what wing-shape is desired. A de-

Stellenbosch University https://scholar.sun.ac.za

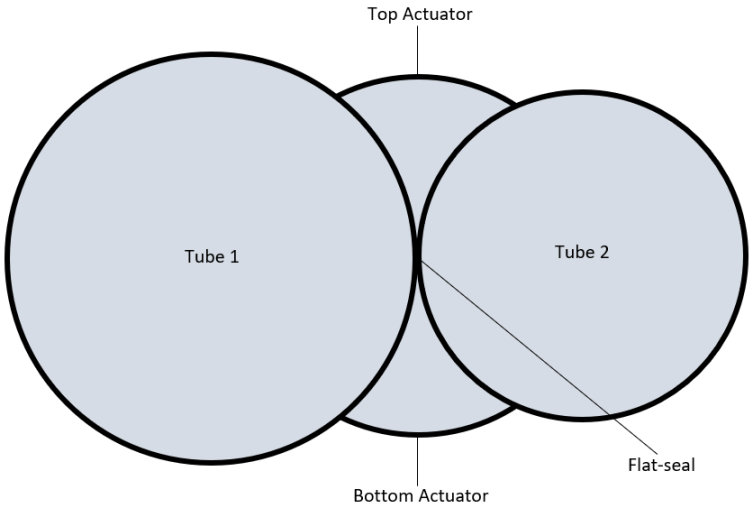

Figure 5.9: *Schematic of Antagonistic Multi-tube Actuator Design*

veloped prototype using the multi-tube actuator can be seen in Figure 5.10 in three different actuated configurations. For all further prototypes constructed, this actuator was selected as the design of choice, due to its performance, ease of construction and also since it does not cause the sudden geometry change that was evident with prototypes using the diamond-seal actuator design.

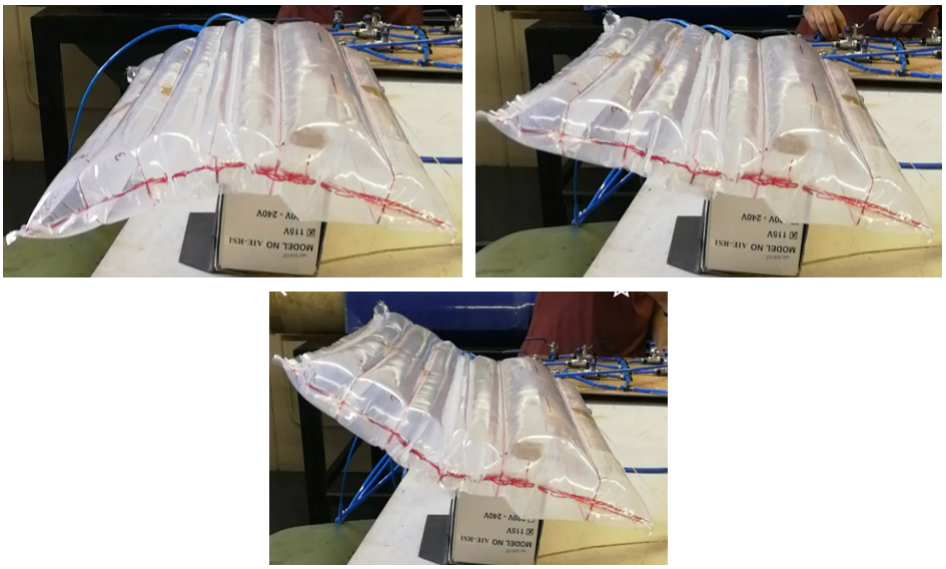

Figure 5.10: *Inflatable Wing Incorporated with the Multi-tube Actuator Design. [Top Left, Maximum Camber State Achieved by Pressurising only the Top Actuator; Top Right, Symmetrical State Achieved by Pressurising Both Actuators; Bottom, Maximum Reverse Camber State Achieved by Pressurising only the Bottom Actuator]*

Stellenbosch University https://scholar.sun.ac.za

Chapter 6

Further Investigation of Selected Wing Articulator

This chapter will focus on the implementation and results of the Design of Experiment (DoE) process as well as the One-Factor-at-a-Time (OFAT) study that was previously described in Chapter 3. The goal of the studies was to quantify to what extent changing the design parameter values influenced the induced shape change of the morphing-mechanism.

6.1 Parameterization of Selected Design

During the exploration phase of the multi-tube actuator, certain design parameters were varied on a trail-and-error basis to find a viable design that caused a noticeable shape-change. Through this randomised construction process, a total of nine design parameters were identified that influenced the performance of the actuator. The parameters identified can be seen in Figure 6.1.

To determine the effect each parameter had on the performance of the constructed actuator, a parametric study by means of a central-composite design (CCD) was carried out. As mentioned in Chapter 3, a CCD uses a full-factorial model at its core, which meant for a two-factor study with nine independent variables, 81 different actuator designs had to be constructed and tested. Additional to the 81 designs, three central designs would also be needed to estimate curvature and the inter-experimental variance in the data, bringing the total number of actuators needed to 84. Constructing 84 different actuators would have been extremely labour and time intensive, which would have been further complicated by the fabrication techniques used, resulting in a heightened possibility of actuators with defects needing reconstruction.

To avoid this scenario, certain simplifications were made to the design to reduce the number of independent design variables. Using the assumption of

Stellenbosch University https://scholar.sun.ac.za

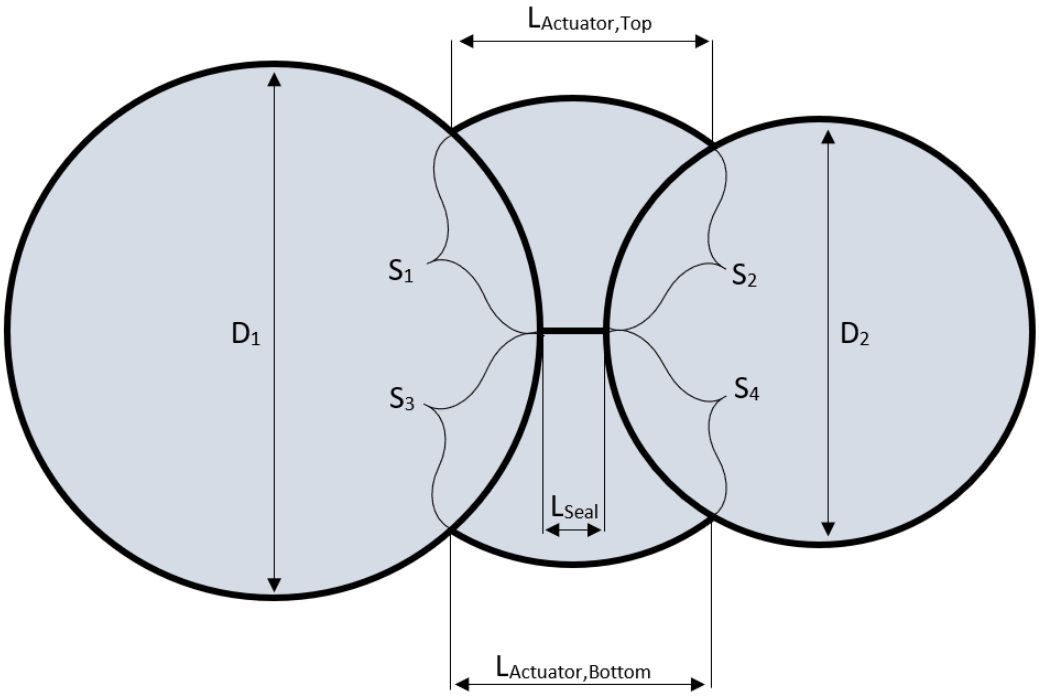

Figure 6.1: *Diagram of the Multi-tube Actuator and the Main Influencing Parameters.*

symmetry over the chord line as well as certain spacing considerations used to simplify the construction process, relationships between the variables were derived. The diameters of the two base-structure tubes were also assumed to be in a fixed ratio to each other. All relations that were derived are displayed in Equation 6.1.1-6.1.5, with a diagram of the actuator after the simplifications were applied also available in Figure 6.2.

$$D_2 = r\ D_1 \quad \text{where} \quad 0.5 \leq\ r \leq 1 \tag{6.1.1}$$

$$S_1 = S_3 = S_{\text{Left}} \quad \text{and} \quad S_2 = S_4 = S_{\text{Right}} \tag{6.1.2}$$

$$L_{\text{Actuator,Top}} = L_{\text{Actuator,Bottom}} = L_{\text{Actuator}} \tag{6.1.3}$$

$$L_{\text{Actuator}} = S_{\text{Right}} + S_{\text{Left}} + L_{\text{Seal}} \tag{6.1.4}$$

$$S_{\text{Right}} = S_{\text{Left}} = S \tag{6.1.5}$$

The simplifications displayed in Equation 6.1.1-6.1.3 reduced the number of variables from nine to five. Equation 6.1.5 shows another relationship that was assumed for simplicity and by applying it to Equation 6.1.4, the number of variables is further reduced to three. With three independent variables, a two-factor central-composite design with three center points added requires a total of eleven actuators to be constructed to explore the entire chosen design space.

Stellenbosch University https://scholar.sun.ac.za

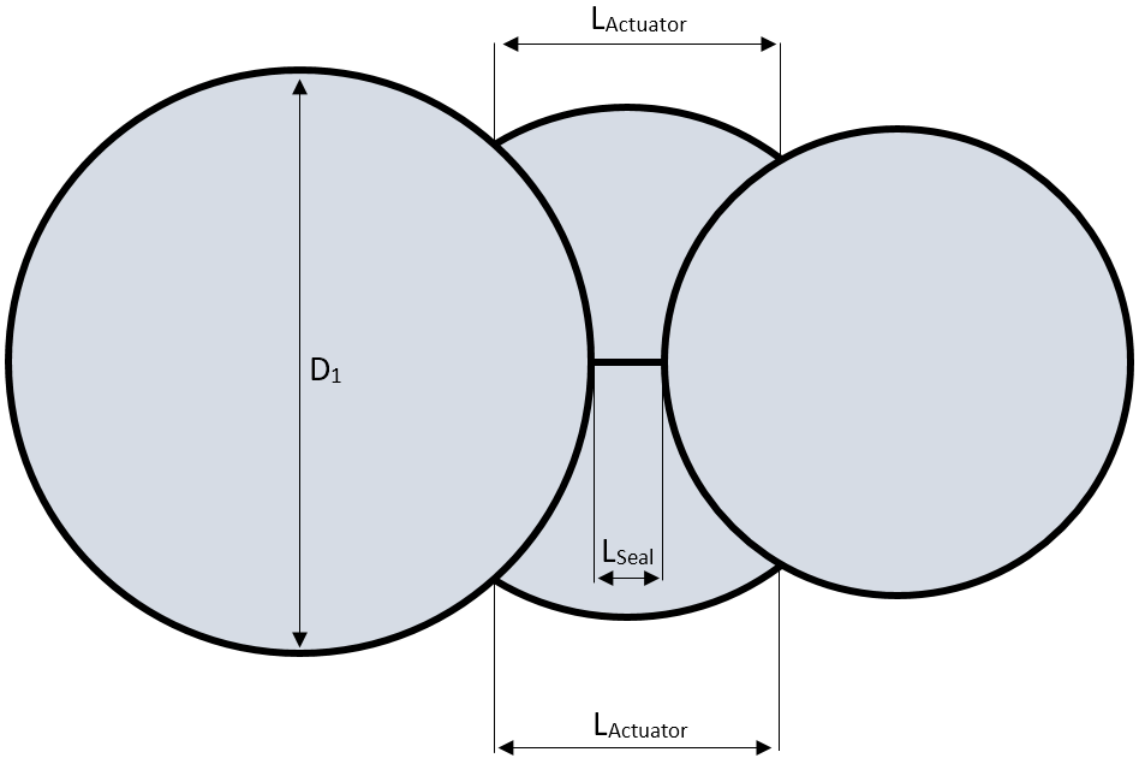

Figure 6.2: *Diagram of the Multi-tube Actuator and the Influencing Parameters after Simplification.*

6.2 Parametric Study of Selected Wing Articulator

6.2.1 Preliminary Calculations for Experiments

During the construction process and preliminary testing of the actuator design it was noted that if failure was to occur, it mostly occurred due to failure of a seal. For thin-walled pressure vessels, the stress in the hoop direction dominates failure and is governed by Equation 6.2.1.

$$\sigma_{\text{hoop}} = \frac{P\ r}{t} \tag{6.2.1}$$

From the observation that failure is governed by the seal strength and not by the strength of the polyethylene, it was decided to limit the hoop-stress in the tube membranes to that of the average seal strength. To determine the average seal strength, uni-axial tensile testing as guided by ASTM F88M-15 was used. ASTM F88M-15 covers the standard test method for the measurement of seal strength in flexible barrier materials through uni-axial tensile testing (ASTM International, 2013). For the tensile testing, ten test specimens were created by bonding two layers of polyethylene sheeting, with a length and width of

Stellenbosch University https://scholar.sun.ac.za

410x200 mm, together through the same technique used to create the actuator prototypes. From these specimens, five 25.4 mm wide samples were cut at equal distance from one another to form a total of 50 tensile test samples. In Figure 6.3, the specimen layout regarding the roll of polyethylene is shown as well as the layout of the samples on the test specimen.

The seal and sample directions were chosen as shown in Figure 6.3 to coincide with the seal and material direction used for the construction of all actuator prototypes. In Table 6.1, a summary of the results of the tensile testing can be seen. From Table 6.1 it can be seen that the average seal strength varies somewhat throughout the specimens tested, with the difference between the largest and smallest seal strength equalling 0.78 MPa. This fluctuation in seal strength is attributed to slight imperfections found in certain regions of the seals, which was an unavoidable consequence of the sealing method used. As the results from the tensile tests were distributed over a wide range, it was decided to use the overall average of the seal strength as the maximum allowable stress, which was calculated to be 2.35 MPa.

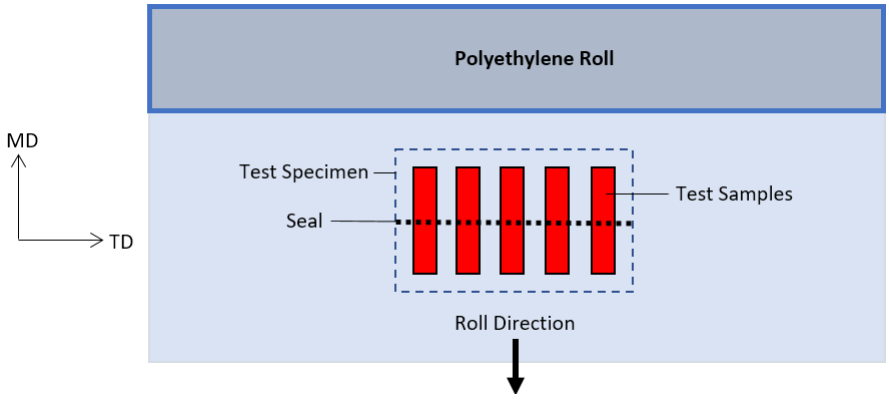

Figure 6.3: *Diagram of Sample Directions as used in the Tensile Tests [TD = Transverse Direction of Material; MD = Machine Direction of Material]*

The constructed actuators can be approximated as a combination of tubes, each consisting of a single polyethylene membrane. The stiffness of a membrane is reliant on the internal membrane pressure and since the function of the actuator relied heavily on the stiffness of each tube, it resulted in the internal pressure of each tube being a critical factor in the actuator performance that had to be determined. To calculate the pressure that ensured each tube was stiffened to such an extent that it would not negatively influence the actuator performance, it was decided to approximate each tube as a thin-walled pressure vessel with a unique radius. In Figure 6.4 a schematic is shown comparing the

Stellenbosch University https://scholar.sun.ac.za

Table 6.1: *Summary of Tensile Test Results*

Test Sample	Average Seal Strength (MPa)	Standard Deviation (MPa)
1	2.65	0.22
2	2.64	0.38
3	1.87	0.33
4	2.32	0.18
5	2.6	0.34
6	2.09	0.29
7	2.56	0.25
8	2.6	0.2
9	2.03	0.34
10	2.15	0.31

sectioned model of an ideal pressure vessel to that of the actuator tubes, clearly showing the similarities between them.

Referring to the naming schemes used in Figure 6.1, the radius used to calculate the hoop stress of Tube 1 and Tube 2 was taken as the design radius, while an effective radius had to be calculated for the top and bottom actuators, since both only formed partial tubes. Due to the nature of the ideal prototype design, it was noticed that the top and bottom actuators could each be approximated as partial sections of a pressure vessel with an effective radius. To find this effective radius of the top and bottom actuator tubes, a circle was fit through the attachment points of the top and bottom actuator was done by using a least-squares fitting algorithm.

For the circle fitting algorithm to obtain a unique solution, three points needed to be specified, but only two were available, namely the attachment points of each individual actuator tube to the base-structure. To ensure a unique solution, it was decided to constrain the length of the circle section between the attachment points to the length used to form the actuator tube during construction, which was previously defined as L_{Act}. This converted the least-squares problem into an iterative problem. The locations of the attachment points, the length that was fixed as well as an example of an approximated circle can be seen Figure 6.5.

The process starts by fitting a general circle through the attachment points of one of the actuator tubes, where-after the arc length between these points are calculated. The radius of the fitted circle is then iteratively adjusted until the circle segment equals the length as used during the construction of the actuator. It was found through the circle-fitting process that for both the top and bottom actuator tubes, a circle with the same radius and centre point was predicted, which was a result of the symmetric nature of the design.

Stellenbosch University https://scholar.sun.ac.za

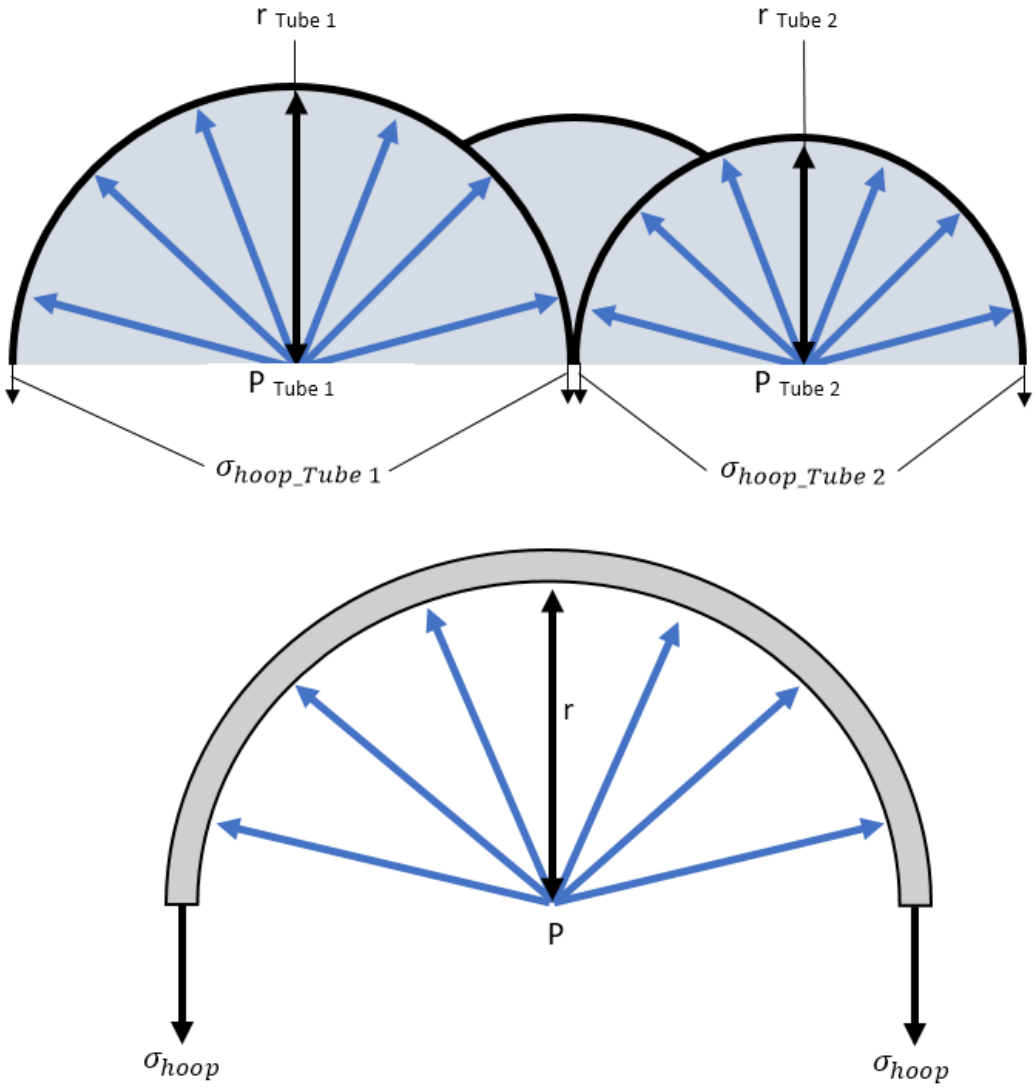

Figure 6.4: *Schematic Comparison Between an Ideal Pressure Vessel and Tubes used in Prototype Construction. [Top, Prototype Design; Bottom, Ideal Pressure Vessel*

To verify the validity of this assumption, four prototypes were selected at random from each CCD iteration and a circle was fit to the top and bottom actuators through the use of the built-in circle fitting tool available in *Tracker*. In Figure 6.6, an example of such a circle fit done through the use of *Tracker* can be seen, with the full results of this process displayed in Table 6.2. The build dimensions corresponding to each prototype tested can be found in Appendix C.

From Table 6.2 it can be seen that the predicted circle fit and experimentally measured circle agrees well, with the largest deviation resulting in 6.8mm and

Stellenbosch University https://scholar.sun.ac.za

the overall average deviation equalling 3.8mm. It can also be noted that the circle fitting algorithm under-predicts the true radius in all prototypes tested during the verification process resulting in a built-in safety factor when using the predicted radius to determine the maximum inflation pressure through Equation 6.2.1.

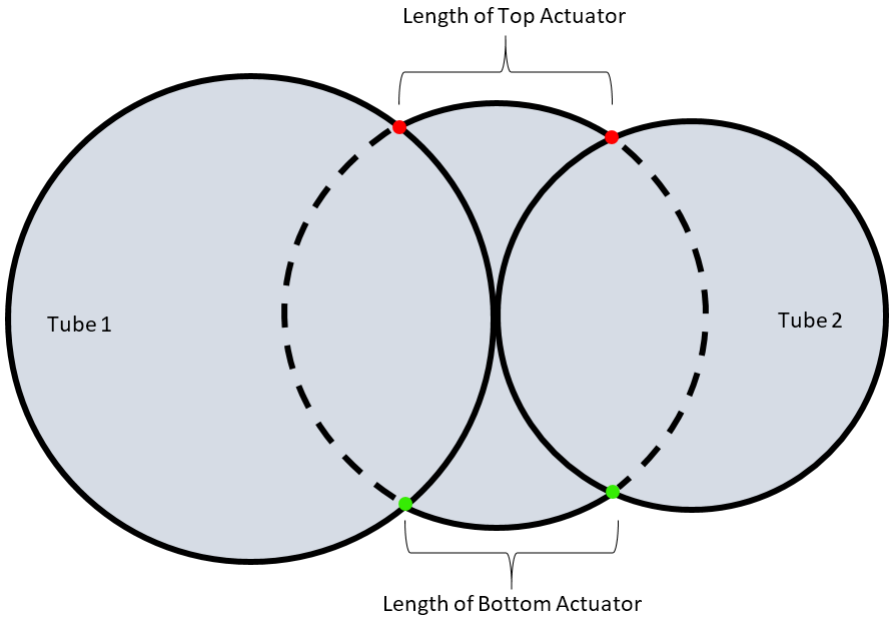

Figure 6.5: *Locations of Points used for Circle Fitting Shown as Dots and Example of Approximated Circle Shown as a Dashed Line. [Green Dot = Point used for Bottom Actuator Circle Fit; Red Dot = Point used for Top Actuator Circle Fit]*

Using the determined average seal strength as well as the ideal or calculated effective diameter of each individual tube along with Equation 6.2.1, the maximum inflation pressure for each tube could be determined. In Table 6.3 and Table 6.4, the calculated maximum inflation pressure for each unique tube diameter used can be seen. To minimise accidental seal rupture during testing, it was opted to inflate each tube only to 80% of its maximum inflation pressure, which is also available in Table 6.3 and Table 6.4.

To verify if the pressure calculation was valid, burst testing was done on three tubes constructed using the smallest, largest and an intermediate diameter. The results from the burst testing can be seen in Table 6.5. From Table 6.5, it can be seen that the maximum pressure calculated for the constructed tubes and the actual measured burst pressure are relatively similar, however it should be noted that the calculated pressure under-predicts the actual pressure in both cases. It can also be seen that the burst pressure of tests utilising the same

Stellenbosch University https://scholar.sun.ac.za

Table 6.2: *Experimental Verification of Circle Fit*

CCD Run	Prototype	Radius (mm)		
		Measured	Predicted	Difference
1	6	30	25	5
	C3	25	24	1
	1	41	37	4
	3	43	36	7
	4	52	48	4
2	0	37	33	4
	7	20	17	3
	3	52	50	2
	C1	37	30	7
3	5	33	28	5
	2	40	38	2
	0	25	24	1

Table 6.3: *Inflation Pressure of Top and Bottom Actuator Tubes using Effective Diameter*

Actautor Prameters (mm)			Pressure (kPa)	
L_{Actuator}	L_{Seal}	Effective Diameter	Max	Operating
30	3	28	14.1	11.3
	10	23	16.7	13.4
100	3	95	4.1	3.3
	10	92	4.2	3.4
50	5	46	8.4	6.7
	7	45	8.7	7.0
74	5	70	5.6	4.5
	7	68	5.7	4.6
50	3	47	8.2	6.6
	6	46	8.6	6.9
74	3	71	5.5	4.4
	6	69	5.6	4.5

Stellenbosch University https://scholar.sun.ac.za

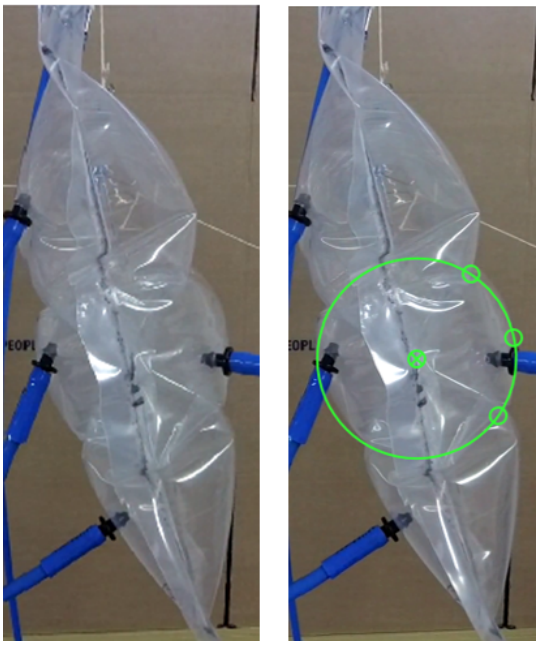

Figure 6.6: *Example of Experimental Circle Fit [Left, Prototype; Right Prototype with Circle Fit Overlay]*

Table 6.4: *Inflation Pressure of Tube 1 and 2 of Prototype using Ideal Diameter*

Diameter (mm)	Pressure (KPa)	
	Max	Operating
80	4.9	3.9
100	3.9	3.1
106	3.7	3.0
133	2.9	2.3
160	2.4	1.9
200	2.0	1.6

diameter is again distributed over a large range, which confirms the variability in the seal strength resulting from the sealing method used as previously mentioned. After all the calculations and experimental verification was done, it was decided to use 80% of the maximum pressure as displayed in Table 6.3 and Table 6.4 as the test pressure for all experiments that were to be carried out. This choice was made based on the fact that as shown by the burst tests, the calculated pressure under-predicted the actual measured pressure and by using the calculated pressure values an embedded safety factor against bursting was included, minimising the possibility of accidental seal rupture during testing.

Stellenbosch University https://scholar.sun.ac.za

Table 6.5: *Burst Test Results*

Diameter (mm)	Burst Pressure (KPa)				
	Test 1	Test 2	Test 3	Test 4	Average
23	16.3	15.9	17.6	17.8	16.9
100	4.0	3.7	4.5	3.8	4.0
200	2.1	3.00	2.5	2.3	2.5

6.2.2 Central-composite Design Study and Response Surface Methodology Approach

As mentioned in Chapter 3, the purpose of the central-composite design (CCD) in combination with the Response Surface Methodology (RSM) was to form a mathematical relationship between the identified parameters and the resulting bending output by fitting a second-order surface through the acquired data points. The Python-script described in Section 3.7.3 of Chapter 3 was used for both the generation of the prototypes derived from the implemented CCD as well as for fitting the second-order surface to the collected data.

As the search for the global minimum of the surface fit is a convergence problem, a convergence criterion had to be established to determine if the coordinates of the investigated parameters have settled on the global minimum. Based on manufacturing considerations, it was decided to accept the coordinates of the investigated parameters for the global minimum of the surface fit as converged if the coordinates of all three parameters remained within 1mm of the previous iteration. To satisfy this convergence criterion it was necessary to complete three iterations of the Central Composite Design. In Table 6.6, a summary of the design ranges chosen for each iteration of the parametric study can be seen, with the full design parameters as generated by the Python-script available in Appendix C.

Table 6.6: *Summary of Parameters Ranges as Used for Different Iterations of the CCD*

Design	Parameter Range [Min, Max]		
	D_1	$L_{Actuator}$	L_{Seal}
Iteration 1	[100, 200]	[30, 100]	[3, 10]
Iteration 2	[133, 200]	[50, 74]	[5, 7]
Iteration 3	[133, 200]	[50, 74]	[3, 6]

A box-plot showing a summary of the average deflection angles that were measured during the various iterations of the CCD are displayed in Figure 6.7, with the full results available in Table C.3, Table C.6 and Table C.9 found in

Stellenbosch University https://scholar.sun.ac.za

Appendix C. The complete experimental setup, equipment used and experimental procedure followed for the CCD deflection measurement can be found in Appendix B.

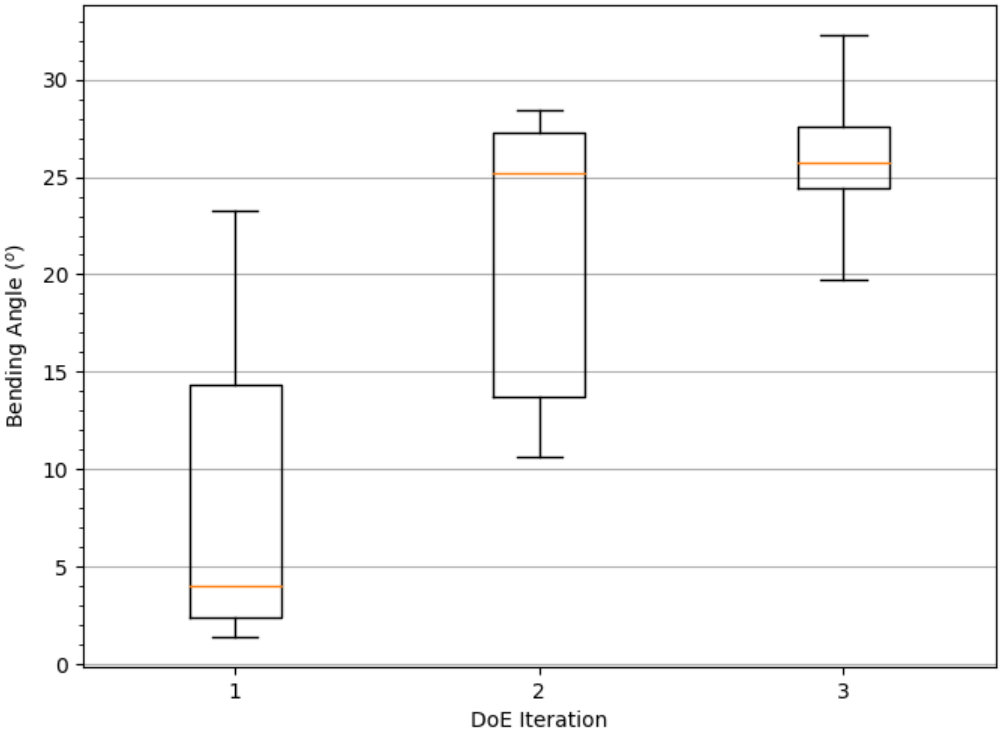

Figure 6.7: *Box-plot of the Average Bending Measurement Test Results for Different Iterations of the CCD*

It can be seen that for each consecutive CCD iteration the average bending angle increased which was a good indication that the parameters were converging on the global minimum as found in the specified design range. It can also be noted that for each CCD, the actuator that produced the maximum bending angle was constructed using the values of the parameters found in the center of the design space, indicating that the global minimum of the design space was located within the design space as originally chosen for the first iteration of the CCD. In Table 6.7, the resulting global minimum found for each iteration of the CCD can be seen.

For the first CCD and RSM iteration, the optimal parameters were found at the center of the design space, which is why it was opted to reduced the size of the design domain and center it around the previously found minima, rather than to shift the design range. From Table 6.7, it can be seen that for the second iteration of the CCD the minimum values for two of the three parameters satisfied the previously defined convergence criterion. It should also be noted

Stellenbosch University https://scholar.sun.ac.za

Table 6.7: *Global Minimum Coordinates Found for Each CCD and RSM Iteration*

CCD and RSM	Actuator Parameters		
	D_1	L_{Act}	L_{Seal}
Iteration 1	164.0	63.4	6.2
Iteration 2	164.3	63.9	3.3
Iteration 3	164.2	63.6	3.5

that for the second CCD and RSM the minimum value found for L_{seal} was outside of the design range, but was still within the initially defined design range. This along with the other two parameters satisfying the convergence criterion led to the decision to only shift the design space of L_{seal} and leave the design ranges of the other two parameters unchanged. As Table 6.7 shows, all three parameters satisfied the convergence criterion in the third iteration of CCD and RMS process. In this iteration the highest measured bending angle was also found, measuring at 33°.

Some performance metrics of the various curve fits done for each iteration of the CCD study as well as a comparison between the measured bending angle of the best performing actuator and the predicted bending angle of the derived model using the construction parameters of the best performing actuator as inputs. These results can be seen respectively in Table 6.8 and Table 6.10. The calculated performance metrics and what they represent can be found in Chapter 3 under Section 3.7.2.

Table 6.8: *Regression Performance Metrics of Curve fits done for each CCD and RSM Iteration*

CCD and RSM	Root Mean Squared Error (degrees)	Mean Absolute Error (degrees)	R^2
Iteration 1	1.956	1.844	0.929
Iteration 2	1.909	1.800	0.927
Iteration 3	1.685	1.589	0.916

Table 6.9: *Model Complexity Comparison of Final CCD and RSM Iteration*

Removed Variable	R^2	Adjusted R^2
D_1	0.562	0.299
L_{Act}	0.657	0.451
L_{Seal}	0.568	0.308
None	0.916	0.877

Stellenbosch University https://scholar.sun.ac.za

Table 6.10: *Prediction Performance of Derived Model for each CCD and RSM Iterations Using the Construction Parqameters of the Best Performing Prototype as Inputs*

CCD and RSM	Bending Angle (degrees)		
	Predicted	Measured	Difference
Iteration 1	24	23	1
Iteration 2	34	28	6
Iteration 3	33	31	2

It can be seen from Table 6.8 that the RMSE and MAE for all three derived models were between 1.5° and 2.0°, with the lowest values found in the third CCD and RSM iteration. This result showed that with each consecutive CCD and with the parameters converging on the global minimum, the errors between the predicted and measured data decreased. This decrease in error can be attributed to the decrease in the measured bending angle variance with each consecutive CCD iteration as can be seen by comparing the minimum and maximum measured bending angles as displayed in Figure 6.7.

Also from Table 6.8 it can be seen that for all three iterations the curve fits scored above 0.91 for the R^2-value, indicating that the model can predict a high amount of the variance found within the measured data. From Table 6.9 it can be seen that the chosen model is not unnecessarily over-complicated in terms of the number of variables added, which is confirmed by the models with terms removed scoring significantly lower in the R^2-value. This result confirmed that the models with terms neglected explained less of the variance found within the measured data compared to the original model containing all explored variables.

To verify the accuracy of the model derived from the measured deflection data of the final iteration of the parametric study, it was decided to build an actuator prototype using the optimal construction parameter combination found during the final iteration of the parametric study and comparing the measured and predicted bending angle. The construction parameters of this prototype can be found in Table 6.7. Through testing it was found that the constructed actuator prototype delivered a bending angle of 31°, where the mathematical model predicted a bending angle of 33°, resulting in an estimation error of 2°.

From this result, it can be seen that the derived mathematical model overestimates the actual bending angle. It should be noted that the derived model still predicts the true bending angle accurately to an error of under 10%, making the model useful for an initial estimation of the bending angle that can be produced by a prototype constructed with previously untested parameter values. In Figure 6.8a through Figure 6.8c, a visual representation of the curve

Stellenbosch University https://scholar.sun.ac.za

fit derived from the final CCD and RSM can be seen with each figure showing the curve with a single variable fixed to the optimal value found within the design space as displayed in Table 6.7.

It can be concluded From Figure 6.8a and Figure 6.8b that the bending angle is predominantly influenced by the parameter D_1, which is evident when studying the gradient of the curve along the x and y-axis respectively. By comparing the gradients of the curve along the x and y-axis of Figure 6.8c, it is evident that L_{Seal} is the dominating parameter, showing a larger influence on the bending angle for small variations in comparison to L_{Act}. It can also be noted from Figure 6.8c that the maximum bending angle is achieved when L_{Seal} is at the minimum edge of the design range, with the bending angle decreasing as L_{Seal} is increased.

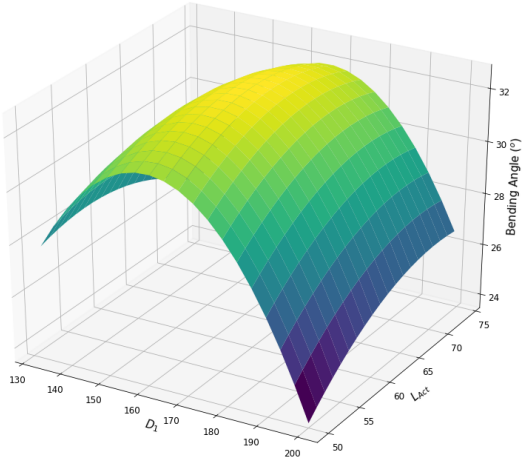

(a) $L_{Seal} = 3\ mm$

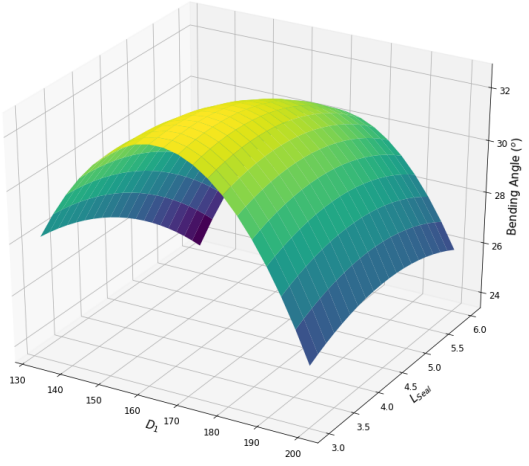

(b) $L_{Act} = 64\ mm$

Stellenbosch University https://scholar.sun.ac.za

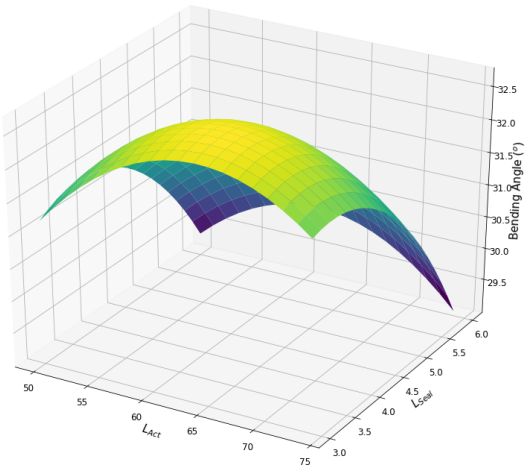

(c) $D_1 = 164$ *mm*

Figure 6.8: *Graphical Representation of the Generated Mathematical Model with one Parameter Fixed to the Optimal Value as found during the Final CCD and RSM Iteration*

6.3 One-Factor-at-a-Time Study of Selected Design

After the previous step involving the CCD and RSM was completed, certain parameters that were reduced to dependent variables through the simplifications made were selected and a One-Factor-at-a-Time (OFAT) study was carried out to determine the effect these parameters had on the deformation performance of the actuator. An OFAT study involves the change of only a single parameter at a time and was used in this project to increase the depth of the mathematical model formulated by including input variables previously left unexplored.

An OFAT study was chosen rather than constructing an entire new CCD, since only the effect of changing the attachment points of the polyethylene rectangles used to form the intermediate tubes were of interest. The attachment points were varied by adjusting the lengths $S_1 - S_4$, as displayed in Figure 6.1. Again, certain simplifications were made to the design to minimize the number of independent variables. The simplifications displayed in Equation 6.1.1 and Equation 6.1.3 were again applied as well as two new simplification displayed in Equation 6.3.1 and Equation 6.3.2.

$$S_1 = S_4 \text{ and } S_2 = S_3 \; ; \quad \text{From Symmetry Over the } y = x \text{ Plane} \tag{6.3.1}$$

$$S_1 = L_{\text{Actuator}} - L_{\text{Seal}} - S_2 \; ; \quad \text{From Manufacturing Considerations} \tag{6.3.2}$$

Stellenbosch University https://scholar.sun.ac.za

For the OFAT testing, the minimum and maximum value for S_1 were selected as 0 and 60 mm respectively and were divided into equal increments of 10 mm each. For each increment, an actuator was constructed and the resulting deformation measured. The parameters used for the construction of the OFAT actuator prototypes were fixed to the optimal values as predicted by the model derived in the final iteration of the CCD and RSM as mentioned in the previous section and displayed in Table 6.7. The range of the experiment was limited between 0 and 60 mm due to the reason that if either S_1 or S_2 is larger than the piece of polyethylene used to construct the actuator tubes, the actuator function breaks down and no useful deformation is generated.

During testing, the same pressures shown in Appendix B were again used for the different diameter tubes. The bending measurement results for the OFAT study can be seen graphically in Figure 6.9, with the results shown in Table C.10 available in Appendix C. From Figure 6.9 it can be seen that as S_1 increases, the bending angle also increases up to where $S_1 = S_2$. At this point, the maximum bending angle is achieved and by further increasing S_1 the bending angle steadily decreases back to zero.

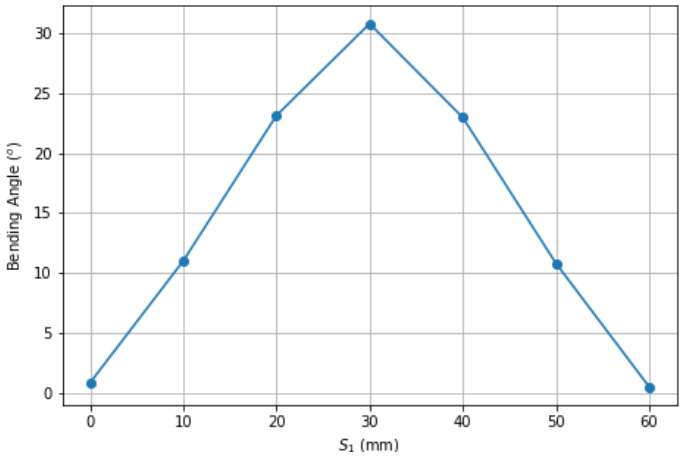

Figure 6.9: *Graphic Representation of OFAT Study Deflection Measurements*

Through observation it was noted that the measured data could be approximated by a simple mathematical function, with the equations describing this function displayed in Equation 6.3.3 through Equation 6.3.5. The function derived is graphically shown in Figure 6.10 along with the measured data displayed as dots. From the Figure 6.10 it can be seen that the approximation fits the measured data well, with the vertex and maximum bending angle fully captured over the tested range of S_1.

$$S_{\max} = \max(S) \; ; \quad \text{where } S = \text{ range of } S_1 \tag{6.3.3}$$

Stellenbosch University https://scholar.sun.ac.za

$$B_{\max} = \max(B) \; ; \quad \text{where } B = \text{ Measure Deflection Angle} \tag{6.3.4}$$

$$f(S) = 2B_{\max}\left[0.5 - \left|\frac{S - \frac{S_{\max}}{2}}{S_{\max}}\right|\right] \tag{6.3.5}$$

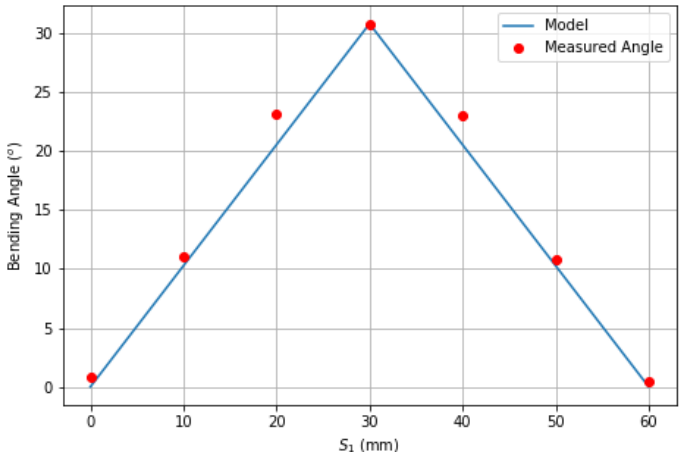

Figure 6.10: *Graphic Representation of Mathematical Model Derived from One-Factor-at-a-Time (OFAT) Study*

6.4 Observations Made from Studies

From the data gathered during the CCD and RSM studies, some interesting observations were made regarding how the fabrication parameters influenced the functionality of the actuator. During construction and the CCD testing, it was noted that actuators constructed using small top and bottom actuator membrane lengths reached their fully actuated state much faster in comparison to prototypes using larger top and bottom actuator membranes. This was expected since the actuation mechanisms relied on the pressure force induced by the inflation of the top and bottom actuator tubes. Pressure is a function of volume, which made the actuation force of the actuator tube a function of the inflated volume, resulting in a smaller tube delivering its maximum actuation force quicker than in comparison to a larger tube.

From the CCD measurement results, it was seen that actuators utilizing an L_{Act} to L_{Seal} ratio of ten or larger, delivered poor bending actuation performance. This was mostly a result of the seal being large enough to bulge outwards when pressure was increased in one of the actuator tubes. This bulging effect caused the seal to act as an internal tube, dramatically increasing the hinge stiffness, which resulted in a lower delivered bending actuation. In Figure 6.11, a schematic representation of this effect is shown.

Stellenbosch University https://scholar.sun.ac.za

Referring to the naming scheme used in Figure 6.1, it was noticed during the testing phase that when the ratio of the perimeter of the smaller base-structure tube forming the actuator and S_2 or S_4 is smaller than four, the bending actuation of the actuator is negatively influenced. This is caused by the inflation characteristics of the top and bottom actuator tubes. In cases where the ratio defined is smaller than four and these tubes are inflated, the actuator tube does not bulge outward in a circular manner, but rather in an elliptical shape, resulting in the membrane pulling the attachment points towards the center of the inflated membrane. This effect is not only confined to the smaller base-structure tube, but also occurs on the larger tube. This induced pull force results in a moment around the center point of the actuator acting on the tubes in the opposite direction of the intended bending direction, resulting in a decrease in the delivered bending actuation. In Figure 6.12, a schematic representation of this effect is shown. In the figure, the original locations of the attachment points are shown on the with the dashed line.

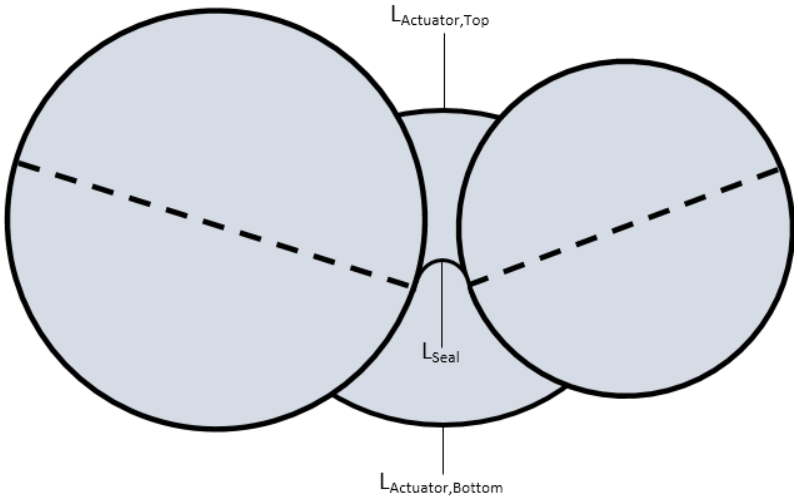

Figure 6.11: *Graphic Representation of Bulge Effect that Occurs when the Ratio of L_{Act} to L_{Seal} becomes Larger than Ten*

From the data gathered during the OFAT study, it was clear that for a maximum deflection angle the actuator tube should be centered between Tube 1 and Tube 2. It was also noted during testing that the stiffness of the point of rotation also decreased as the ratio of S_1 and S_2 moves away from one. This can be attributed to the basic design of the mechanism, where the joint stiffness is a result of the added stiffness created by the inflation of the actuator tubes. As the actuator tubes are shifted away from the center of the mechanism, the tube-joint overlap area of the actuator tube decreases, resulting in a smaller pressure force acting on one of the base-structure tubes, consequently

Stellenbosch University https://scholar.sun.ac.za

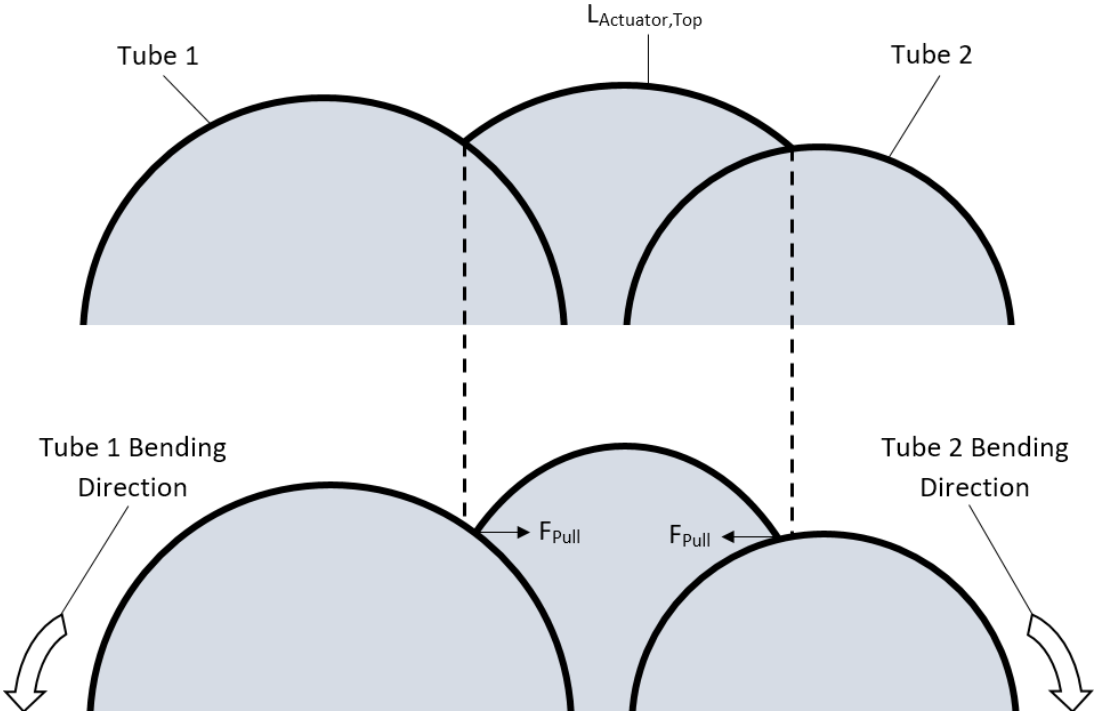

Figure 6.12: *Graphic Representation of Pull Effect that Occurs when the Ratio of the Perimeter of the Smaller Base-structure Tube Forming the Actuator and S_2 or S_4 becomes Smaller than Four. [Top, Actuator Tube Uninflated; Bottom, Actuator Tube Inflated]*

reducing the hinge or joint stiffness. In Figure 6.13, this phenomenon is displayed graphically, with the joint stiffness increasing with every consecutive actuator displayed.

Stellenbosch University https://scholar.sun.ac.za

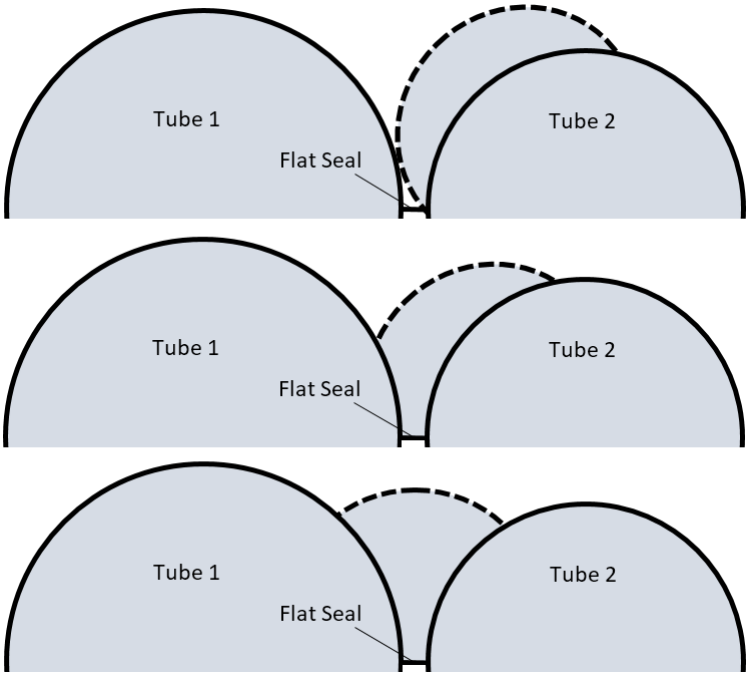

Figure 6.13: *Graphic Representation of Effect of Shifting Actuator Tubes on Joint stiffness [Top, Lowest Joint Stiffness; Bottom, Highest Joint Stiffness]*

Stellenbosch University https://scholar.sun.ac.za

Chapter 7

Final Morphing Wing Design

To demonstrate the feasibility of using the research done to construct a functioning morphing wing, it was decided to develop a final wing prototype that integrates the Base-structure and Multi-tube actuator discussed in Chapter 5 as well as utilizing the insights gained through the further exploration of the Multi-tube actuator as shown in Chapter 6. It was decided to construct a prototype with a length and width of 1000 mm, a thickness ratio of 0.23 and a total of six chambers, similar to the one used to validate the Python-script as mentioned in Chapter 5.

To be able to use and compare the bending estimation of the mathematical model generated during the final iteration of the DoE, the base-structure of the prototype was slightly modified by adjusting the locations of the fifth spar by 6 mm towards the leading edge. This was done to ensure the included actuator had the same dimensions as the optimal actuator found in the final iteration of the DoE as shown in Table 6.7. In Table 7.1, the construction parameters used for the Python-script described in Chapter 3 compared to the actual measurements of the constructed wing can be seen.

Table 7.1: *Parameters Comparison Between Input Parameters of Python-script and Actual Parameters of Constructed Wing*

Input Parameter	Python Generated	Constructed Wing	Difference
Length (mm)	1000	1015	15
Max Thickness (%)	0.230	0.210	0.020
Number of Chambers	6	6	0

Comparing the values as shown in Table 7.1, it can be seen that there are some discrepancies between the input parameters used and the actual measured parameters. The most noticeable difference is in the maximum thickness of the wing which differs with 0.011%. The maximum thickness as displayed in Table 7.1 is a ratio of the maximum thickness to the total length of the wing,

Stellenbosch University https://scholar.sun.ac.za

which meant for a wing with a length of 1000 mm, the percentage translates in a thickness difference of 20 mm. This difference can be explained by the polyethylene sheeting adding additional stiffness that the Python-script does not take into account since the inflation algorithm used to determine the lengths of each chamber only takes the internal forces due to the pressure and geometric constraints into account. The discrepancy in the length of the wing is mostly attributed to rounding of the generated design parameters to the nearest 5 mm, which was done to simplify the overall construction process. In Figure 7.1, the computer-generated model and the final wing in its symmetric configuration are shown for a side-by-side comparison. From this comparison, it can be seen that the chambers of the final constructed wing are not as curved as the predicted inflated shape. This could again be attributed to the polyethylene sheeting adding additional stiffness that was not accounted for in the Force Density Method calculations.

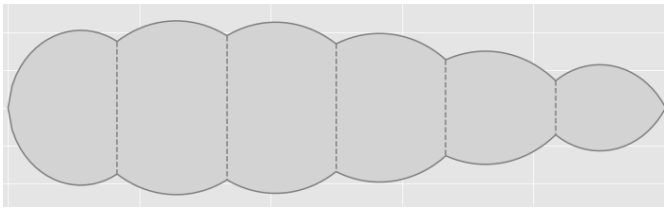

(a) *Python Generated Design*

(b) *Final Constructed Wing*

Figure 7.1: *Comparison of Python Generated Wing versus Constructed Wing*

In Figure 7.2, the extreme deformation modes of the final constructed wing can be seen along with two intermediate bending modes. In Figure 7.2, the center-line and the rotation point of the constructed prototype are respectively displayed by a dashed line and a filled circle. Through deflection measurement tests done on the final wing, it was found that the wing was not perfectly symmetric in terms of its bi-directional bending. During testing it was found that the constructed wing could rotate the rear portion of the wing by an average of 33° in a downwards direction, but only by an average of 30° in an upwards direction. To ensure this result was not influenced by the weight of the prototype, the experiment was redone with the prototype rotated by 180° along the length of the wing. The test with the prototype rotated again showed that the wing had a bias towards one direction, with the wing deflecting upwards by an average of 31° and downwards by an average of 29°. The directional bending

Stellenbosch University https://scholar.sun.ac.za

bias present in the wing could be attributed to the construction method used. As mentioned previously, heat-binding of the polyethylene sheeting is primarily used to construct the wing. During the sealing process, only a single side of the material is directly exposed to the heating-tool, which causes the opposite side of the polyethylene to slightly harden. This hardening effect results in a layer that resists bending towards the hardened side more than in comparison to the opposite side of the material. This phenomenon is briefly described during the literature review available in Chapter 2 and also formed the basis for the basic Diamond-seal actuator described in Chapter 5.

From the bending measurements made, the prototype delivered an overall average bending of 32° in a downwards direction and 29.5° in an upwards direction. Using the build dimensions of the prototype as the inputs for the mathematical model generated in Chapter 6, the maximum possible bending angle was estimated as 32.5°, resulting in a difference of only 0.5° in comparison to the maximum average measured bending angle of the constructed prototype. The complete results of the individual bending measurements can be found in Table C.11 available in Appendix C.

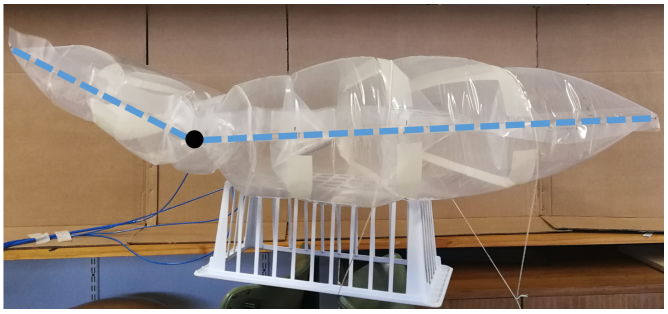

(a) *Maximum Upwards Camber Configuration achieved by Inflating Bottom Actuator Tube [Average Measured Deflection Angle: 29.5°]*

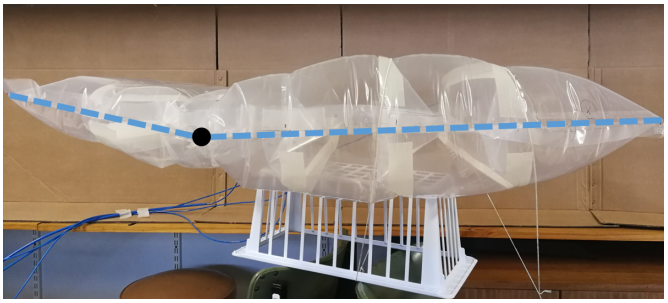

(b) *Intermediate Upwards Camber Configuration achieved by Inflating Bottom Actuator Tube and Partially Inflating Top Actuator Tube [Displayed Deflection Angle: 15°]*

Stellenbosch University https://scholar.sun.ac.za

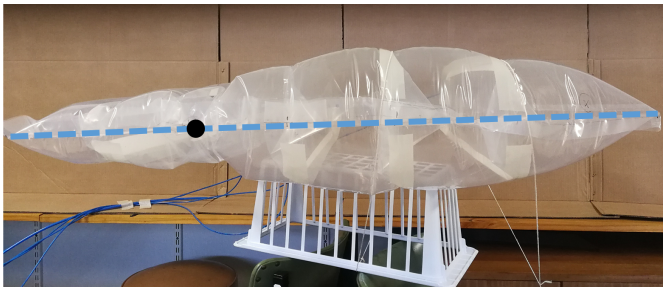

(c) *Symmetric Configuration achieved by Inflating both Top and Bottom Actuator Tubes*

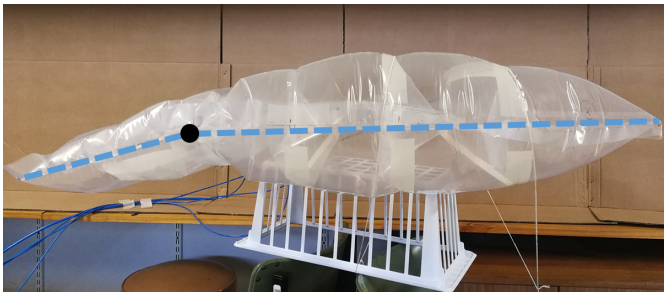

(d) *Intermediate Downwards Camber Configuration achieved by Inflating Top Actuator Tube and Partially Inflating Bottom Actuator Tube [Displayed Deflection Angle: 14°]*

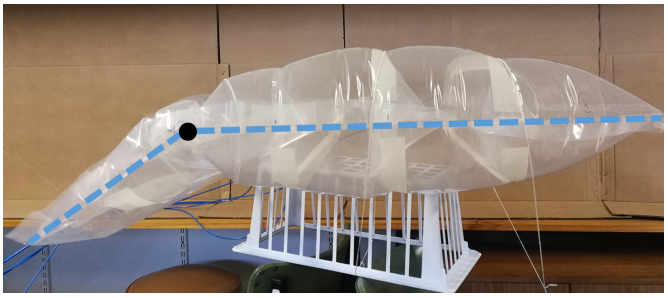

(e) *Maximum Downwards Camber Configuration achieved by Inflating Top Actuator Tube [Average Measured Deflection Angle: 32°]*

Figure 7.2: *Different Shape Configurations Possible with the Final Wing Design, with the Centre-line Displayed by the Dashed Line and the Rotation Point by a Filled Circle*

Stellenbosch University https://scholar.sun.ac.za

Chapter 8

Conclusion

Through the research presented here a topologically simple and low-cost wing capable of altering its camber during operation was developed. The developed wing was fully inflatable and self-supporting with the shape-changing mechanism embedded directly into the structure of the wing, resulting in a design that utilized no rigid components or complex joints between parts, making the design more resilient to impacts, such as low-speed collisions or low-altitude crashes, in comparison to traditional wing designs.

The designed wing consisted of two main components namely the base-structure and the morphing mechanism, both of which were designed through the use of an iterative systems design approach. The chosen base-structure as discussed in Chapter 5 consisted of two polyethylene sheets with horizontal polyethylene spars attached at predetermined locations to both the upper and lower sheet of polyethylene, effectively forming tubes when inflated.

Through this research, a Python-script was also developed which calculated the spar location and lengths based on any symmetrical NACA 4-digit aerofoil. This script also incorporated a Force Density Method (FDM) that simulated the inflated shape of a chosen aerofoil. The parameters as generated through the Python-script were used to construct a prototype. The resulting constructed geometry was then compared to the FDM-generated geometry through a 3D-scanning process.

The morphing or shape-changing mechanism chosen was inspired by the inherent spaces found in the selected base-structure design and consisted of two polyethylene rectangles bonded to both the upper and lower surface of two consecutive tubes of the base-structure, effectively forming intermediate tubes. The multi-tube actuator functioned on an antagonistic principle derived from a pressure difference between the upper and lower actuator tubes, resulting in a range of possible bending angles. A further exploration phase was carried out on the actuator design through a Design of Experiment (DoE) approach

Stellenbosch University https://scholar.sun.ac.za

by utilising a central-composite design (CCD) in conjunction with a response surface methodology (RSM) approach. This was done to increase the understanding of how the construction parameters of the actuator influenced its bending performance as well as to derive a mathematical model to estimate the bending performance of an actuator based on its design parameters.

Using the mathematical model derived through the RSM process, the optimal parameter combination located within the chosen design space was estimated and used to construct a prototype actuator. Using this actuator prototype and comparing the physically measured bending angle to the estimation made by the derived model resulted in an absolute error of only 2°, verifying that the model is useful for a preliminary estimation of the bending output of an actuator based on its construction parameters.

A final wing design was developed and constructed utilizing all knowledge acquired through this research. The base-structure of the final wing was based on a NACA-0023 with a chord length and width of 1000 mm, while the parameters used for the multi-tube actuator were set to the optimal results as found through the final iteration of the RSM. The final prototype wing was capable of delivering an average maximum bending of 29.5° and 32° in an upwards and downwards direction, respectively. Using the build parameters of the incorporated actuator as inputs for the mathematical model derived during the final CCD and RSM iteration, the maximum bending of the wing was estimated to be 32.5°, resulting in an error of only 0.5°.

Stellenbosch University https://scholar.sun.ac.za

Chapter 9

Suggested Improvements and Future Work

Looking at the developed prototype wing as well as the challenges encountered during manufacture, a clear improvement will be to manufacture the design out of some other material. The replacement material should still offer the benefits of polyethylene, but should be able to be bonded by some other method. Doing so would negate some of the imperfections due to the heat-sealing method used, resulting in a more airtight design. Another alternative to this is to develop a heat-sealing or manufacturing device specifically created to construct the proposed wing design.

One possible example of such a device is a foot-operated heat-sealer with the jaws extended or modified in such a way that the plastic sheeting can move past the jaws with less constraint, to allow sealing at various locations a conventional foot-operated heat-sealing machine cannot. In Figure 9.1, a conventional foot-operated heat-sealing machine can be seen, with the material only being able to move a finite distance past the jaws of the machine.

Using Computational Fluid Dynamic (CFD) techniques to simulate the design in its various shapes might also be of value, allowing rapid estimation of the aerodynamic characteristic of the designed wing without the need for a prototype. Doing so also opens the possibility to apply shape-optimization to the designed wing to allow rapid changes to be made to the design to possibly further increase the aerodynamic benefits the design offers.

After some preliminary simulations are run, a full-scale model can be constructed and aerodynamically tested through wind tunnel tests, which can at a later stage be compared to the aerodynamic characteristics of the developed wing to that of a traditional wing in its various cambered configurations. A full-scale model also offers the added benefit of being able to investigate the structural integrity of the wing through tests involving wing-buckling, wing-

Stellenbosch University https://scholar.sun.ac.za

Figure 9.1: *Conventional Foot-operated Heat-sealer with the Jaw-configuration Allowing Plastic Sheeting to only Move a Finite Distance Past the Seal Location*

twist as well as wing-tip deflection under a point load. These tests can also be extended to include vibrational analysis of the overall wing structure as well fatigue and life cycle testing of the actuator.

Another improvement that can be made to the current wing design is to add multiple actuation points along the length of the wing, instead of only one as done in the developed prototype. Incorporating multiple actuators at various locations along the length of the wing will not only dramatically increase the maximum camber change possible, but will also introduce a wide array of additional possible shapes-changes since multiple actuation points allow each section between actuation points to be able to rotate upwards as well as downwards independently from each other. Figure 9.2 shows a schematic comparison of the possible shape-change between a design with a single actuation point and a design with two actuation points.

From the middle image in Figure 9.2, only the back portion of the wing is actuated and allowed to rotate about the rotation point of the actuator, resulting in the camber changing characteristics as seen in the wing developed through this research. The bottom image of Figure 9.2 shows the possible shape-change when the wing is only actuated about the rotation point of the second actuator, with the back portion of the wing actuated in such a manner that it remains parallel to the front portion of the wing. Future work should, however, investigate if the wing shapes possible by incorporating multiple actuation points is useful enough to justify the increase in manufacturing complexity resulting from inserting multiple actuators.

Stellenbosch University https://scholar.sun.ac.za

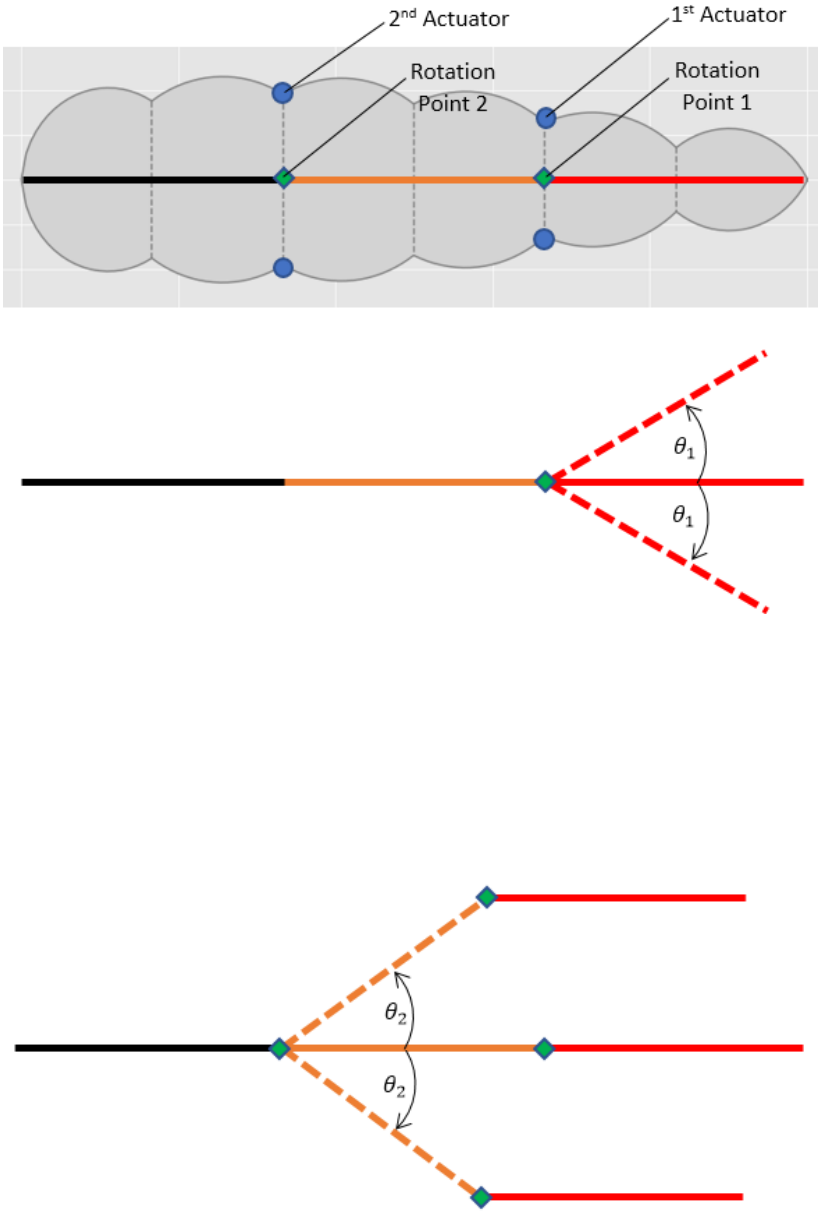

Figure 9.2: *Additional Auction Points Added to the Structure and Their Effect on the Bending Profile of the Wing [Top, Wing in Default Configuration with Actuator Locations, Rotation Points and Centre-line Shown; Middle, Shape Change Possible with only Actuator 1 Included; Bottom, Shape Change Possible with Both Actuator 1 and 2 Included]*

Stellenbosch University https://scholar.sun.ac.za

Appendices

Stellenbosch University https://scholar.sun.ac.za

Appendix A

Preliminary Testing of Base-structure and Morphing-Mechanism

The following section describes the experimental setup and equipment used for the preliminary testing done on the base-structure and morphing-mechanism designs described in Chapter 5.

A.1 Base-structure

A.1.1 Experimental Setup

For all base-structures a preliminary test was done to establish if the design was self-supporting or not. This test consisted of clamping the structure at the leading edge in a cantilever-like fashion and adding weight to see if the wing buckles. In Figure A.1, the test setup can be seen. As this was only a preliminary test, the weight was increased to a maximum of 1 kg. If the structure deflected more than 50 mm before 0.5 kg of additional weight was added, the structural stiffness and load-bearing capabilities were deemed too low and alterations to increase the stiffness of the design had to be made.

A.1.2 Equipment and Software Used during Experiments

- Tape measure
- Clamp
- 0.05 kg weights

Stellenbosch University https://scholar.sun.ac.za

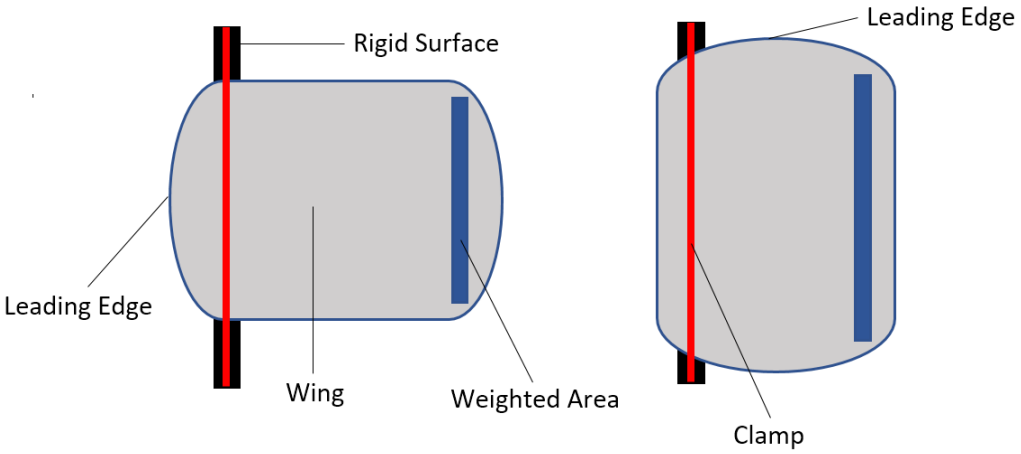

Figure A.1: *Preliminary Stiffness Test Setup of Wing Base-structure [Left, Stiffness Along Chord Tested; Right, Stiffness Along Width of Wing Tested]*

A.1.3 Test Procedure

1. Clamp base-structure to rigid object as shown in the left image of Figure A.1. Measure the centre-line height of the wing at the farthest distance away from the clamping position.
2. Add weight to location as shown in Figure A.1.
3. Remeasure centre-line height of the wing. Note added weight.
4. Repeat steps 2 and 3 until centre-line height of wing has deflected more than 50 mm.
5. Repeat process for wing configuration shown in the right image of Figure A.1.

A.1.4 Results

Table A.1: *Design 1 Stiffness Test Results*

Test	Weight Added (kg)	
	Chord Stiffness Test	Wing Width Stiffness Test
1	1	1
2	1	1
3	1	1
Average	1	1

Stellenbosch University https://scholar.sun.ac.za

Table A.2: *Design 2 Stiffness Test Results*

Test	Weight Added (kg)	
	Chord Stiffness Test	Wing Width Stiffness Test
1	0	0.4
2	0	0.45
3	0	0.45
Average	0	0.43

Table A.3: *Modified Design 2 Stiffness Test Results*

Test	Weight Added (kg)	
	Chord Stiffness Test	Wing Width Stiffness Test
1	0.60	0.65
2	0.60	0.70
3	0.65	0.60
Average	0.62	0.65

Table A.4: *Design 3 Stiffness Test Results*

Test	Weight Added (kg)	
	Chord Stiffness Test	Wing Width Stiffness Test
1	0.75	0.75
2	0.75	0.80
3	0.75	0.75
Average	0.75	0.77

A.2 Morphing-Mechanism

A.2.1 Experimental Setup

For the morphing-mechanism a similar test was carried out. The tests carried out served to determine the stiffness and load-bearing capabilities of the bending joint as well as a preliminary actuation-force measurement. The test setup can be seen in Figure A.2.

For the joint stiffness tests, the structure was clamped in a cantilever-like fashion and the morphing-mechanism was actuated to such an extent so that the

Stellenbosch University https://scholar.sun.ac.za

wing was in a symmetric configuration. Weights were then added to the location shown in Figure A.2 until the trailing-edge of the wing deflected more than 50 mm from its original state.

For the preliminary actuation-force measurement, weights were added to the location as shown in Figure A.2 while the wing was in a symmetric configuration. After the weights were added, the morphing-mechanism was allowed to actuate for its entire range of motion. This process was repeated until the mechanism could no longer actuated fully with the added weight.

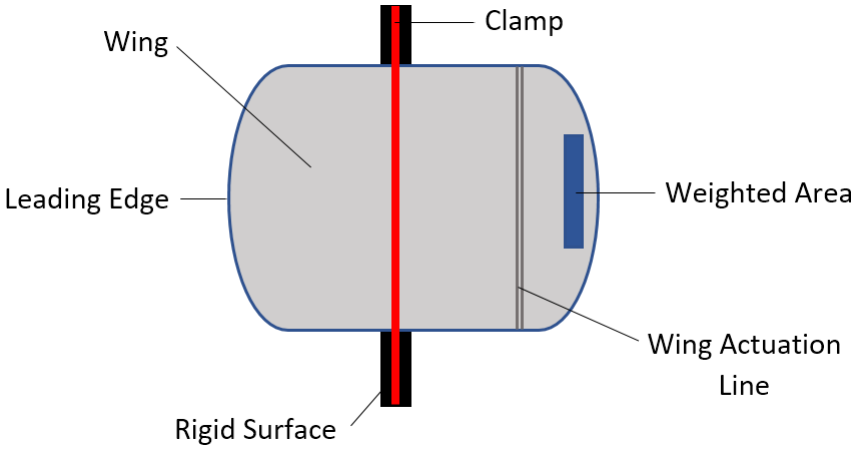

Figure A.2: *Preliminary Stiffness Test Setup of the Wing Morphing-mechanism*

A.2.2 Equipment Used during Experiments

- Tape measure
- Clamp
- 0.05 kg weights

A.2.3 Test Procedure For Joint Stiffness Test

1. Clamp base-structure to rigid object as shown in Figure A.2. Ensure wing is in a symmetric configuration.
2. Measure the centre-line height of the wing at the trailing-edge.
3. Add weight to location as shown in Figure A.2.
4. Remeasure centre-line height of the wing. Note added weight.

Stellenbosch University https://scholar.sun.ac.za

5. Repeat until wing trailing-edge deflects more than 50 mm from original position

A.2.4 Test Procedure For Preliminary Actuation-force Measurement

1. Clamp base-structure to rigid object as shown in Figure A.2. Ensure wing is in a symmetric configuration.
2. Add weight to location as shown in Figure A.2.
3. Allow morphing-mechanism to actuate for its entire range of motion.
4. Repeat steps 2 and 3 until the actuator can no longer actuate for its entire range of motion.

A.2.5 Results

Table A.5: *Antagonistic Diamand Actuator Stiffness and Actuation-Force Test Results*

Test	Weight Added (kg)	
	Joint Stiffness	Actuation-force
1	0.55	0.4
2	0.45	0.45
3	0.45	0.45
Average	0.48	0.43

Table A.6: *Multi-tube Actuator Stiffness and Actuation-Force Test Results*

Test	Weight Added (kg)	
	Joint Stiffness	Actuation-force
1	0.60	0.50
2	0.65	0.45
3	0.65	0.50
Average	0.63	0.48

Stellenbosch University https://scholar.sun.ac.za

Appendix B

Experimental Setup, Equipment Used and Test Procedure

The following section describes the experimental setup, equipment and software used to complete the parametric experimentation as described in Section 3.7 of Chapter 3. A brief explanation of the test procedure is also available in this section.

B.1 Equipment and Software Used during Experiments

- -10-10 kPa Pressure transducer (Brand: Endress+Hauser; Serial: PMD75-AAA7D212AAU)
- 0-50 kPa Pressure transducer (Brand: Endress+Hauser; Serial: PMD55-AA21BA67FGBHH4A1A-AA)
- Camera (Brand:Yi Technology; Max Resolution: 4k; Serial: 2AFIB-YAS1616)
- Camera Tri-pod
- 10 mm diameter dowel rod
- Nylon Rope
- Clasps to attach suspenders to actuators (x3)
- Tracker Physics software (Version: 5.0.7)
- Computer: (Core Speed 2.6 GHz; CPU: Intel Core i7, RAM: 16 GB)
- 10 Bar pressure line

Stellenbosch University https://scholar.sun.ac.za

- Ball valve
- 3d-printed throttle/pressure release valves (x4)

B.2 Experimental Setup

In Figure B.1, a diagram representing the full test setup can be seen.

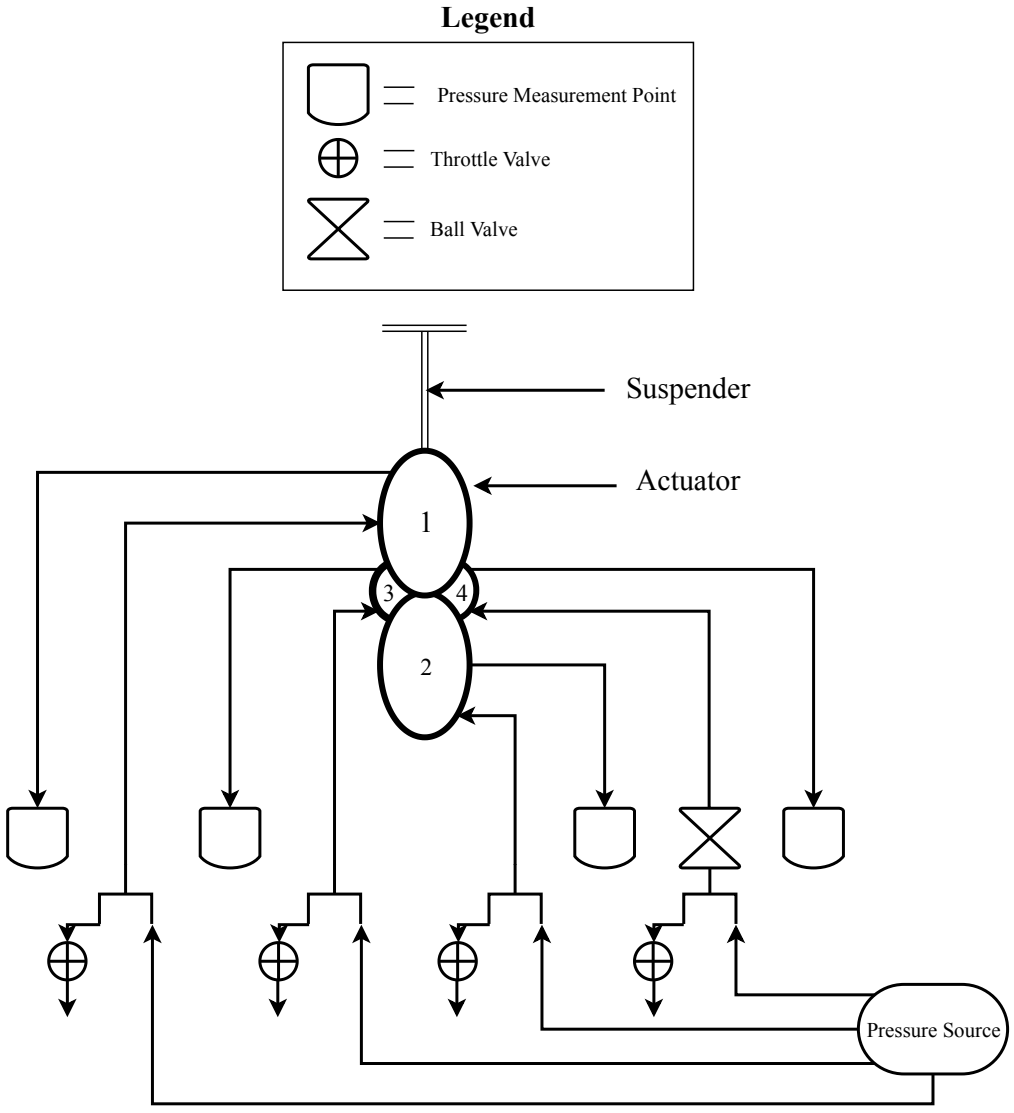

Figure B.1: *Diagram of Test Setup Used During DoE Deformation Measurement with the all Actuator Tubes Numbered as well as Input, Throttle-valve and Measurement Points Displayed*

Stellenbosch University https://scholar.sun.ac.za

For the experiment the actuator prototypes were suspended from a wooden dowel rod that was fixed to the ceiling of the test laboratory. To prevent unwanted motion during the actuation process, the prototypes were held in place by a suspension system attached to the upper tube of the prototype, labelled "1" in Figure B.1. All input tubes to the prototype were also suspended in such a manner as to minimise the influence on the prototype.

To accurately test each prototype, four individually controllable pressure lines were required, but only one was available in the test facility. To solve this issue, a valve system was created, consisting of *Festo* pneumatic piping, four ball valves and four additional 3d-printed throttle valves. The *Festo* pneumatic piping along with the the ball valves were used to split the pressure line into four individual lines. This setup also offered the added benefit of being able to roughly control the pressure in each line by opening or closing the ball valves. To achieve finer control of the pressure in each chamber four throttle valves were added to the system. In Figure B.2, the components forming the throttle valve assembly can be seen, with an isometric view of the valve displayed in Figure B.3.

These valves were then systematically closed until the desired pressure within each tube was reached. This process was iterative in nature, since all pressure lines were effectively connected to the original main pressure line, resulting in the pressure changing slightly in each tube with every adjustment made to a throttle or ball valve. With the throttle valves added, it was also possible to apply constant pressure to each tube, effectively negating the pressure loss resulting from any seal defects present in the prototype.

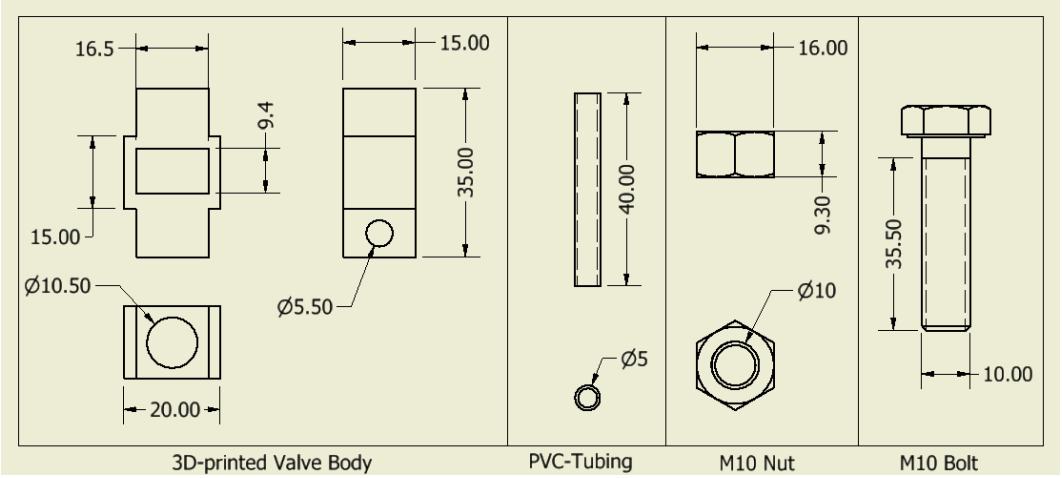

Figure B.2: *Individual Components Forming the Throttle Valve Assembly with Dimensions Shown*

Stellenbosch University https://scholar.sun.ac.za

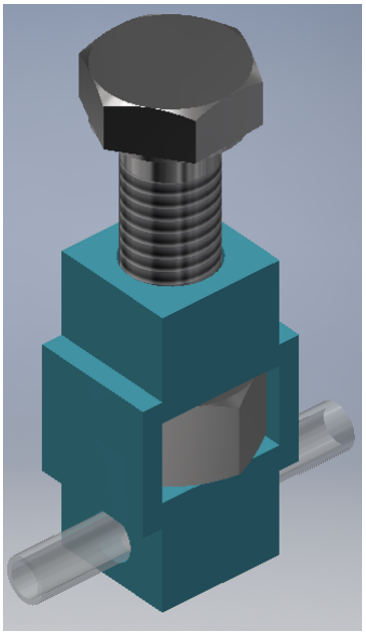

Figure B.3: *Isometric View of Throttle Valve Assembly*

For measuring the deflection angle produced, a camera mounted on a tripod was used to capture images of the passive as well as the actuated state of the prototype. The image files were then combined to form a video consisting of two frames and analysed by using *Tracker*.

B.3 Test Procedure

1. Suspend prototype from ceiling and connect to suspension system.
2. Connect each tube to an individual pressure line with ball and throttle valves fully open.
3. Close the ball valve associated with tube 4 as displayed in Figure B.
4. Open main pressure valve until reading on the dial shows 15 kPa.
5. Adjust the pressure in each tube by opening or closing the ball valves associated with each tube until all tubes are stiff to the touch and below maximum allowed pressure.
6. Fine tune pressure in each tube by adjusting the associated throttle valve. Repeat for all tubes, checking the pressure readings in all previously adjusted tubes, making adjustments as necessary.
7. Check if all tubes are at the predefined maximum allowed pressure for the selected diameter.

Stellenbosch University https://scholar.sun.ac.za

8. Capture image of passive state.
9. Close main pressure valve.
10. Open the ball valve associated with tube 4 as displayed in Figure B.
11. Repeat steps 4-7.
12. Capture image of actuated state.
13. Combine images int two frame video clip.
14. Load video into *Tracker* and define axis and point to track.
15. Activate auto-tracking and measure deflection angle relative to defined axis. Save measured data.
16. Repeat for all constructed prototypes.

Stellenbosch University https://scholar.sun.ac.za

Appendix C

Prototype Construction Parameters and Test Results

The following chapter contains the build parameters used as well as the results for each iteration of the central-composite design study. Deformations measured during the One-Factor-at-a-Time study as well as for the final wing prototype can also be found in this chapter.

C.1 Central Composite Design

C.1.1 Iteration 1

Table C.1: *Design Variable Range used for Iteration 1*

	Design Range	
	Minimum	Maximum
D_1	100	200
L_{Actuator}	30	100
L_{Seal}	3	10

Stellenbosch University https://scholar.sun.ac.za

Table C.2: *Prototype Design Parameters Used for Iteration 1*

Design	D_1	D_2	L_{Actuator}	L_{Seal}
1	100	80	30	3
2	200	160	30	3
3	100	80	100	3
4	200	160	100	3
5	100	80	30	10
6	200	160	30	10
7	100	80	100	10
8	200	160	100	10
Center	150	100	65	6.5

Table C.3: *Deflection Measurements of Iteration 1*

Design	Result (Degrees)				
	Test 1	Test2	Test 3	Average	Standard Deviation
1	8	8	8	8	0
2	15	14	14	14	0.5
3	1	2	2	2	0.5
4	4	4	3	4	0.5
5	2	3	3	3	0.5
6	4	4	4	4	0
7	2	1	2	2	0.5
8	15	15	16	15	0.5
C1	23	24	23	23	0.5
C2	23	23	23	23	0
C3	23	23	24	23	0.5

C.1.2 Iteration 2

Table C.4: *Design Variable Range used for Iteration 2*

	Design Range	
	Minimum	Maximum
D_1	100	200
L_{Actuator}	30	100
L_{Seal}	3	10

Stellenbosch University https://scholar.sun.ac.za

Table C.5: *Prototype Design Parameters Used for Iteration 2*

Design	D_1	D_2	L_{Actuator}	L_{Seal}
1	133	106	50	5
2	200	160	50	5
3	133	106	74	5
4	200	160	74	5
5	133	106	50	7
6	200	160	50	7
7	133	106	74	7
8	200	160	74	7
Center	167	133	62	6

Table C.6: *Deflection Measurements of Iteration 2*

Design	Result (Degrees)				
	Test 1	Test2	Test 3	Average	Standard Deviation
1	23	22	24	24	0.5
2	27	28	28	27	0.5
3	28	29	27	28	0.8
4	29	29	28	29	0.5
5	14	14	14	14	0
6	12	12	11	12	0.5
7	10	11	11	11	0.5
8	23	23	24	23	0.5
C1	27	28	27	27	0.5
C2	28	28	27	28	0.5
C3	27	27	27	27	0

C.1.3 Iteration 3

Table C.7: *Design Variable Range used for Iteration 3*

	Design Range	
	Minimum	Maximum
D_1	100	200
L_{Actuator}	30	100
L_{Seal}	3	10

Stellenbosch University https://scholar.sun.ac.za

Table C.8: *Prototype Design Parameters Used for Iteration 3*

Design	D_1	D_2	L_{Actuator}	L_{Seal}
1	133	106	50	3
2	200	160	50	3
3	133	106	74	3
4	200	160	74	3
5	133	106	50	6
6	200	160	50	6
7	133	106	74	6
8	200	160	74	6
Center	167	133	62	5

Table C.9: *Deflection Measurements of Iteration 3*

Design	Result (Degrees)				
	Test 1	Test2	Test 3	Average	Standard Deviation
1	26	26	26	26	0
2	25	25	25	25	0
3	28	28	28	28	0
4	25	24	24	24	0.5
5	26	26	26	26	0
6	22	22	22	22	0
7	20	20	20	20	0
8	28	27	28	28	0.5
C1	33	32	33	33	0.5
C2	32	32	32	32	0
C3	33	32	32	32	0.5

Stellenbosch University https://scholar.sun.ac.za

C.2 OFAT Study

Table C.10: *OFAT Study Deflection Measurement Results*

S_1	S_2	Result (Degrees)				
		Test 1	Test 2	Test 3	Average	Standard Deviation
0	60	1	1	1	1	0
10	50	10	11	12	11	1
20	40	23	23	23	23	0
30	30	31	31	31	31	0
40	20	23	23	23	23	0
50	10	10	11	11	11	1
60	0	1	0	0	0	1

Stellenbosch University https://scholar.sun.ac.za

C.3 Final Wing Build Deflection Measurements

Table C.11: *Final Wing Build Deflection Measurements*

Test	Orientation			
	Normal		180 Flipped	
	Downwards	Upwards	Downwards	Upwards
1	33	30	32	28
2	33	29	31	29
3	34	32	31	29
Average	33	30	31	29

Stellenbosch University https://scholar.sun.ac.za

List of References

ASTM International (2013). Standard Test Method for Seal Strength of Flexible Barrier Materials 1. *ASTM International*, , no. F88, pp. 1–11.

Barbarino, S., Ameduri, S., Lecce, L. and Concilio, A. (2009). Wing shape control through an SMA-based device. *Journal of Intelligent Material Systems and Structures*, vol. 20, no. 3, pp. 283–296. ISSN 1045389X.

Barbarino, S., Bilgen, O., Ajaj, R.M., Friswell, M.I. and Inman, D.J. (2011). A review of morphing aircraft. *Journal of Intelligent Material Systems and Structures*, vol. 22, no. 9, pp. 823–877. ISSN 1045389X.

Boldmethod (2019). Aerodynamic Facts About Flaps.
Available at: `https://bit.ly/2O35om9`

Breuer, J., Ockels, W. and Luchsinger, R. (2007). An inflatable wing using the principle of Tensairity. *48th AIAA/ASME/ASCE/AHS/ASC Structures, Structural Dynamics, and Materials Conference*, pp. 1–12. ISSN 02734508.
Available at: `http://arc.aiaa.org/doi/10.2514/6.2007-2117`

Breuer, J.C.M. and Luchsinger, R.H. (2010). Inflatable kites using the concept of Tensairity. *Aerospace Science and Technology*, vol. 14, no. 8, pp. 557–563. ISSN 12709638.
Available at: `http://dx.doi.org/10.1016/j.ast.2010.04.009`

Brown, D. (2006). Chapter 16: Tracker. *Open Source Physics: A User's Guide with Examples*, pp. 337–365.
Available at: `https://bit.ly/3473wOY`

Chopra, I. (2000). Status of application of smart structures technology to rotorcraft systems. *Journal of the American Helicopter Society*, vol. 45, no. 4, pp. 228–252.

Chougule, V.N., Gosavi, H.S., Dharwadkar, M.M. and Gaind, A.A. (2018). Review of Different 3D Scanners and Scanning Techniques. *IOSR Journal of Engineering (IOSRJEN)*, pp. 41–44.
Available at: `www.iosrjen.org`

Dano, M.L. and Hyer, M.W. (2001). Snap-through of unsymmetric fiber-reinforced composite laminates. *International Journal of Solids and Structures*, vol. 39, no. 1, pp. 175–198. ISSN 00207683.

Stellenbosch University https://scholar.sun.ac.za

Dayyani, I., Khodaparast, H.H., Woods, B.K.S. and Friswell, M.I. (2015). The design of a coated composite corrugated skin for the camber morphing airfoil. *Journal of Intelligent Material Systems and Structures*, vol. 26, no. 13, pp. 1592–1608. ISSN 15308138.
Available at: `https://doi.org/10.1177/1045389X14544151`

dos Santos e Lucato, S.L., Wang, J., Maxwell, P., McMeeking, R.M. and Evans, A.G. (2004). Design and demonstration of a high authority shape morphing structure. *International Journal of Solids and Structures*, vol. 41, no. 13, pp. 3521–3543. ISSN 00207683.

Feng, N., Liu, L., Liu, Y. and Leng, J. (2015). A bio-inspired, active morphing skin for camber morphing structures. *Smart Materials and Structures*, vol. 24, no. 3. ISSN 1361665X.

Gong, X., Liu, L., Scarpa, F., Leng, J. and Liu, Y. (2017). Variable stiffness corrugated composite structure with shape memory polymer for morphing skin applications. *Smart Materials and Structures*, vol. 26, no. 3. ISSN 1361665X.

Gude, M. and Hufenbach, W. (2006). Design of novel morphing structures based on bistable composites with piezoceramic actuators. *Mechanics of Composite Materials*, vol. 42, no. 4, pp. 339–346. ISSN 01915665.

Gude, M., Hufenbach, W. and Kirvel, C. (2011). Piezoelectrically driven morphing structures based on bistable unsymmetric laminates. *Composite Structures*, vol. 93, no. 2, pp. 377–382. ISSN 02638223.
Available at: `http://dx.doi.org/10.1016/j.compstruct.2010.09.004`

Hutchinson, R.G., Wicks, N., Evans, A.G., Fleck, N.A. and Hutchinson, J.W. (2003). Kagome plate structures for actuation. *International Journal of Solids and Structures*, vol. 40, no. 25, pp. 6969–6980. ISSN 00207683.

Kluga, N. (1991). A Study of Flap Management, an Analysis of the Consequences of Flap Management, and a Search for Possible Causes. *Journal of Aviation/Aerospace Education & Research*, vol. 1, no. 3. ISSN 2329-258X.

Liang, C. and Rogers, C.A. (1990). One-dimensional thermomechanical constitutive relations for shape memory materials. In: *Collection of Technical Papers - AIAA/ASME/ASCE/AHS/ASC Structures, Structural Dynamics and Materials Conference*, pt 1, pp. 16–28. Long Beach, CA, USA. ISSN 02734508.

Lu, T.J., Hutchinson, J.W. and Evans, A.G. (2001). Optimal design of a flexural actuator. *Journal of the Mechanics and Physics of Solids*, vol. 49, no. 9, pp. 2071–2093. ISSN 00225096.

Luo, Q. and Tong, L. (2013). Adaptive pressure-controlled cellular structures for shape morphing: II. Numerical and experimental validation. *Smart Materials and Structures*, vol. 22, no. 5. ISSN 09641726.

Stellenbosch University https://scholar.sun.ac.za

Mathur, S. and Malik, S. (2010). Advancements in the V-Model. *International Journal of Computer Applications*, vol. 1, no. 12, pp. 30–35.

Mitas, P., Wilkowski, J. and Podziewski, P. (2014). Various Wood Species . vol. 150, pp. 147–150.

Mohammed Elmardi Osama (2016). *Text Book On Dynamic Relaxation Method*. 1st edn. LAP LAMBERT Academic Publishing, Saarbruken, Germany. ISBN 978-3-659-94751-3.

Ou, J., Vlavianos, N., Heibeck, F., Ishii, H., Peters, J., Cheng, C.-Y. and Skouras, M. (2016). aeroMorph - Heat-sealing Inflatable Shape-change Materials for Interaction Design. pp. 121–132. ISSN 00653438.

Schek, H.J. (1974). The force density method for form finding and computation of general networks. *Computer Methods in Applied Mechanics and Engineering*, vol. 3, no. 1, pp. 115–134. ISSN 00457825.

SKYbrary (2016). AP4ATCO - Wing Mechanisms.
Available at: `https://www.skybrary.aero/index.php/AP4ATCO_-_Wing_Mechanism#Wing_Mechanisms`

Sofla, A.Y.N., Elzey, D.M. and Wadley, H.N.G. (2008). Two-way antagonistic shape actuation based on the one-way shape memory effect. *Journal of Intelligent Material Systems and Structures*, vol. 19, no. 9, pp. 1017–1027. ISSN 1045389X.

Tanaka, K. (1986). Termomechanical Sketch of Shape Memory Effect: One-dimensional Tensile Behaviour. *Res Mechanica: International Journal of Structural Mechanics and Materials Science*, vol. 18, no. 3, pp. 251–263.

Vasista, S. and Tong, L. (2012). Design and Testing of Pressurized Cellular Planar Morphing Structures. *AIAA Journal*, vol. 50, no. 6, pp. 1328–1338. ISSN 0001-1452.
Available at: `http://arc.aiaa.org/doi/10.2514/1.J051427`

Veenendaal, D. and Block, P. (2012). An overview and comparison of structural form finding methods for general networks. *International Journal of Solids and Structures*, vol. 49, no. 26, pp. 3741–3753. ISSN 00207683.
Available at: `http://dx.doi.org/10.1016/j.ijsolstr.2012.08.008`

Vos, R., Barrett, R. and Romkes, A. (2011). Mechanics of pressure-adaptive honeycomb. *Journal of Intelligent Material Systems and Structures*, vol. 22, no. 10, pp. 1041–1055. ISSN 1045389X.